January 2009

Spectral and Stratigraphic Mapping of Hydrated Sulfate and Phyllosilicate-bearing Deposits: Implications for the Aqueous History of Sinus Meridiani, Mars

Sandra Wiseman
Washington University in St. Louis

WASHINGTON UNIVERSITY IN ST. LOUIS

Department of Earth and Planetary Sciences

Dissertation Examination Committee:
Raymond Arvidson, Chair
Jeffrey Catalano
Patrick Crowley
Daniel Giammar
Bradley Jolliff
Jill Pasteris

SPECTRAL AND STRATIGRAPHIC MAPPING OF HYDRATED SULFATE AND PHYLLOSILICATE-BEARING DEPOSITS: IMPLICATIONS FOR THE AQUEOUS HISTORY OF SINUS MERIDIANI, MARS

by

Sandra Margot Wiseman

A dissertation presented to the
Graduate School of Arts and Sciences
of Washington University in
partial fulfillment of the
requirements for the degree
of Doctor of Philosophy

August 2009

Saint Louis, Missouri

ABSTRACT OF THE DISSERTATION

Spectral and Stratigraphic Mapping of Hydrated

Sulfate and Phyllosilicate-bearing Deposits: Implications for

the Aqueous History of Sinus Meridiani, Mars

by

Sandra Margot Wiseman

Doctor of Philosophy in Earth and Planetary Sciences

Washington University in St. Louis, 2009

Professor Raymond Arvidson, Chairperson

Data acquired by the Mars Reconnaissance Orbiter (MRO) are used in conjunction with additional data sets to perform detailed stratigraphic and spectral analyses with the goal of identifying and mapping the mineralogy and stratigraphy of sedimentary deposits to infer the aqueous history of the Sinus Meridiani region on Mars. Datasets utilized include MRO Compact Reconnaissance Imaging Spectrometer for Mars (CRISM), MRO Context Imager, MRO High Resolution Imaging Science Experiment, Mars Express (MEX) Observatoire pour la Minéralogie, l'Eau, les Glaces et l'Activité, MEX High Resolution Stereo Camera, Mars Odyssey (ODY) Thermal Emission Imaging System, ODY Mars Orbital Camera, and ODY Mars Orbiter Laser Altimeter data.

Spectral analyses focus on detection, identification, and mapping of hydrated and/or hydroxylated alteration minerals in the near infrared region between ~1.0 and 2.5 μm. An extensive analysis is presented on methods for the retrieval of atmospherically

corrected CRISM surface Lambert Albedo spectra using Discrete Ordinate Radiative Transfer modeling.

Sedimentary deposits indicative of a complex aqueous history occur in Sinus Meridiani. Fe/Mg phyllosilicate minerals, including Fe/Mg smectites, are detected in ancient Noachian cratered terrains. Fe/Mg smectites also occur in association with layered sedimentary deposits that unconformably overlie the Noachian cratered terrain. Both of these units predate the formation of the sulfate and hematite-bearing unit on which the Mars Exploration Rover Opportunity landed. At least one episode of intense erosion acted on the sedimentary deposits. A thick sequence of layered hydrated sulfate deposits that are texturally and spectrally distinct from the sulfate rich bedrock explored by the Opportunity Rover occurs in northern Sinus Meridiani. Detailed stratigraphic analyses indicate that these deposits are not readily explained by a simple layered stratigraphy and an unconformable facies change is inferred to have occurred.

The presence of Fe/Mg smectite-bearing deposits indicates that the low pH conditions experienced by younger hematite-bearing materials are not representative of the aqueous geochemical environment that prevailed during the formation of earlier materials. The deposits in Sinus Meridiani record the transition from an open hydrologic system with near neutral pH conditions to a more arid acid-sulfate dominated ground water system.

ACKNOWLEDGEMENTS

I thank my advisor, R. E. Arvidson, for his guidance and mentorship. R. V. Morris and M. J. Wolff also provided much appreciated insights and guidance during preparation of dissertation related research. I also thank J. Catalano, P. Crowley, D. Giammar, B. Jolliff, and J. Pasteris for participating on the dissertation committee. The McDonnell Center for the Space Sciences provided funding for this research through a McDonnell Center Fellowship and NASA provided funding through the NASA Graduate Student Researchers Program. I thank the Johns Hopkins University Applied Physics Laboratory for participation in acquisition and analysis of CRISM data.

TABLE OF CONTENTS

Abstract ii
Acknowledgements iv
List of Figures vi
List of Tables viii
Chapter 1 – Introduction 1
References 3
Chapter 2 – Retrieval of Atmospherically Corrected Hyperspectral CRISM Surface Reflectance Spectra Using DISORT Radiative Transfer Modeling: Comparison to Empirical 'Volcano Scan' Correction Method 5
2.1 Introduction 5
2.2 Background 6
2.3 CRISM Lambert Albedo Retrieval Algorithms 15
2.4 Atmospheric Correction Results 17
2.5 Discussion 24
Figures 26
References 50
Chapter 3 – Phyllosilicate and Sulfate-Hematite Deposits within Miyamoto Crater in Southern Sinus Meridiani, Mars 52
3.1 Introduction 52
3.2 Geologic Context 53
3.3 Spectral Reflectance Retrievals, Analysis, and Mapping 54
3.4 Miyamoto Crater Interior Materials 55
3.5 Discussion and Implications 57
Figures 59
References 65
Chapter 4 – Spectral and Stratigraphic Mapping of Hydrated Sulfate and Phyllosilicate-bearing Deposits in Northern Sinus Meridiani, Mars 68
4.1 Introduction 68
4.2 Geologic Context 69
4.3 Data Sets and Methods 76
4.4 Spectral and Stratigraphic Mapping in Northern Sinus Meridiani 83
4.5 Discussion 96
4.6 Conclusion 109
Figures 111
Tables 162
References 163
Chapter 5 – Synthesis 171
References 174
Appendix A – List of CRISM Images Utilized in Chapter 4 175

LIST OF FIGURES

2.1 – Terrestrial mineral spectra and spectral features in the Martian atmosphere ...26
2.2 – CO_2, CO, and H_20 gas absorptions ...27
2.3 – Single scattering albedo for dust and ice aerosols ...28
2.4 – CRISM transmission spectra...29
2.5 – I/F and Lambert Albedo lookup tables ...30
2.6 – High resolution I/F spectrum ...31
2.7 – Wavelength offset, 0.6 nm...32
2.8 – Over and under correction of gases ...33
2.9 – Lambert Albedo retrievals for wavelength offsets of 0.2 and 0.6 nm ...34
2.10 – CRISM single Gaussian and summation of three Gaussians bandpass models ...35
2.11 – Lambert Albedo retrieval with random noise ...37
2.12 – Lambert Albedo retrievals using temperature profiles ± 10 K ...38
2.13 – Effect of aerosol optical depth on I/F intensity...39
2.14 – Lambert Albedo retrievals for multiple dust opacities ...40
2.15 – Synthetic I/F transmission spectra ...42
2.16 – DISORT simulated volcano scan correction...43
2.17 – CRISM volcano scan correction ...46
2.18 – DISORT simulated volcano scan correction, total opacity = 0 ...47
2.19 – Transmittance versus column density...48
2.20 – CRISM Lambert Albedo retrieval and volcano scan corrected spectra...49
3.1 – Context map, Miyamoto crater ...59
3.2 – 2.3 μm parameter map, Miyamoto crater ...60
3.3 – CRISM spectrum extracted from phyllosilicate-bearing deposits in Miyamoto crater...62
3.4 – Polygonally fractured material in Miyamoto crater...64
4.1 – Geologic context maps of Sinus Meridiani...111
4.2 – Selected spectra of terrestrial minerals ...113
4.3 – Geologic context maps of northern Sinus Meridiani ...115
4.4 – Detailed map of study region in northern Sinus Meridiani...116
4.5 – CRISM and OMEGA parameter maps ...119
4.6 – Detailed look at CT and ET1 in the northern portion of the study area...121
4.7 – CRISM spectra extracted from selected FRT images...123
4.8 – False color composite of CRISM image FRT000099C8 and parameter map...124
4.9 – Dark mantle on ET1 near 30 km diameter crater...125
4.10 – Dark mantle on ET1 ...127
4.11 – Detailed look at $ET1_B$ and $ET1_C$ ...129
4.12 – False color composite of CRISM image FRT000097F8 and parameter map...131
4.13 – CRISM spectra extracted from selected FRT images...133
4.14 – $ET1_A$ exposed in cliff wall...134
4.15 – Detailed look at eastern portion of study area ...136

4.16 – False color composite of CRISM image FRT0000CC22 and parameter map....138
4.17 – Units map and topographic map of valley....140
4.18 – High elevation LHS deposits....142
4.19 – False color composite of CRISM image FRT00004616 and parameter map....144
4.20 – False color composite of CRISM image FRT00006541 and parameter map....146
4.21 – CRISM Lambert albedo spectra extracted from FRT00004616....148
4.22 – Mesas in center of valley....149
4.23 – LHS deposits on western valley floor....151
4.24 – Hydrated sulfates....153
4.25 – False color composite of CRISM image FRT0000893E and parameter map....154
4.26 – CRISM spectra extracted from selected FRT images....156
4.27 – False color composite of CRISM image FRT000062E6 and parameter map....158
4.28 – False color composite of CRISM image FRT00003CE0 and parameter map draped on MOLA topography....159
4.29 – Cross sections generated from MOLA topographic profiles....161

LIST OF TABLES

4.1 – Spectral Parameters.....162

CHAPTER 1 – INTRODUCTION

Knowledge of Martian geology and surface properties is derived from analyses of orbital remote sensing observations together with ground truth measurements for a limited number of locations on the Martian surface. Atmospheric correction of data acquired from orbit is necessary for proper interpretation of surface spectral properties in the visible and near infrared wavelength regions. Investigations presented in this dissertation utilize recently acquired near infrared spectral data from the Mars Reconnaissance Orbiter (MRO) Compact Reconnaissance Imaging Spectrometer for Mars (CRISM) [*Murchie et al.,* 2007] in conjunction with other datasets to better understand the aqueous history of deposits in the Sinus Meridiani region of Mars. An extensive analysis is presented on methods for the retrieval of atmospherically corrected CRISM surface Lambert Albedo spectra using Discrete Ordinate Radiative Transfer modeling [*Stamnes et al.,* 1988] and artifacts generated by atmospheric correction area detailed. Detailed stratigraphic and spectral analyses are performed with the goal of identifying and mapping the mineralogy and stratigraphy of sedimentary deposits to infer the aqueous history of the Sinus Meridiani region on Mars. Datasets utilized include MRO CRISM, MRO Context Imager (CTX) [*Malin et al.,* 2007], MRO High Resolution Imaging Science Experiment (HiRISE) [*McEwen et al.,* 2007] Mars Express (MEX) Observatoire pour la Minéralogie, l'Eau, les Glaces et l'Activité (OMEGA) [*Bibring et al.,* 2004], MEX High Resolution Stereo Camera (HRSC) [*Neukum et al*., 2004], Mars Odyssey (ODY) Thermal Emission Imaging System (THEMIS) [*Christensen et al.,* 2004], ODY Mars Orbital Camera (MOC) [*Malin et al.,* 1992], and ODY Mars Orbiter Laser Altimeter (MOLA) [*Smith et al.,* 2001] data.

This dissertation is divided into five chapters. The first chapter introduces the scope and motivations for investigations presented in chapters two, three, and four. Chapters two, three, and four have been prepared for publication and contain relevant introductory material and dataset descriptions [*Wiseman et al*., 2008; *Wiseman et al*., 2009; *Wiseman et al*., 2009a]. The lead author on all three papers, S. M. Wiseman, was primarily responsible for analyses and text preparation. S. M. Wiseman's academic advisor, R. E. Arvidson, provided critical guidance and review during the preparation of the dissertation research. Other coauthors provided expert advice and reviewed draft manuscripts.

Chapter two describes the retrieval of atmospherically corrected surface Lambert Albedo spectra from CRISM I/F spectra (where I/F is the radiance at sensor (I) divided by the solar irradiance (F) at the top of the Martian atmosphere divided by π) using Discrete Ordinate Ratiative Transfer (DISORT) modeling. Model results are used to identify artifacts that can be generated by atmospheric correction, including the commonly used empirical method that employs division by a scaled transmission spectrum derived from high and low altitude observation on Mars. Atmospheric correction is necessary for proper interpretation of surface spectral properties. Chapters three and four focus on mapping the mineralogy and stratigraphy of deposits in Sinus Meridiani. Spectral analyses presented in chapters three and four focus on detection and identification of hydrated and/or hydroxylated alteration minerals in the near infrared region between ~1.0 and 2.5 μm. Chapter five presents a synthesis of results detailed in chapters two, three, and four.

REFERENCES

Bibring, J.-P., A. Soufflot, M. Berthé, Y. Langevin, B. Gondet, P. Drossart, M. Bouyé, M. Combes, P. Puget, A. Semery, G. Bellucci, V. Formisano, V. Moroz, V. Kottsov, G. Bonello, S. Erard, O. Forni, A. Gendrin, N. Manaud, F. Poulet, G. Poulleau, T. Encrenaz, T. Fouchet, R. Melchiori, F. Altieri, N. Ignatiev, D. Titov, L. Zasova, A. Coradini, F. Capacionni, P. Cerroni, S. Fonti, N. Mangold, P. Pinet, B. Schmitt, C. Sotin, E. Hauber, H. Hoffmann, R. Jaumann, U. Keller, R. E. Arvidson, and F. Forget, OMEGA: Observatoire pour la Minéralogie, l'Eau, les Glaces et l'Activite´, in *Mars Express: The Scientific Payload*, edited by A. Wilson, pp. 37-49, Eur. Space Agency Spec. Publ., Noordwijk, The Netherlands, 2004.

Christensen, P. R. (2004), The Thermal Emission Imaging System (THEMIS) for the Mars 2001 Odyssey mission, *Space Sci. Rev.*, *110*, 85-1doi:10.1023/B:SPAC.0000021008.16305.94.

Malin, M. C., J. F. Bell III, B. A. Cantor, M. A. Caplinger, W. M. Calvin, R. T. Clancy, K. S. Edgett, L. Edwards, R. M. Haberle, B. J. PhIL1ips, S. W. Lee, M. A. Ravine, P. C. Thomas, and M. J. Wolff (2007), Context Camera Investigation on board the Mars Reconnaissance Orbiter, *J. Geophys. Res*, *112*, E05S04, doi:10.1029/2006JE002808.

Malin, M. C. (1992), Mars Observer Camera, *J. Geophys. Res*, *97*, 7699-7718.

McEwen, A. S., E. M. Eliason, J. W. Bergstrom, N. T. Bridges, C. J. Hansen, W. A. Delamere, J. A. Grant, V. C. Gulick, K. E. Herkenhoff, L. Keszthelyi, R. L. Kirk, M. T. Mellon, S. W. Squyres, N. Thomas, and C. M. Weitz (2007), Mars Reconnaissance Orbiter's High Resolution Imaging Science Experiment (HiRISE), *J. Geophys. Res*, *112*, E05S02, doi:10.1029/2005JE002605.

Murchie, S., R. E. Arvidson, P. Bendini, K. Beisser, J.-P. Bibring, J. Bishop, J. Boldt, P. Cavender, T. Choo, R. T. Clancy, E. H. Darlington, D. Des Marais, R. Espiritu, D. Fort, R. Green, E. Guinness, J. Hayes, C. Hash, K. Heffernan, J. Hemmler, G. Heyler, D. Humm, J. Hutchenson, N. Izenberg, R. Lee, J. Lees, D. Lohr, E. Malaret, T. Martin, J. A. McGovern, P. McGuire, R. V. Morris, J. F. Mustard, S. Pelkey, E. Rhodes, M. Robinson, T. Roush, E. Schafer, G. Seagrave, F. P. Seelos, IV, S. Slavney, M. Smith, W.-J. Shyong, K. Stohbehn, H. Taylor, P. Thompson, B. Tossman, M. Wirzburger, and M. Wolff (2007), Compact Reconnaissance Imaging Spectrometer for Mars (CRISM) on Mars Reconnaissance Orbiter (MRO), *J. Geophys. Res*, *112*, E05S03, doi:10.1029/2006JE002682.

Neukum, G., R. Jaumann, and H. C.-I. a. E. Team, HRSC: The High Resolution Stereo Camera of Mars Express, in *Mars Express: The Scientific Payload*, edited by A. Wilson, pp. 17-35, Eur. Space Agency Spec. Publ., Noordwijk, The Netherlands, 2004.

Smith, D. E., M. T. Zuber, H. V. Frey, J. B. garvin, J. W. Head, D. O. Muhlemann, G. H. PettenfIL1, R. J. PhIL1ips, S. C. Solomon, H. J. Zwally, W. B. Banerdt, T. C. Duxbury, M. P. Golombek, F. G. Lemoine, G. A. Neumann, D. D. Rowlands, O. Aharonson, P. G. Ford, A. B. Ivanov, C. L. Johnson, P. J. McGovern, J. B. Abshire, R. S. Afzal, and X. Sun (2001), Mars Orbiter Laser Altimeter:

Experiment summary after the first year of global mapping of Mars, *J. Geophys. Res*, *106*(E10), 23689-23722.

Stamnes, K., S. Tsay, W. Wiscombe, and K. Jayaweera (1988), Numerically stable algorithm for discrete-ordinate-method radiative transfer in multiple scattering and emitting layered media, *Appl. Opt.*, *27*, 2502-2509.

Wiseman S. M., R. E. Arvidson, J. C. Andrews-Hanna, R. N. Clark, N. L. Lanza, D. Des Marais, G. A. Marzo, R. V. Morris, S. L. Murchie, H. E. Newsom, E. Z. Noe Dobrea, A. M. Ollila, F. Poulet, T. L Roush, F. P. Seelos, G. A. Swayze (2008), Phyllosilicate and sulfate-hematite deposits within Miyamoto crater in southern Sinus Meridiani, Mars, *Geophys. Res. Lett*., 35, L19204, doi:10.1029/2008GL035363.

Wiseman, S.M., R. E. Arvidson, R. V. Morris, F. Poulet, S. L. Murchie, F. P. Seelos, J. L. Bishop, J. C. Andrews-Hanna, D. Des Marais, J. L. Griffes (2009), Spectral and stratigraphic mapping of hydrated sulfate and phyllosilicate-bearing deposits in northern Sinus Meridiani, Mars, *J. Geophys. Res*, in revision.

Wiseman, S.M., R. E. Arvidson, R. V. Morris, F. Poulet, S. L. Murchie, F. P. Seelos, J. L. Bishop, J. C. Andrews-Hanna, D. Des Marais, J. L. Griffes (2009a), Retrieval of atmospherically corrected hyperspectral CRISM surface reflectance spectra using DISORT radiative transfer modeling: Comparison to the empirical volcano scan correction method, *J. Geophys. Res*, in prep.

CHAPTER 2 – RETRIEVAL OF ATMOSPHERICALLY CORRECTED HYPERSPECTRAL CRISM SURFACE REFLECTANE SPECTRA USING DISORT RADIATIVE TRANSFER MODELING: COMPARISON TO THE EMPIRICAL VOLCANO SCAN CORRECTION METHOD

2.1 Introduction

Atmospheric correction of data acquired by the Mars Reconnaissance Orbiter (MRO) Compact Reconnaissance Imaging Spectrometer for Mars (CRISM) is important for interpretation of surface spectral properties because of the of the presence of scattering and absorbing aerosols particles and absorbing gases in the Martian atmosphere. Analyses of CRISM data in this paper are limited to the wavelength range between 450 and 2650 nm in which reflected solar radiation dominates the signal. Atmospheric contributions from both aerosols and gases are important in this wavelength region. Relatively intense CO_2 absorptions occur in portions of the spectrum near which vibrational features produced by OH and H_2O in hydrated and/or hydroxylated minerals can occur (Figure 2.1). H_2O and CO in the atmosphere produce shallower spectral features (Figure 2.2). Dust aerosol contributions are most pronounced at shorter wavelengths (< 700 nm) in areas were Fe^{3+} mineralogy dominates spectral features. Ice aerosols have absorption features near 1500 and 2000 nm (Figure 2.3). The spectral slope between ~1000 and 2650 nm, which is important for interpreting broad spectral features resulting from electronic transitions in Fe^{2+} bearing minerals, is also affected by the presence of atmospheric aerosols (Figure 2.1).

In this paper we describe retrieval of atmospherically corrected surface Lambert Albedo spectra using Discrete Ordinate Radiative Transfer (DISORT) modeling. The DISORT model calculates aerosol, gas, and surface contributions simultaneously [*Stamnes et al.,* 1988; *Thomas and Stamnes,* 2002]. We also simulate the commonly used empirical volcano scan correction method, which employs division by a scaled transmission spectrum derived from high and low altitude observation on Mars [*Langevin et al*., 2005]. Model results are used to identify artifacts that can be generated by improper or incomplete atmospheric correction.

2.2 Background

2.2.1 CRISM Dataset

The CRISM spectrometer aboard MRO is a hyperspectral imager that operates between 360 and 3960 nm and is capable of acquiring both hyperspectral (544 channels) and multispectral (72 channel subset) images [*Murchie et al.,* 2007]. The CRISM instrument is mounted on a gimbal platform that allows acquisition of off nadir images and ground tracking of a target. Targeted hyperspectral images, referred to as full resolution targeted (FRT), half resolution long (HRL), and half resolution short (HRS), are utilized in Lambert Alebdo retrievals. FRT images are acquired at a spatial resolution of 20 m/pixel and HRL and HRS images are binned spatially by a factor of two, resulting in a spatial resolution of 40 m/pixel. FFC images, or hyperspectral images acquired with nadir pointing, are used for flatfield calibration. Transmission spectra utilized in the volcano scan correction are also derived from FFC images.

A sequence of 11 images, termed an emission phase function (EPF) sequence, is acquired for each targeted image. EPF sequences include 5 incoming images acquired at emergence angles between ~70 and 30°, one central scan that is continuously gimbaled over a range of ~15 to -15°, and five outgoing images with emergence angles between ~ -30 and -70°. The incoming and outgoing images are spatially binned by a factor of 10, but the central swath (image number 07) of the targeted EPF sequence is returned at full or half spatial resolution. Our Lambert Albedo retrievals are applied to the high resolution central swath.

The CRISM spectrometer has two detector arrays, termed the 'S' and 'L' detectors, that operate between 360 and 1006 nm and 1003 and 3960 nm, respectively. Each detector array is 2-dimensional and acquires data over 640 across track pixels for each channel. The along track dimension is built up mainly by orbital motion, resulting in 3-dimensional image cubes. As a result of using a 2-dimensional detector, the central wavelength position of each channel changes as a function of column, causing spectral 'smile'. For a given column, the wavelength center ranges by ± 7 nm relative to the wavelength of the central column. Spectral bandpass shapes also vary with column.

CRISM instrument response function information, including wavelength center and bandpass coefficients for each column for each channel, is contained in 'WA' and 'SB' Calibration Data Records (CDRs) that are available through the Planetary Data System (PDS). Prelaunch channel centers and bandpasses shapes were derived from laboratory measurements. Bandpass shapes for CRISM columns near the center of the detector are more symmetrical than those further from the center. The SB CDR contains coefficients that define the bandpass shape in terms of a single Gaussian model as well as

a more complicated summation of three Gaussians model. Comparison of wavelength centers of gas bands in Martian spectra measured by CRISM to modeled atmospheric gas absorptions revealed that a wavelength shift of ~2 nm relative to ground measurements occurred subsequent to the launch of MRO. SB and WA CDRs were updated to reflect this change by adding a constant wavelength offset of ~2 nm to all channels in all columns. However, a relatively small (< 1.5 nm) temperature dependent wavelength shift that is not currently reflected in the WA and SB CDR files occurs in CRISM data [*Smith et al.,* 2009]. For each CRISM channel, warmer instrument temperatures experienced during the perihelion season lead to a shift toward higher wavelengths and colder instrument temperatures during aphelion result in a shift toward lower wavelengths [*Smith et al*., 2009]. This long term trend is perturbed by short term variations in instrument temperature caused by the orbital cycle and solar induced heating. The wavelength shift is assumed to be the result of slight changes in the position of a grating in response to thermal conditions within the CRISM instrument housing.

With the exception of a few bad channels and other known artifacts, the current calibration version, TRR2, of CRISM I/F data (where I/F is the radiance, I, at sensor divided by the solar irradiance, F, at the top of the Martian atmosphere divided by π) is well calibrated over our wavelength region of interest, from ~440 to 2650 nm [*Murchie et al*., 2007]. A typical flatfield correction to account for relatively small detector element response variations in the detector is applied to CRISM data at the end of the calibration pipeline [*Murchie et al*., 2007]. The application of a flatfield correction to wavelength regions within intense gas absorptions is complicated by the presence of spectral smile because spectral intensity can vary dramatically over a few tenths of nm. Therefore, a

flatfield correction to CRISM data was applied only to wavelengths outside of major gas absorptions.

Ancillary data, including the incidence angle (*i*), emergence angle (*e*), phase angle (*g*), latitude, and longitude for each pixel, can be found in Derived Data Record (DDR) files that are generated for each CRISM observation and released to the PDS. Mars Orbiter Laser Altimeter (MOLA) elevation data are also contained in the DDR file. Image acquisition time and other parameters, including the solar distance and solar elevation (Ls), are defined in CRISM PDS label files that accompany each data product.

2.2.2 Radiative Transfer Model

Radiative transfer modeling utilizes public domain Discrete Ordinate Ratiative Transfer (DISORT) code [*Stamnes et al*., 1998; *Thomas and Stamnes*, 2002]. DISORT is a general purpose Fortran program for discrete-ordinate-method radiative transfer in scattering and emitting layered media. The atmosphere is treated as a plane-parallel medium in which individual layers are homogenous but interlayer properties can be varied. The numerical implementation is discussed in *Stamnes et al*., [1999]. We utilized 'front-end' routines optimized for study of the Martian atmosphere, DISORT_multi, to compute synthetic I/F spectra [*Wolff et al*., 2009].

2.2.2.1 Disort_multi Model Inputs

DISORT_multi is a flexible package in which multiple parameters and preferences can be defined. Results of this model have been compared with other code and agree to within ± 1 % [*Wolff et al*., 2009]. The following description of model inputs

focuses on our investigations and is not a comprehensive overview of the capabilities of DISORT_multi. Synthetic I/F spectra are calculated that would be observed at the top of the atmosphere for user defined viewing geometry (*i*, *e*, and *g*) and surface parameter(s) as a result of attenuation and scattering of the solar beam down through the atmosphere, interaction with the surface, and attenuation and scattering up through the atmosphere. Absorption, emission, and multiple scattering from atmospheric gases and aerosols are accounted for.

Gas absorptions for CO_2, CO, and H_2O are defined using correlated-k distributions with parameters derived from the HITRAN database [*Rothman et al.,* 2005]. Gas contributions resampled to CRISM resolution are shown in Figure 2.2. For our purposes, the correlated-k inputs are generated at a wavelength sampling of 0.2 nm. Total water vapor is specified in precipitable micrometers and a water column is constructed in which the saturation value is used to limit the mixing ratio in a given atmospheric layer. Lambert Albedo retrievals in this paper focus on observations for which dust is the dominant atmospheric aerosol. Dust aerosol single scattering albedos for 1.5 μm particles and wavelength dependent phase functions utilized in our modeling were derived from analysis of CRISM hyperspectral data [*Wolff et al*., 2009] (Figure 2.3). Ice aerosol parameters for 2 and 4 μm sized particles [*Clancy et al*., 2003] are also shown in Figure 2.3. Dust is assumed to be well mixed throughout the atmosphere and ice (if present) is assumed to be well mixed above the level of water condensation.

Atmospheric temperature profiles relevant to atmospheric conditions at the latitude, longitude, and Ls of a CRISM observation of interest are derived from historical Mars Global Surveyor (MGS) Thermal Emission Spectrometer (TES) observations of

Mars acquired between 1998 and 2000 [*Smith*, 2004]. Surface pressure is calculated using fits to the diurnal pressure variations determined from Viking lander data [*Tillman et al*., 1993] and scaled by elevation. Pressure (*P*) at each atmospheric layer is calculated from the integration of the hydrostatic equation.

$$P(z) = P(z_0)\, e^{-(z-z_o)/(\frac{RT}{mg})}, \quad (2.1)$$

where *z* is height, *T* is temperature, and *R*/*mg* is the gas constant divided by the mean molecular mass of Martian air multiplied by the acceleration due to gravity on Mars.

Aerosol optical depth inputs appropriate for atmospheric conditions at the time of image acquisition can be estimated from TES climatologic values [*Smith* 2004; 2008], derived from CRISM EPF sequences [*Wolff et al*., 2009], or calculated from concurrent Thermal Emission Imaging Spectrometer (THEMIS) observations [*Smith et al*., 2009]. In addition, total optical depth measurements made at 880 nm by the Mars Exploration Rover (MER) rovers are available near the Spirit and Opportunity landing sites [*Lemmon et al*., 2004].

2.2.3 Empirical Volcano Scan Correction

The volcano scan correction was originally implemented by the Mars Express Observatoire pour la Minéralogie, l'Eau, les Glaces et l'Activité (OMEGA) team as a means to remove large atmospheric gas absorption features with minimal computational investment [*Langevin et al., 2005*]. This method utilizes a scaled transmission spectrum derived from low and high altitude observations in which different path lengths through the atmosphere are measured (Figure 2.4). Atmospheric transmission files derived from CRISM FFC data acquired at the base and summit of Olympus Mons are contained in AT

CDR files that are available from the PDS. Software is available through the PDS that automatically applies the volcano scan correction to each pixel of each column of a CRISM image using the transmission spectrum from the appropriate column of the AT CDR. Several AT CDR files have been developed in an effort to sample multiple different wavelength shift positions of the CRISM instrument. Although atmospheric aerosol contributions were variable among the Olympus Mons observations, a long wavelength slope correction was applied to the transmission spectra in the AT CDR files in an effort to normalize the shapes of the transmission spectra.

Transmittance between the base and summit of Olympus Mons, T_v, is determined using the integrated form of the Beer-Lambert-Bougher Law, such that

$$T_v(\lambda) = I_\lambda(s_{0\to2}) / I_\lambda(s_{0\to1}) = e^{-ks_{1\to2}}, \quad (2.2)$$

where the opacity (τ) is defined as

$$\tau = ks_{1\to2}, \quad (2.3)$$

and I_λ is equivalent to the CRISM I/F at some wavelength (λ), $s_{0\to1}$ is the total path length traversed from the top of the atmosphere (s_0) to some vertical distance s_1 within the atmosphere, $s_{0\to2}$ is the total path length traversed from the top of the atmosphere (s_0) to some distance s_2 within the atmosphere, k is the absorption coefficient of the optically active species. It is implicit in equation (2.1) that the surface contribution to $I_\lambda(s_{0\to1})$ and $I_\lambda(s_{0\to2})$ is identical. For measurements of the surface acquired at the top of the Martian atmosphere, the total path length is a sum of the incoming and outgoing paths. The amount of absorbing particles in a given path length varies by Ls as a result of the CO_2 cycle on Mars [*Tillman et al*., 2003]. In the presence of both scattering and absorbing

molecules, the total opacity (τ) is the sum of the absorbing (τ_{abs}) and scattering (τ_{scat}) optical depths, that is,

$$\tau = \tau_{abs} + \tau_{scat}. \quad (2.4)$$

The contribution from τ_{scat} is assumed to be negligible in the high and low altitude spectra used to generate the transmission spectrum. Although the transmittance (T) outside of gas bands should be equal to 1, in practice, the ratio of the low and high altitude data is scaled by a constant factor so that the derived transmission spectrum is equal to 1 at 2240 nm, a wavelength that has no appreciable gas absorption (Figure 2.4b).

To perform the volcano scan correction, a target CRISM spectrum acquired with an arbitrary atmospheric path length, s_3, is divided by an exponentially scaled version of the derived transmission spectrum. Calculating the exponential scaling factor relies on band depth estimates. The band depth of an absorption feature in the target spectrum and the band depth of the same feature in the derived transmission spectrum are proxies for the transmittance that occurred over the atmospheric path lengths traversed for the target spectrum and the derived transmission spectrum, respectively.

$$BD_{targ} = I_{feature}(target)/I_{continuum}(target), \quad (2.5)$$

assuming $T=1$ on the continuum,

$$BD_{targ} = I_{feature}(s_{0\rightarrow3})/I_{continuum} = e^{-ks_{0\rightarrow3}}. \quad (2.6)$$

Similarly,

$$BD_{trans} = I_{feature}(trans)/I_{continuum}(trans), \quad (2.7)$$

$$BD_{trans} = I_{feature}(s_{1\rightarrow2})/I_{continuum} = e^{-ks_{1\rightarrow2}}. \quad (2.8)$$

The exponential scaling factor is determined by taking the natural logarithm of the band depths, such that

$$\ln(BD_{targ}) \;/\; \ln(BD_{trans}) = \ln(e^{-ks_{0\to3}}) \,/\, \ln(e^{-ks_{1\to2}}) \;=\; s_{0\to3}/s_{1\to2}. \quad (2.8)$$

An estimate of the band depth of the strongest CO_2 band in the CO_2 triplet near 2000 nm is commonly calculated as the ratio of the slope corrected I/F value along the continuum at ~1900 nm to the I/F value in the CO_2 absorption band at ~2010 nm. *McGuire et al*., [2009] note that variations in the surface spectral contribution between the wavelength along the continuum and the wavelength of the CO_2 absorption feature can cause error in the calculated band depth and instead suggest using the ratio of the I/F value at 1980 nm to the I/F value of the CO_2 absorption band at ~2010 nm. These two band depth estimates will be referred to as the BD1 and BD2 estimates, respectively.

Applying the volcano scan correction to the target spectrum of interest, remembering that

$$I_\lambda(s_{0\to3}) = I_\lambda(s_0) * e^{-ks_{0\to3}}, \quad (9)$$

results in

$$I_{feature}(s_0)e^{-ks_{0\to3}} \;/\; (e^{-ks_{1\to2}})^{s_{0\to3}/s_{1\to2}} = I_{feature}(s_0), \quad (10)$$

where $I_{feature}(s_0)$ is the CRISM I/F value corrected for gas absorption, provided that all assumptions implicit in the volcano scan correction were met.

The CRISM target spectrum over all wavelengths is corrected using the exponential scaling factor that is determined from the band depth of the intense CO_2 at ~2010 nm because there is a high signal contribution and therefore less impact from noise in this channel. Scaling the entire transmission spectrum by a constant exponential factor is only appropriate if the absorption coefficient, *k*, does not change as a function of column density.

2.3 CRISM Lambert Albedo Retrieval Algorithms

For our investigations, we assumed a Lambertian surface. The Lambert Albedo (A_L) is defined as

$$A_L = \pi^* I / (F^*\cos(i)), \quad (2.11)$$

where I is the radiance, F is the solar irradiance, and *i* is the solar incidence angle. Lambertian surfaces are isotropic, that is, they scatter light evenly in all directions. Methods described in this paper can be adapted to solve for more complicated surface functions, including the semi-empirical Hapke function [*Hapke*, 1993].

Synthetic Martian I/F spectra are generated using DISORT_multi. For each set of atmospheric conditions and viewing geometries, model data area calculated for multiple surface Lambert Albedos. A lookup table is generated between modeled I/F and Lambert Albedo that is used to retrieve Lambert Albedo spectra from CRISM I/F spectra. Lambert Albedo spectra are atmospherically corrected surface spectra in which both aerosol and gas contributions have been removed.

2.3.1 Lookup Table

For diffuse atmospheric conditions, the relationship between modeled I/F and input Lambert Albedo is approximately linear for a given wavelength (Figure 2.5). A first order estimate of the Lambert Albedo of a Martian surface can be determined by dividing CRISM I/F by the cosine of the incidence angle, *i*. Synthetic I/F spectra are generated for Lambert Albedos that are ± 0.05 of the estimated Lambert Albedo in order to minimize the χ^2 error of the linear fit. CRISM I/F values are mapped to Lambert

Albedos using the linear equations generated from the synthetic I/F spectra, for each CRISM channel, for each column.

2.3.2 Calculation of CRISM Wavelength Offset

Detailed knowledge of the CRSM instrument response function is important to properly model regions of strong gas absorption. The shape of the gas features measured is a convolution of very narrow gad bands and the CRISM instrument response function (Figure 2.6). Because of the temperature dependent wavelength shift and the presence of spectral smile we solve for CRISM band centers for each image using the strongest gas band centered at ~2010 nm. A constant offset is assumed across channels. It is possible that the wavelength shift is not constant across channels, but because CO_2 bands at wavelengths shorter than 2010 nm span fewer channels and are relatively weaker, more error is associated with wavelength calculations using other gas absorption features. This makes it difficult to determine if there is a significant channel dependent wavelength shift. Wavelength offsets calculated relative to the WA CDR are small (< 2 nm) and do vary slightly with column. The column dependence of the wavelength shift that we calculate likely compensates for a combination of small inaccuracies in the laboratory derived center wavelengths and the time/temperature dependent wavelength shift. We assume that the bandpass shape has not changed following laboratory calibration and use parameters from the summation of three Gaussians model fits given in the SB CDR.

In order to calculate wavelength centers, high resolution synthetic I/F spectra are generated with a wavelength sampling of 0.4 nm. The continuum level of the CRISM I/F spectrum across the ~2010 nm gas bands in defined as a linear fit to 3 channels outside

gas absorptions, near 1800 nm and 3 channels near 2200 nm. These continuum I/F values are converted to Lambert Albedos using the look up table approach. The synthetic high resolution spectra are convolved with CRISM bandpasses that are systematically offset by 0.1 nm for ± 2.0 nm relative to the nominal channel center (Figure 2.7). Lookup tables between resampled synthetic I/F and Lambert Albedo are used to generate I/F spectra across the ~2010 nm gas absorption band, for each wavelength offset. The correlation between the 5 bands near the deepest part of the absorption feature in the CRISM I/F spectrum and the synthetic I/F spectra are compared and the wavelength offset that results in the largest correlation coefficient is determined.

The relative value of the correlation coefficient as a function of wavelength offset is fairly insensitive to moderate variations in the surface pressure used to generate the synthetic I/F spectra. The same wavelength center ± 0.1 nm was retrieved in experiments where the model surface pressure was varied by ± 10 %. Error caused by variations in surface spectra relative to the assumed continuum is minimized by using channels in which absorption from CO_2 dominates. In addition, the ~2010 nm CO_2 band is outside of strong spectral absorption features caused by H_2O that occur near 1900 nm (Figure 2.1).

2.4 Atmospheric Correction Results

2.4.1. Lambert Albedo Spectra

Erroneous correction of CO_2 bands results in obvious positive or negative features in Lambert Albedo retrievals (Figure 2.8). Improper corrections of H_2O vapor or CO cause more subtle artifacts because these absorption features are relatively weaker compared to most CO_2 features (Figure 2.2). Small wavelength offsets between the

target spectrum, or CRISM I/F spectrum to be converted to a Lambert Albedo spectrum, and I/F spectra used to generate Lambert Albedo lookup tables results in high frequency artifacts, or 'hash', near gas bands (Figures 2.9a, 2.9b). These artifacts occur for relatively small wavelength offsets because the derivative changes rapidly as a function of wavelength near CO_2 absorptions (Figure 2.9c). The magnitude of the 'hash' depends on the position of the center of the CRISM bandpass relative to the position of strong lines in the gas band. For some CRISM columns, small wavelength offsets have a relatively greater affect on the magnitude than larger wavelength offsets.

Changes to gas bands are observed in high resolution synthetic I/F spectra resampled to CRISM bandpasses using parameters from the two different bandpass models contained in the SB CDR files (Figures 2.10a, 2.10b). Differences in gas band shape resulting from resampling to CRISM bandpasses using the two different bandpass models is more noticeable in columns near the edge of the detector because the actual bandpass shapes are less symmetrical in these columns [*Murchie et al.,* 2007]. Incorrect knowledge of bandpass shapes also results in 'hash' near gas bands in retrieved Lambert Albedo spectra (Figures 2.10c, 2.10d).

Noise in the CRISM dataset is complicated and includes column dependent effects as well as random noise [*Parente*, 2008]. The temperature of the detector during data acquisition affects the amount of thermally induced noise in CRISM images. The method of Lambert Albedo retrieval used in this paper is sensitive to noise (Figure 2.11). Flatfield corrections outside of gas bands are on the order of 0 to ± 1.5 % for most CRISM channels in our wavelength range of interest [*Murchie et al*., 2007]. The lack of a viable flatfield correction in CRISM I/F spectra over wavelengths that have large gas

absorptions is expected to contribute to errors in Lambert Albedo retrievals near gas bands.

Inaccuracies in model atmospheric temperature inputs can contribute to relatively small artifacts near the main CO_2 triplet at 2000 nm. Temperature profiles derived from TES are accurate to within ± 10 K [*Smith*, 2004]. Dust loading in the atmosphere is important for solar insulation on Mars [*Smith*, 2008]. Temperature profiles in the TES climatology database (for the proper Ls and lat/lon) are appropriate to use for modeling atmospheric conditions that occured during acquisition of CRISM data so long as the aerosol opacity recorded in the TES climatological database is similar to the opacity at the time of acquisition of the CRISM observation of interest. Adjusting the atmospheric temperature profile by a constant value of ± 10 K has a small effect on the quality of the Lambert Albedo retrievals (Figure 2.12).

Lambert Albedo retrievals in this paper focus on observations for which dust is the dominant aerosol. Dust aerosol contributions affect the slope and brightness of Martian spectra (Figure 2.13). Multiple scattering caused by aerosol particles brightens I/F spectra of dark surfaces and darkens spectra of bright surfaces (Figure 2.13). The total aerosol contribution mediates the amplitude of this effect. Ice aerosols, if present, also cause absorption features near 1500 and 1900 nm that appear similar to absorption features in spectra of some hydrated minerals (Figure 2.1).

In addition to modulating the amplitude and long wavelength shape of the Lambert Albedo retrievals, aerosols affect retrievals in gas bands because the total opacity is a combination of the absorbed and scattered component (Equation 2.4). There is a tradeoff between the amount of aerosols modeled and the surface pressure needed to

minimize residual CO_2 features in Lambert Albedo retrievals. For example, if a low dust opacity is assumed, lower modeled pressures are needed to minimize residuals associated with CO_2 features. Conversely, if a high dust opacity is used, higher modeled pressures are necessary to minimize the residual (Figure 2.14). Optical depths can vary widely from year to year on Mars for a given Ls. Therefore, optical depth values in the TES climatology may not be representative of atmospheric conditions that occurred during acquisition of CRISM images.

2.4.2. Volcano Scan Corrected Spectra

Two assumptions are implicit in deriving a transmission spectrum from the ratio of the high and low altitude Martian spectra. The surface materials at the base and summit of Olympus Mons are assumed to be spectrally identical and the total opacity, τ, is assumed to result only from gas absorption, that is, the scattering contribution from aerosols is negligible. If both of these assumptions are met, then the transmittance (T) outside of gas bands should be equal to 1. This is not the case, and the ratio of the low and high altitude data is scaled by a constant factor. The adjusted transmission spectra contained in the AT CDRs are fairly close to unity at wavelengths outside of gas absorptions (Figure 2.4b).

Given that the measurements at the base and summit of Olympus Mons used to generate the transmission spectra are separated by approximately 6° in latitude (~350 km), it is unlikely that surfaces materials at these two locations are spectrally identical. The assumption that gas absorption dominates is more appropriate during low aerosol opacity conditions on Mars than high opacity conditions. Variable aerosol contributions

to spectra acquired at the base and summit of Olympus Mons are expected. The amount of aerosol particles in a well mixed atmosphere decreases with decreasing pressure and aerosol concentrations are spatially variable on Mars [*Smith*, 2004]. Differences in surface spectral characteristics and/or aerosol contributions between the spectra acquired at the base and the summit of Olympus Mons lead to deviations from unity outside of gas bands in the derived transmission spectrum.

In order to explore potential artifacts generated by application of the volcano scan correction, we simulated the volcano scan correction using synthetic I/F spectra generated for atmospheric profiles appropriate for the base and summit of Olympus Mons using DISORT_multi. Transmission spectra were generated from these synthetic data using the technique outlined in section 2.2.3. Multiple simulations were performed in which aerosol and surface parameters were adjusted. Figure 2.15a shows simulated results that have a transmission spectrum that is similar in shape to CRISM transmission spectra shown in Figure 2.4. For simplicity, the surface spectral contribution was assumed to be linear as a function of wavelength and the volcano scan correction was applied to the low altitude spectrum from which the transmission spectrum was generated. BD1 and BD2 band depth estimates were utilized to calculate the constant exponential scaling factor applied during the volcano scan correction. Residual gas band features are evident in the simulated volcano scan corrected data (Figure 2.15b). Applying the scaling factor calculated using the BD1 estimate results in 'hash' near 2000 nm caused by over correction of some parts of the CO_2 triplet, even though undercorrection of weaker CO_2 bands is evident at other wavelengths (Figures 2.16). Applying the scaling factor calculated using the BD2 estimate results in undercorrection of the CO_2 triplet near 2000

nm that has the appearance of a broad artifact with some high frequency 'hash' (Figure 2.16). The addition of noise to the simulation (Figure 2.16) reduces the structured appearance of the residual gas bands but does not mask them. Similar artifacts are evident in volcano scan corrected CRISM spectra. Figure 2.17 shows an example of a CRISM volcano scan corrected spectrum in which a transmission spectrum derived from FFC00008608 was applied to an I/F spectrum extracted from FFC00008608 near the base of Olympus Mons. This example is analogous to the simulation shown in Figure 2.16. The complication due to artifacts introduced by the time/temperature dependent wavelength shift is negated by application of the transmission spectrum to a target spectrum acquired in the same image.

Residual gas features are also evident in DISORT simulated volcano scan corrected data in which all assumptions inherent in the volcano scan correction were met, that is, the surface spectral contributions in the low and high altitude spectral were identical and the aerosol opacity was set to 0 so that the total opacity, τ, resulted only from gas absorption (Figure 2.18). The magnitudes of the residual gas features vary with wavelength and depend on the value of the constant exponential scaling factor that was applied during the volcano scan correction.

These residual gas band artifacts occur because scaling the entire transmission spectrum by a constant exponential factor is not physically correct. Gas bands contain many individual absorption lines which have variable strengths. Each line has a spectral profile that peaks at the line center and less absorption occurs in the line wings. A detailed discussion of gas line properties and the curve of growth in the context of radiative transfer modeling can be found in *Thomas and Stamnes*, [2002]. In the weak

line limit ($\tau << 1$), or linear regime, the absorptance ($1 - T$) is proportional to the amount of absorbing molecules. In the strong line limit ($\tau >> 1$), or saturated regime, there is a square root dependence on the column density. In between these two limits, the absorption coefficient (k) is constant and an exponential relationship between absorptance and column density is observed. For the combination of pressures that occur in the Martian atmosphere (< ~9 mbars) and gas line strengths in our wavelength region of interest (450 to 2650 nm), both the linear and exponential regimes are important (Figure 2.19). As a result of CRISM spectral resolution, CRISM channels near gas absorptions sample multiple gas lines of variable intensities. The spectral resolution and spacing of CRISM data impacts the shape of the residual features observed in volcano scan corrected data.

2.4.3 Comparison Lambert Albedo and Volcano Scan Corrected Spectra

Atmospherically corrected spectra retrieved using results from DISORT radiative transfer modeling and the empirical volcano scan correction for a CRISM I/F spectrum extracted from an observation covering the Gusev plains near the MER Spirit landing site are shown in Figure 2.20. The long frequency spectral shape of the two spectra shown in Figure 2.20 is variable. Aerosol contributions are corrected for in the Lambert Albedo spectra. Both spectra exhibit artifacts near the 2000 nm CO_2 triplet. More 'hash' near small gas bands is evident in the Lambert Albedo spectrum than the volcano scan corrected spectrum. This 'hash' originates as a result of several factors. As discussed in section 2.3.2, the time/temperature dependent wavelength shift that occurs in CRISM data is assumed to be constant across channels. As part of the Lambert Albedo retrieval

process, this wavelength shift is calculated. However, if the wavelength shift is not constant or if bandpass shapes are not know with a high fidelity, then 'hash' near gas bands is expected to occur in Lambert Albedo retrievals as a result of the mismatch in shape between the synthetic I/F spectra and the CRISM I/F spectrum near gas bands. Although the time/temperature dependent wavelength offset is also a factor in the volcano scan correction, knowledge of bandpass shapes is not.

2.5 Discussion

To summarize, aerosol and gas atmospheric contributions are calculated in this paper using DISORT radiative transfer modeling. Accurate retrieval of atmospherically corrected Lambert Albedo surface spectra requires detailed knowledge of atmospheric conditions at the time of image acquisition. Artifacts that can be induced by inaccurate atmospheric inputs were characterized. Time/temperature dependent wavelength shifts that have a large impact on removal of gas bands are calculated and incorporated into the Lambert Albedo retrieval algorithm. Lambert Albedo retrievals near gas bands are surprisingly sensitive to the shape of the instrument response function used to resample high spectral resolution DISORT synthetic I/F spectra to CRISM spectral sampling.

The empirical volcano scan correction approach to remove atmospheric gas bands is much less computationally intensive than radiative transfer modeling. Artifacts caused by inaccuracies in preflight laboratory data are not a factor because instrument specific factors, including instrument response functions, are inherent in the derived transmission spectrum employed in the volcano scan correction. Aerosols contributions, which influence the magnitude and long frequency spectral slope, are not accounted for in the

volcano scan correction method. A constant exponential factor is used to scale the transmission spectrum during application of the volcano scan correction in the current implementation of this method. Because the relationship between opacity and the density of absorbing molecules in the optical path changes from exponential to linear as the opacity decreases into the optically thin ($\tau << 1$) regime, a constant exponential scaling factor is inappropriate. Residual gas bands are evident in volcano scan corrected data that can mimic the appearance of surface spectral features near 2000 nm. Thus, as originally noted by *Langevin et al.,* [2005], the empirical volcano scan correction should be considered as a first order method for retrieval of surface reflectance.

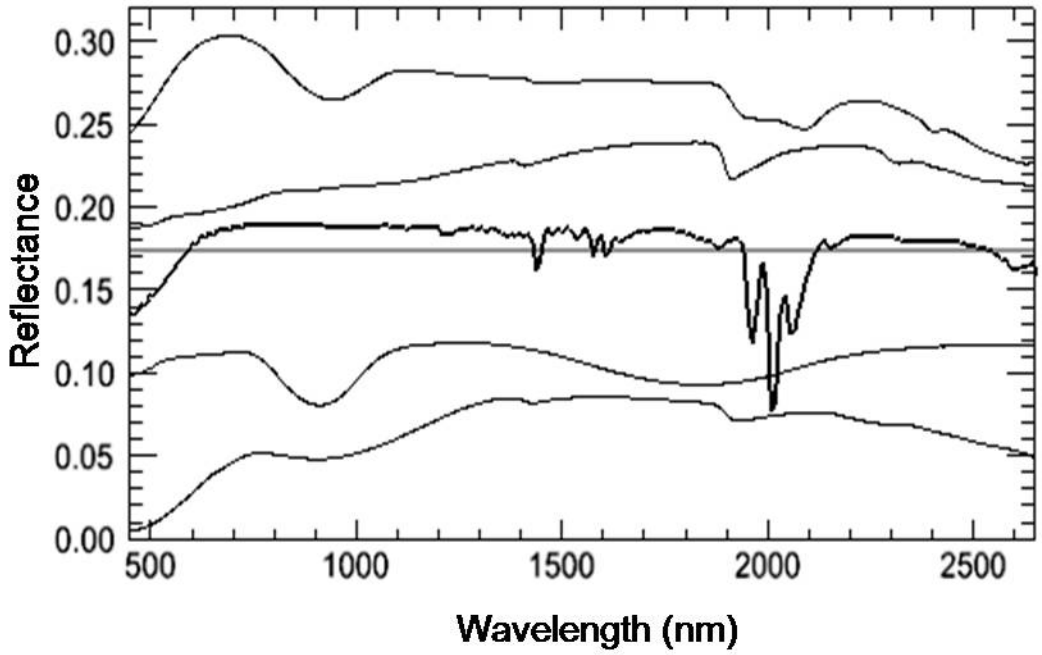

Figure 2.1. Laboratory reflectance spectra (arbitrarily scaled and offset) of multiple minerals from the publically available CRISM spectral library [*CRISM Science Team*, 2006] are plotted with fine black lines. Spectra from top to bottom: szomolnokite, saponite, hyperthene, and ferrihydrite. The bold black line shows a synthetic I/F spectrum that would be observed at the top of the atmosphere for a surface with a Lambert Albedo of 0.2 at all wavelengths with a viewing geometry of i = g = 30, e = 0 (bold gray line).

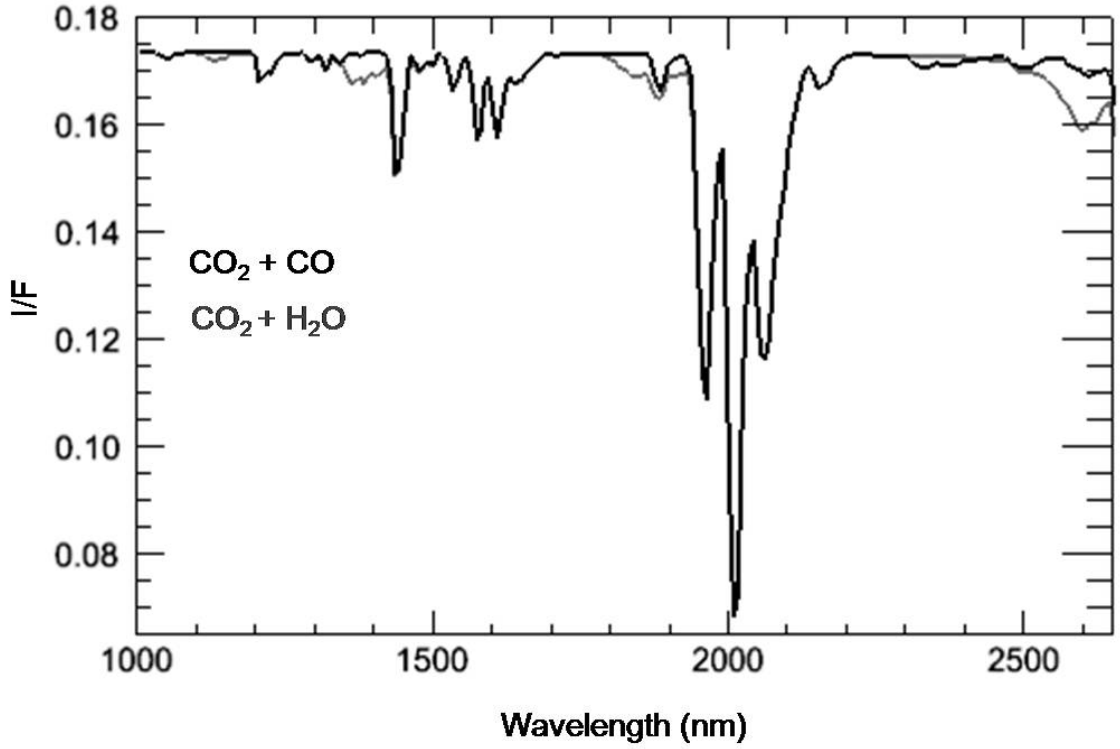

Figure 2.2. Black line: Synthetic I/F spectrum showing CO_2 + CO gas absorptions resampled to CRISM spectral resolution. Gray line: Synthetic I/F spectrum showing CO_2 + H_2O gas absorptions resampled to CRISM spectral resolution. Synthetic spectra were generated for a surface Lambert Albedo of 0.2 at all wavelengths with a viewing geometry of i = g = 30, e = 0.

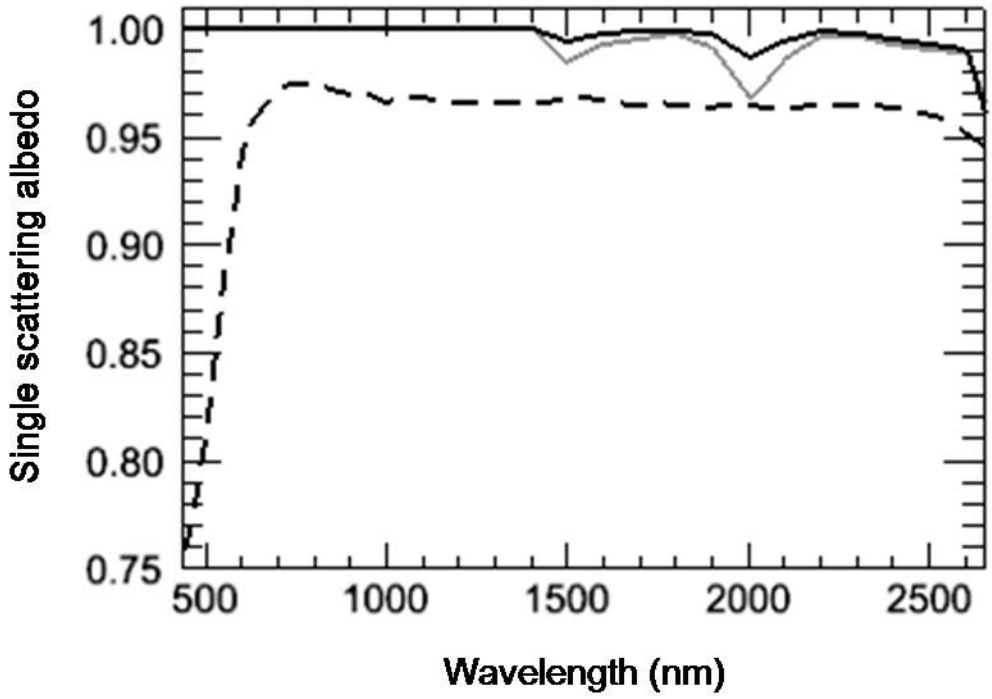

Figure 2.3. Single scattering albedo for 1.5 μm dust aerosol particles (dashed line) [*Wolff et al.,* 2009], 2 μm ice aerosol particles (solid black line), and 4 μm ice aerosol particles (solid gray line) [*Clancy et al.,* 2003].

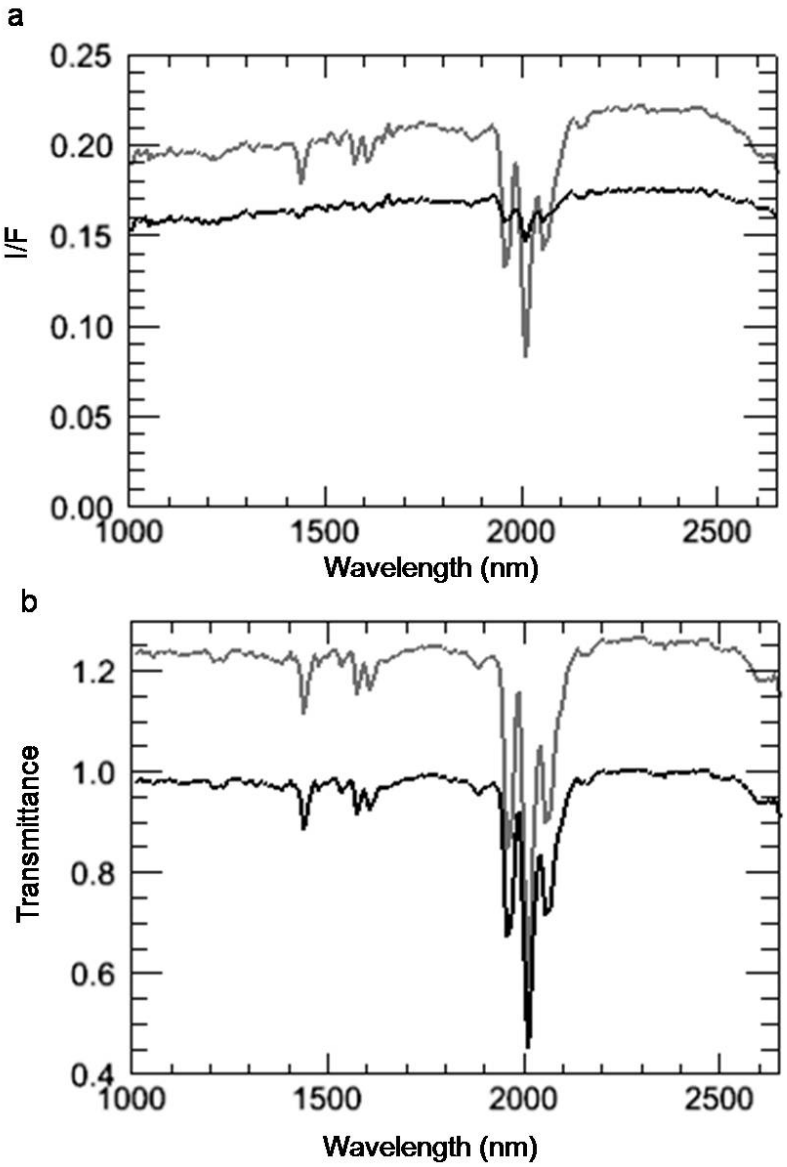

Figure 2.4. a) Low and high altitude spectra acquired at the base and summit of Olympus Mons, shown in gray and black, respectively, extracted from column 300 of FFC000061C4. b) Unscaled (gray line) and scaled (black line) versions of the transmission spectrum generated from spectra shown in part a).

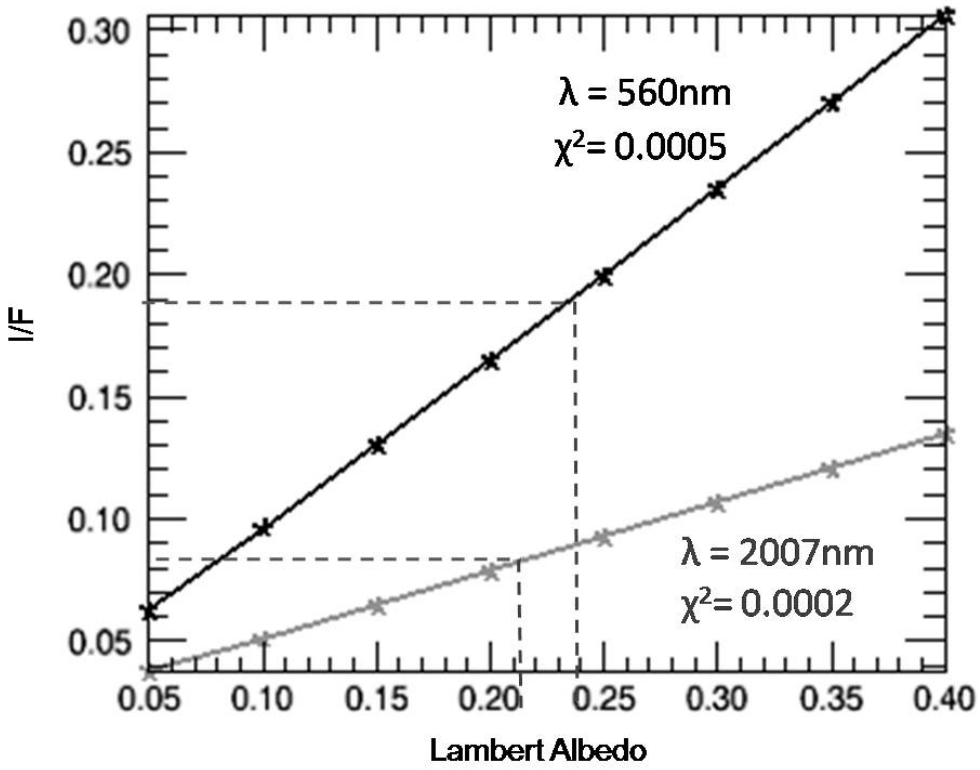

Figure 2.5. Examples of look up tables between I/F and Lambert Albedo for wavelengths at 560 nm and 2007 nm. The error between the line fit values (y) and the actual values (f) is given by $\chi^2 = \sum[(y - f)/f]^2$.

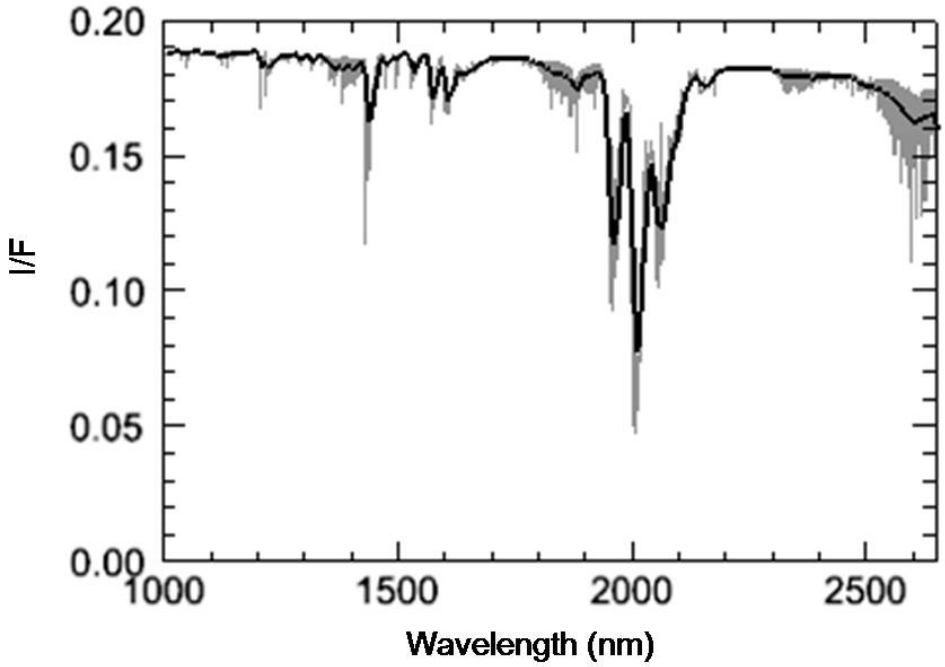

Figure 2.6. Gray line: Synthetic I/F spectrum with spectral sampling of 0.4 nm, generated from correlated-k inputs with a wavelength spacing of 0.2 nm. Black line: High resolution gray spectrum resampled to CRISM spectral resolution at column 300. Synthetic spectra were generated for a surface Lambert Albedo of 0.2 at all wavelengths, a dust opacity of 0.6 at 900 nm, and a viewing geometry of i = g = 30, e = 0.

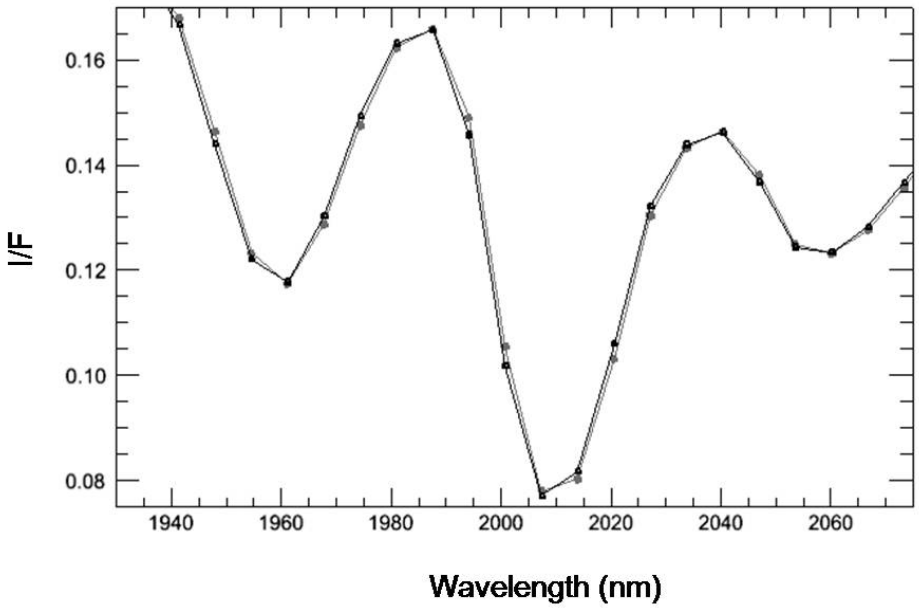

Figure 2.7. Black line: High resolution synthetic I/F spectrum resampled to spectral resolution for CRISM column 300. Gay line: High resolution synthetic I/F spectrum resampled to spectral resolution for CRISM column 300, offset by 0.6 nm. Synthetic spectra were generated for a surface Lambert Albedo of 0.2 at all wavelengths, a dust opacity of 0.6 at 900 nm, and a viewing geometry of i = g = 30, e = 0.

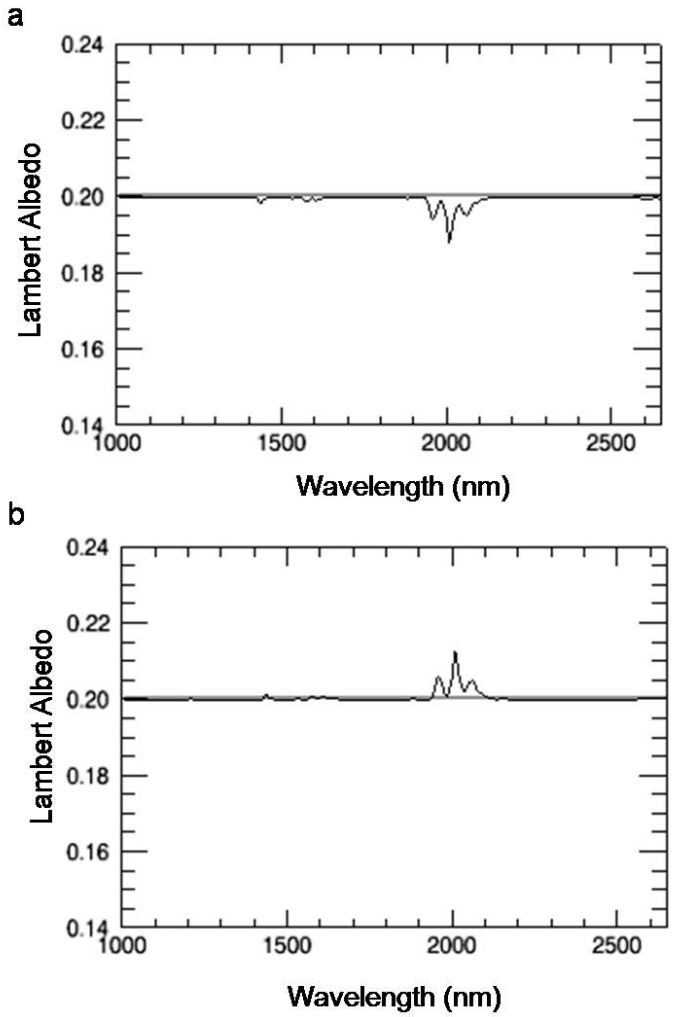

Figure 2.8. a) Lambert Albedo retrieval with 95 % of actual surface pressure. Gray line: Input surface spectrum. b) Lambert Albedo retrieval with 105 % of actual surface pressure. Gray line: Input surface spectrum. Synthetic spectra were generated for a surface Lambert Albedo of 0.2 at all wavelengths, a dust opacity of 0.6 at 900 nm, and a viewing geometry of i = g = 30, e = 0.

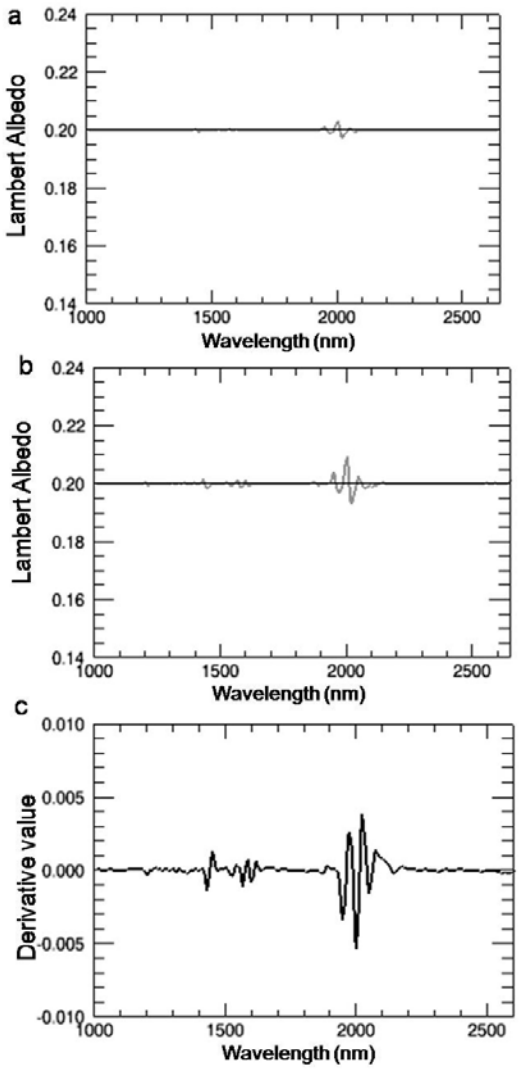

Figure 2.9. a) Lambert Albedo retrieval for a synthetic I/F spectrum resampled to CRISM column 300 bandpasses with a wavelength offset of 0.2 nm applied. Gray line: Input surface spectrum. b) Lambert Albedo retrieval for a synthetic I/F spectrum resampled to CRISM column 300 bandpasses with a wavelength offset of 0.6 nm applied. Gray line: Input surface spectrum. c) Derivative of synthetic I/F spectrum used in Lambert Albedo retrievals. Synthetic spectra were generated for a surface Lambert Albedo of 0.2 at all wavelengths, a dust opacity of 0.6 at 900 nm, and a viewing geometry of i = g = 30, e = 0.

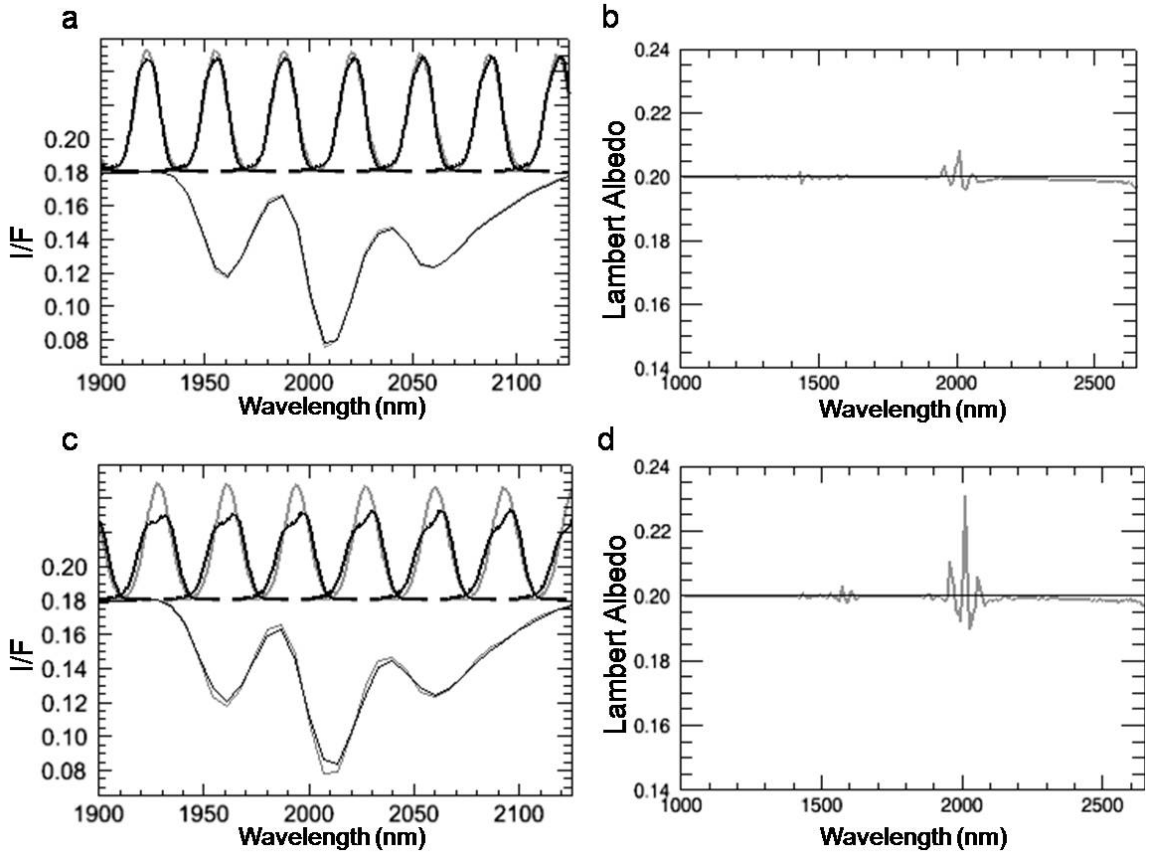
a
b
c
d
I/F
Lambert Albedo
Wavelength (nm)
0.20
0.18
0.16
0.14
0.12
0.10
0.08
0.24
0.22
1900
1950
2000
2050
2100
1000
1500
2500

Figure 2.10. a) Summation of three Gaussians (heavy black line) and single Gaussian (gray line) CRISM bandpass models, shown for every fifth CRISM channel in column 300. Thin gray line: High resolution synthetic I/F spectrum resampled to CRSIM single Gaussian bandpass model for column 300. Thin black line: High resolution synthetic I/F spectrum resampled to CRSIM three Gaussians bandpass model for column 300. b) Gray Line: Lambert Albedo retrieval for synthetic I/F spectrum resampled to CRISM bandpasses using the three Gaussians model and retrieved using synthetic I/F spectra resampled to CRISM bandpasses using the single Gaussian model. Black line: Lambert Albedo of input surface. c) Summation of three Gaussians (heavy black line) and single Gaussian (gray line) CRISM bandpass models, shown for every fifth CRISM channel in column 100. Thin gray line: High resolution synthetic I/F spectrum resampled to CRSIM single Gaussian bandpass model for column 100. Thin black line: High resolution synthetic I/F spectrum resampled to CRSIM three Gaussians bandpass model for column 100. d) Gray Line: Lambert Albedo retrieval for synthetic I/F spectrum resampled to CRISM bandpasses using the three Gaussians model and retrieved using synthetic I/F spectra resampled to CRISM bandpasses using the single Gaussian model. Black line: Lambert Albedo of input surface.

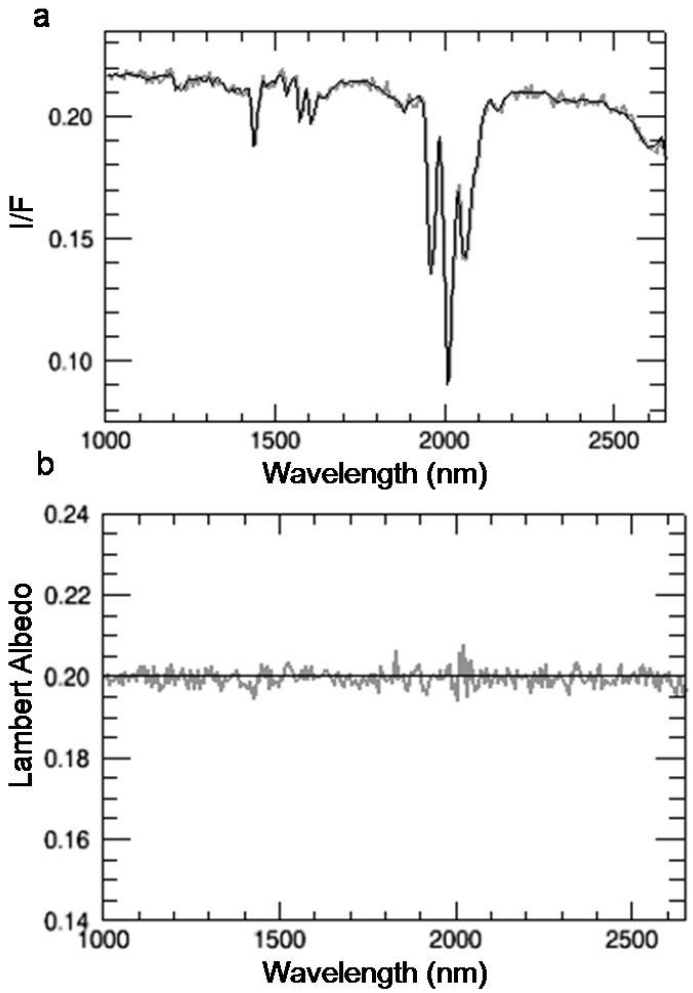

Figure 2.11. a) Synthetic I/F spectrum (black line) generated for a surface Lambert Albedo of 0.2 at all wavelengths, a dust opacity of 0.6 at 900 nm, and a viewing geometry of i = g = 30, e = 0. Gray line: Synthetic I/F spectrum shown in black, but with Gaussian random noise added that has a standard deviation of 0.0015. b) Lambert albedo retrievals for input black and gray synthetic I/F spectra shown in part a).

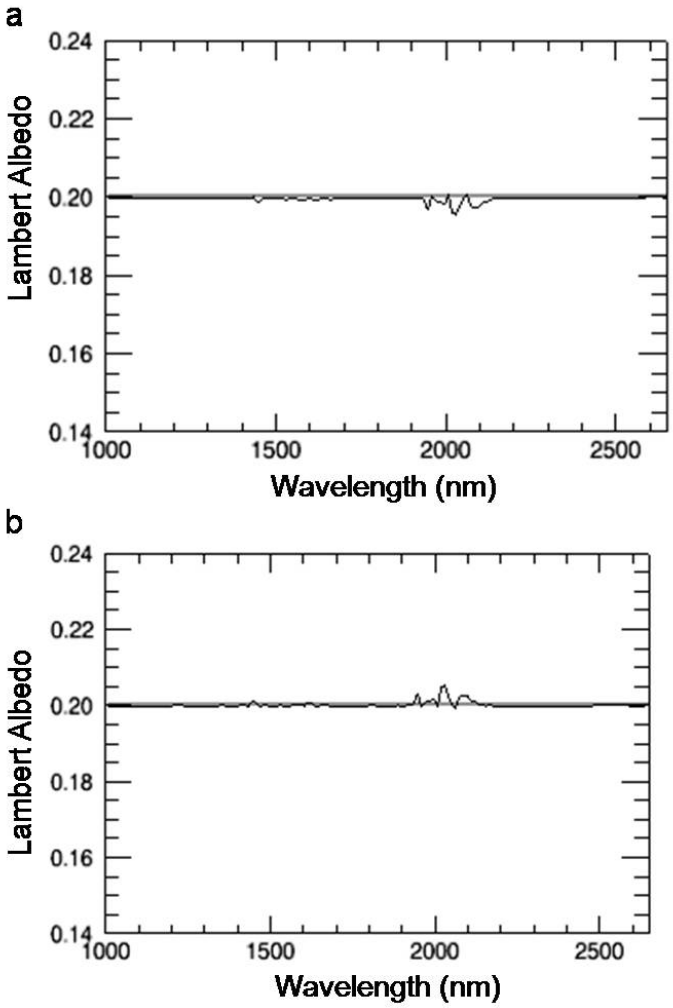

Figure 2.12. a) Black line: Lambert Albdo retrieval using a temperature profile adjusted by -10 K. Gray line: Input Lambert Albedo surface spectrum. b) Black line: Lambert Albdo retrieval using a temperature profile adjusted by +10 K. Gray line: Input Lambert Albedo surface spectrum. Synthetic I/F spectra were generated for a surface Lambert Albedo of 0.2 at all wavelengths, a dust opacity of 0.6 at 900 nm, and a viewing geometry of i = g = 30, e = 0.

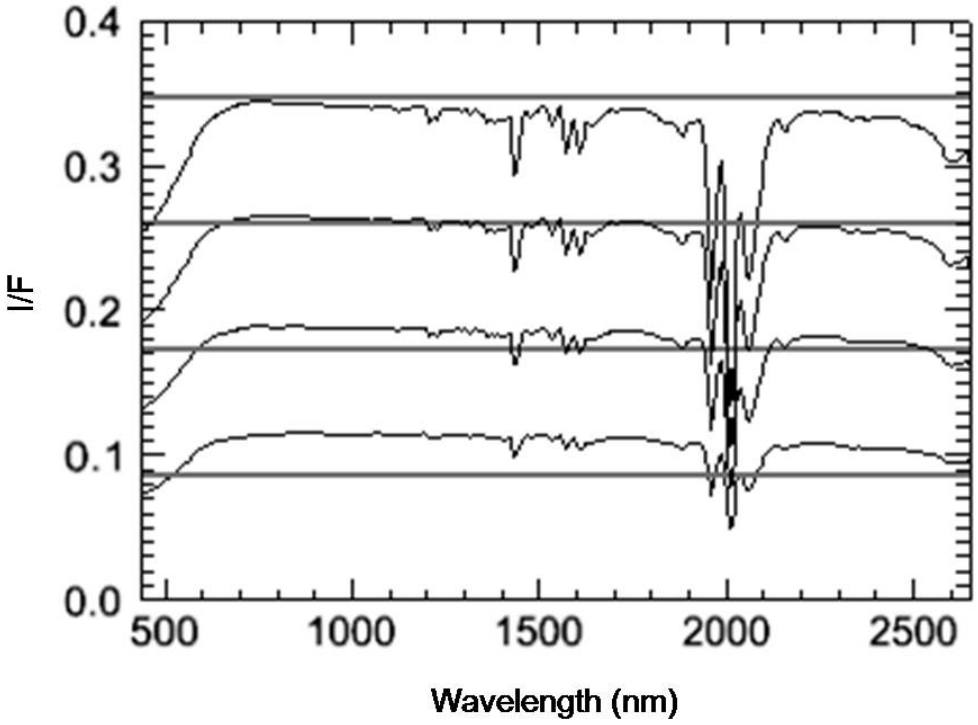

Figure 2.13. Synthetic I/F spectra (black lines) for input surface spectra shown by thick gray lines. Input Lambert Albedos for gray lines, from top to bottom are 0.4, 0.3, 0.2, and 0.1. Synthetic spectra were generated using a dust opacity of 0.6 at 900 nm and a viewing geometry of i = g = 30, e = 0.

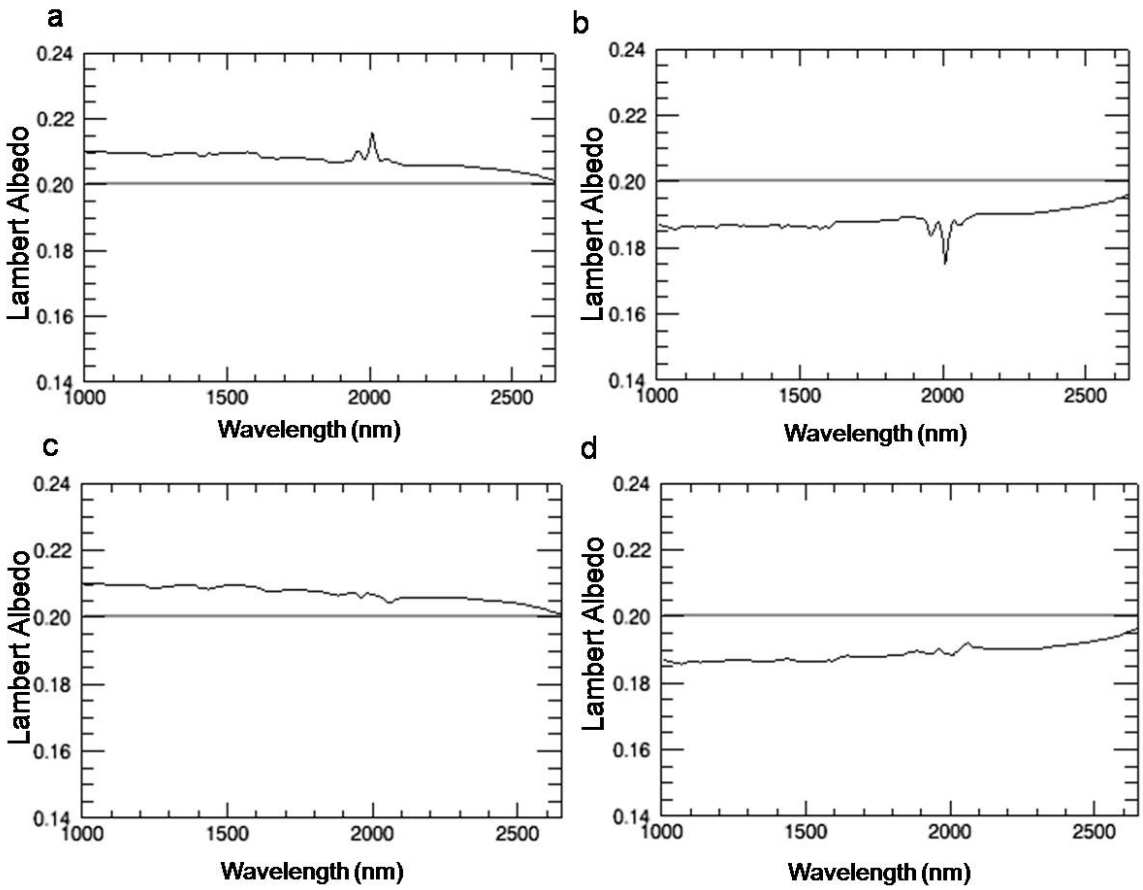
a
b
c
d
Lambert Albedo
Wavelength (nm)
0.24
0.22
0.20
0.18
0.16
0.14
1000
1500
2000
2500

Figure 2.14. Synthetic I/F spectra were generated for a surface Lambert Albedo of 0.2 at all wavelengths, a modeled dust opacity of 0.6 at 900 nm, and a viewing geometry of i = g = 30, e = 0. a) Black line: Lambert Albedo retrieval using a modeled dust opacity of 0.3. Gray line: Input Lambert albedo spectrum. b) Black line: Lambert Albedo retrieval using a modeled dust opacity of 0.3 and 96 % of the the nominal surface pressure. Gray line: Input Lambert albedo spectrum. c) Black line: Lambert retrieval using a modeled dust opacity of 0.9. Gray line: Input Lambert albedo spectrum. d) Black line: Lambert Albedo retrieval using a modeled dust opacity of 0.9 and 105 % of the nominal surface pressure. Gray line: Input Lambert albedo spectrum.

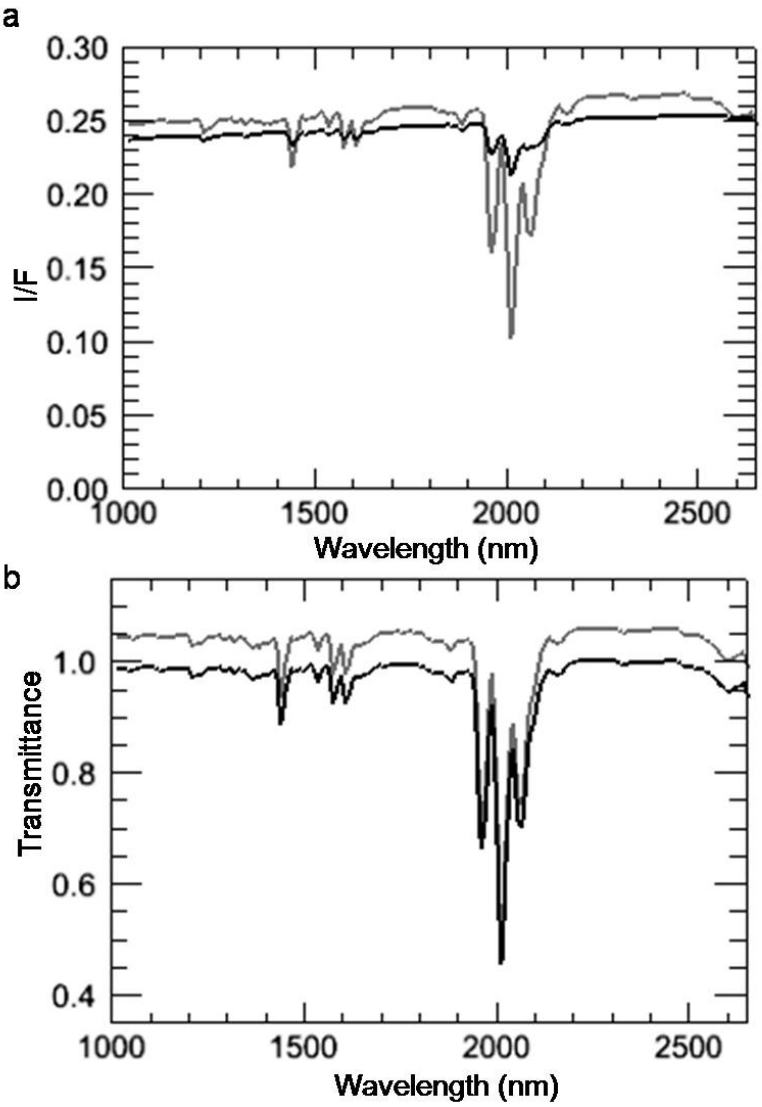

Figure 2.15. a) Low and high altitude synthetic I/F spectra modeled using pressure/temperature profiles appropriate for the base and summit of Olympus Mons, shown in gray and black, respectively. A dust opacity of 0.3 was used to generate the high altitude spectrum and a dust opacity of 0.6 was used to generate the low altitude spectrum. 5 precipitable μm of water were modeled for the low altitude spectrum. b) Unscaled (gray line) and scaled (black line) versions of the transmission spectrum generated from spectra shown in part a).

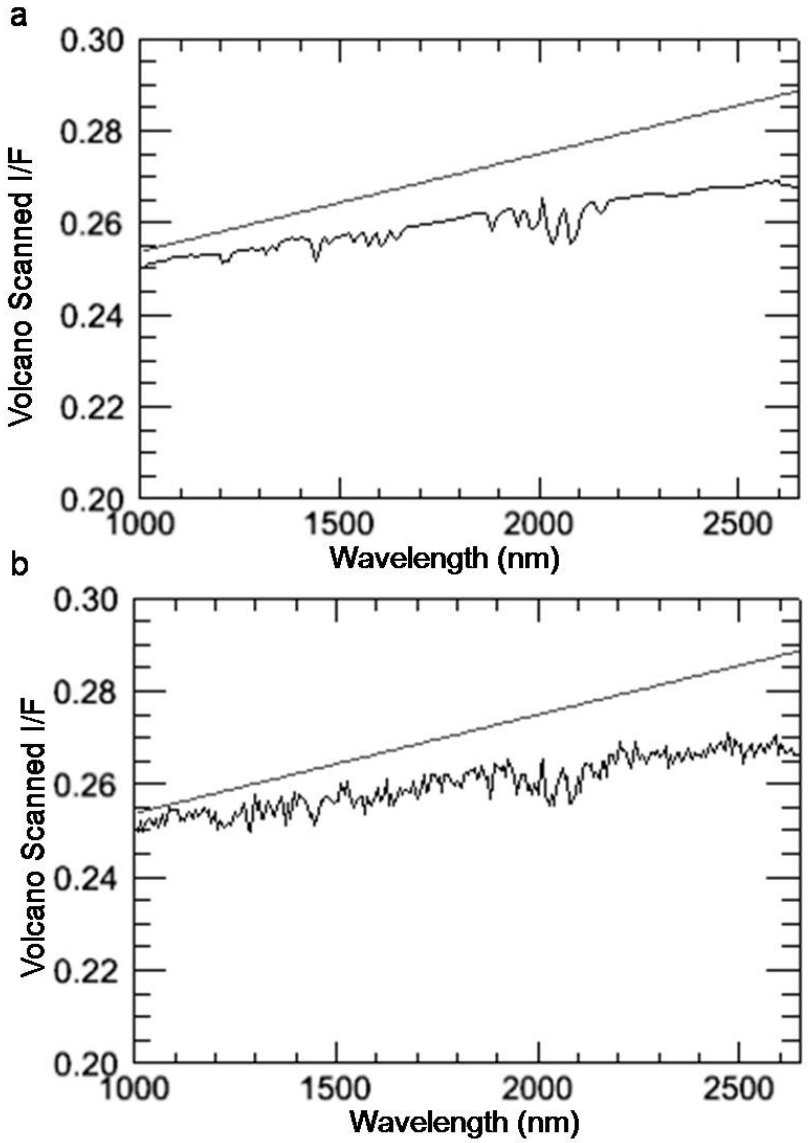
a
0.30
0.28
0.26
0.24
0.22
0.20
Volcano Scanned I/F
1000
1500
2000
2500
Wavelength (nm)
b
0.30
0.28
0.26
0.24
0.22
0.20
Volcano Scanned I/F
1000
1500
2000
2500
Wavelength (nm)

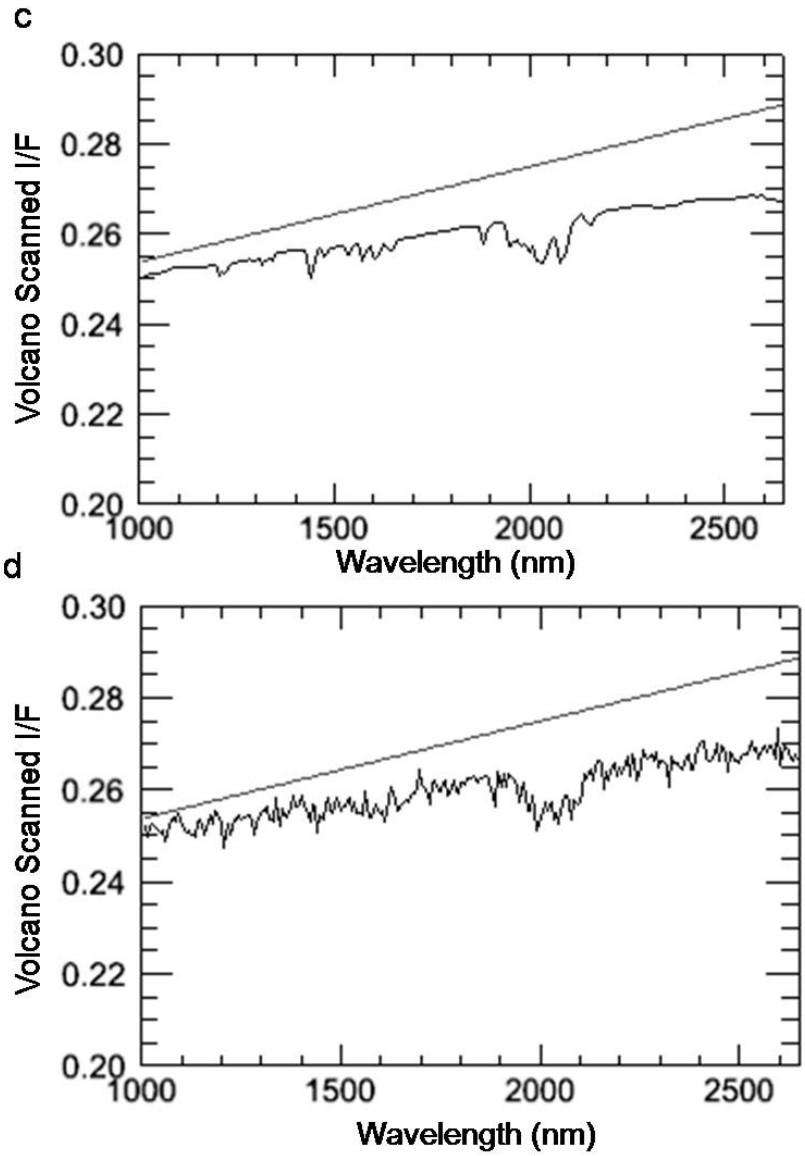
c
0.30
0.28
0.26
0.24
0.22
0.20
Volcano Scanned I/F
1000
1500
2000
2500
Wavelength (nm)
d
0.30
0.28
0.26
0.24
0.22
0.20
Volcano Scanned I/F
1000
1500
2000
2500
Wavelength (nm)

Figure 2.16. a) Black line: Simulated volcano scan correction applied to the low altitude spectrum shown in gray in Figure 2.15a using a constant exponential scaling factor of 1.21. The scaling factor was calculated using the BD1 estimate. Gray line: Input surface Lambert Albedo spectrum. b) Simulation shown in part a) but with random Gaussian noise added. c) Black line: Simulated volcano scan correction applied to the low altitude spectrum shown in gray in Figure 2.15a using a constant exponential scaling factor of 1.17. The scaling factor was calculated using the BD2 estimate. Gray line: Input Lambert Albedo surface spectrum. d) Simulation shown in part c) but with random Gaussian noise added.

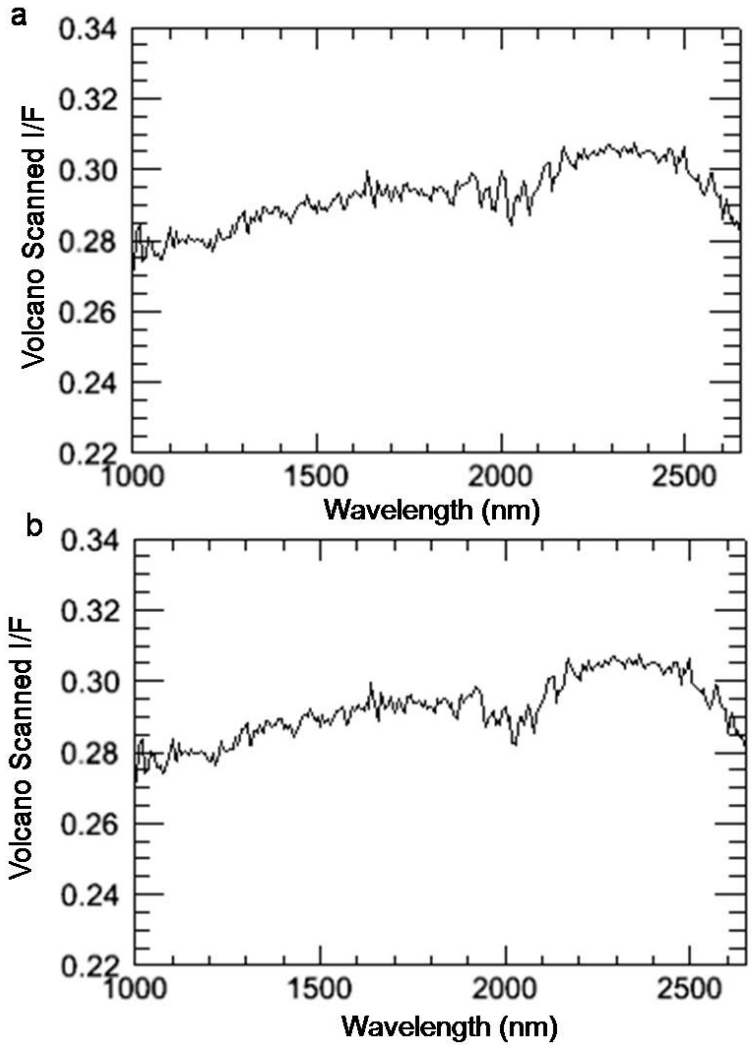

Figure 2.17. a) CRISM volcano scan correction using the transmission spectrum generated from FFC00008608 applied to a low altitude spectrum extracted from FFC00008608. A constant exponential scaling factor calculated using the BD1 estimate was used to scale the transmission spectrum. b) CRISM volcano scan correction using the transmission spectrum generated from FFC00008608 applied to a low altitude spectrum extracted from FFC00008608. A constant exponential scaling factor calculated using the BD2 estimate was used to scale the transmission spectrum.

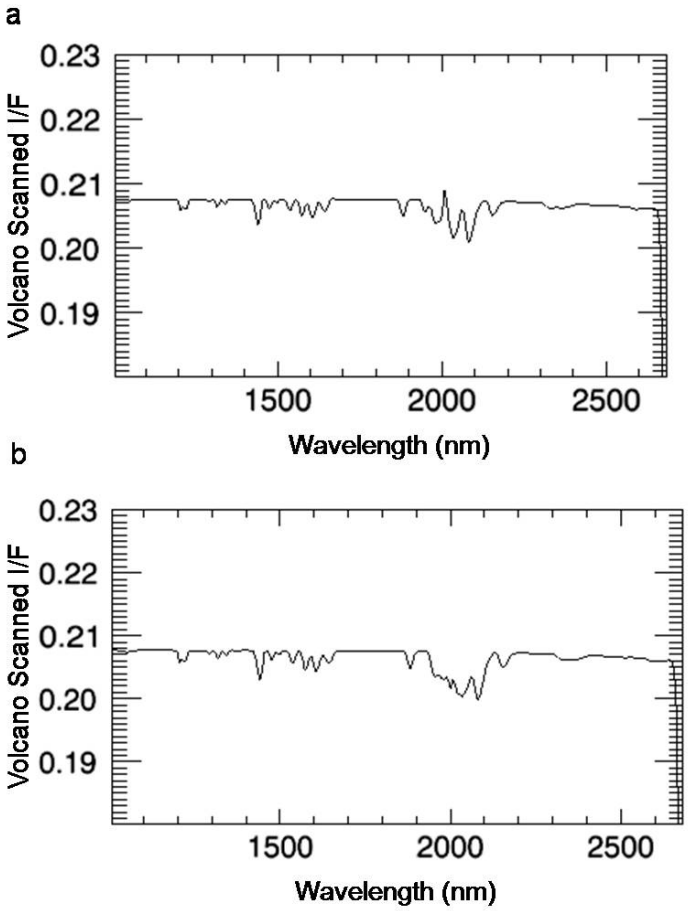

Figure 2.18. a) Simulated volcano scan correction utilizing a transmission spectrum derived from high and low altitude synthetic I/F spectra for which a total aerosol opacity of 0 was modeled and the surface spectra were identical. The simulated volcano scan correction was applied to the low altitude spectrum using a constant exponential scaling factor of 1.20. The scaling factor was calculated using the BD1 estimate. b) Simulated volcano scan correction utilizing a transmission spectrum derived from high and low altitude synthetic I/F spectra for which a total aerosol opacity of 0 was modeled and the surface spectra were identical. The simulated volcano scan correction was applied to the low altitude spectrum using a constant exponential scaling factor of 1.17. The scaling factor was calculated using the BD2 estimate.

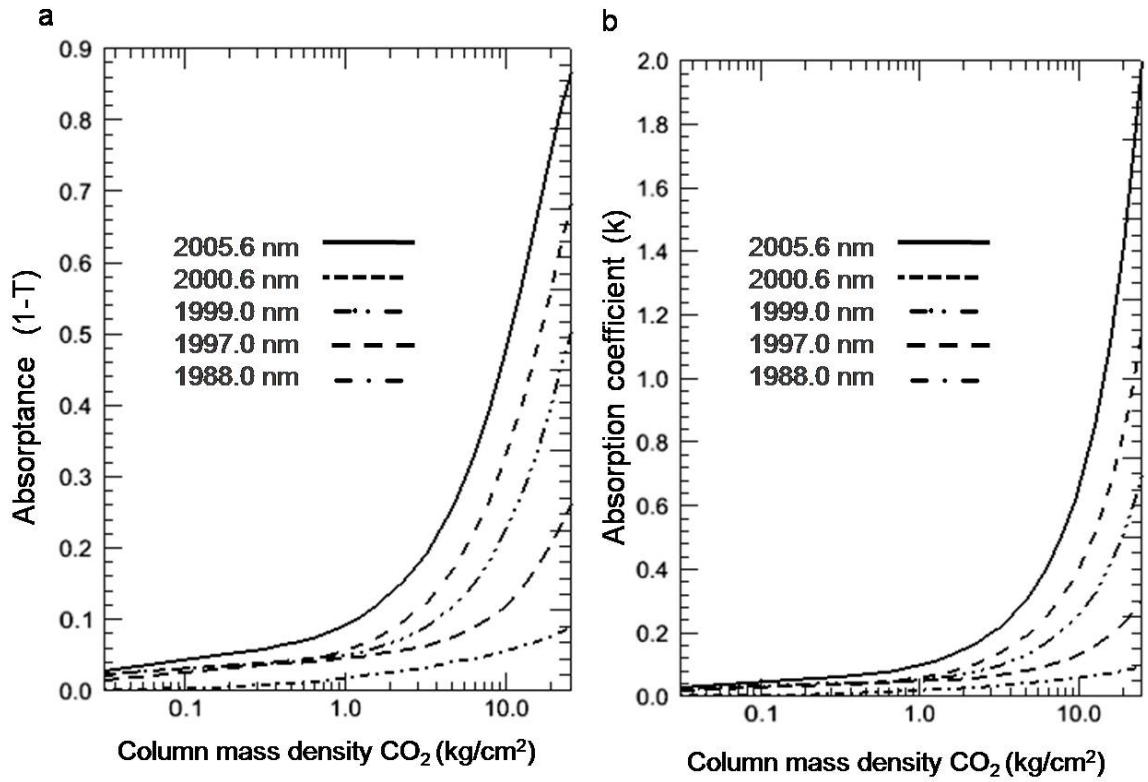

Figure 2.19. a) Absorptance versus column density for several different wavelengths generated using correlated-k inputs with 0.2 nm wavelength spacing and a width of 0.6 nm. b) Correlation coefficient versus column density for several different wavelengths generated using correlated-k inputs with 0.2 nm wavelength spacing and a width of 0.6 nm.

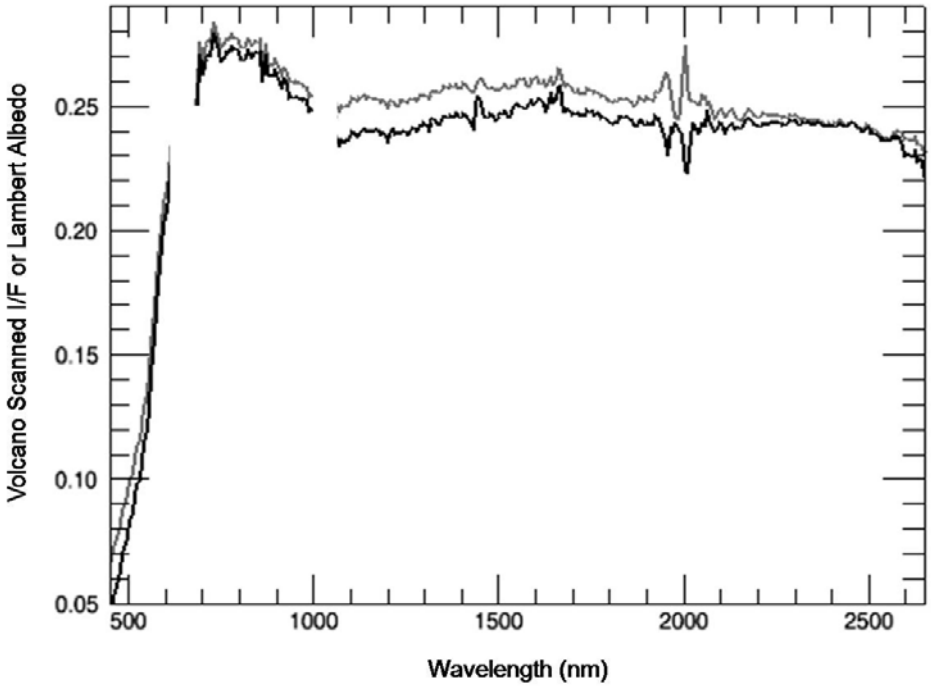

Figure 2.20. Black line: Lambert Albedo retrieval for a CRISM I/F spectrum extracted from FRT00003192 (10x10 spectral average, centered at column 300, line 220). A dust opacity of 0.38 at 900 nm was modeled based on MER Spirit Pancam optical depth measurements. Gray line: Volcano scan corrected spectrum for a CRISM I/F spectrum extracted from FRT00003192 (10x10 spectral average, centered at column 300, line 220) using the transmission spectrum derived from FFC00006C14.

REFERENCES

Clancy, R.T. et al. (2003), Mars aerosol studies with the MGS TES emission phase function observations: Optical depths, particle sizes, and ice cloud types versus latitude and solar longitude, *J. Geophys. Res*, Research 108(E9): 5089. doi:10.1029/2003JE002058.

Hapke, B. (1993), *Theory of reflectance and emittance spectroscopy.* Cambridge University Press: Cambridge, UK, pp 455.

Langevin, Y., F. Poulet, J.-P. Bibring, B. Gondet (2005), Sulfates in the northern polar region of Mars detected by OMEGA/Mars Express, *Science*, 307, 1584-1586.

Lemmon, M. T., et al. (2004), Atmospheric imaging results from the Mars Exploration Rovers: Spirit and opportunity, Science, 306, 1753–1756, doi: 10.1126/science.1104474.

McGuire, P. C. et al., (2009), An improvement to the volcano-scan algorithm for atmospheric correction of CRISM and OMEGA spectral data, *Adv. in Planet. Space Sci*., accepted.

Murchie, S., R. E. Arvidson, P. Bendini, K. Beisser, J.-P. Bibring, J. Bishop, J. Boldt, P. Cavender, T. Choo, R. T. Clancy, E. H. Darlington, D. Des Marais, R. Espiritu, D. Fort, R. Green, E. Guinness, J. Hayes, C. Hash, K. Heffernan, J. Hemmler, G. Heyler, D. Humm, J. Hutchenson, N. Izenberg, R. Lee, J. Lees, D. Lohr, E. Malaret, T. Martin, J. A. McGovern, P. McGuire, R. V. Morris, J. F. Mustard, S. Pelkey, E. Rhodes, M. Robinson, T. Roush, E. Schafer, G. Seagrave, F. P. Seelos, IV, S. Slavney, M. Smith, W.-J. Shyong, K. Stohbehn, H. Taylor, P. Thompson, B. Tossman, M. Wirzburger, and M. Wolff (2007), Compact Reconnaissance Imaging Spectrometer for Mars (CRISM) on Mars Reconnaissance Orbiter (MRO), *J. Geophys. Res*, *112*, E05S03, doi:10.1029/2006JE002682.

Parente, M. (2008), A new approach to denoisig CRISM images, *LPSC XXXVIII*, #2528.

Rothman, L.S. et al. (2009), The HITRAN 2008 molecular spectroscopic database, *J. of Quant. Spect. Rad. Transfer,* vol 110, 533-572.

Smith, M.D. (2004), Interannual Variability in TES Atmospheric Observations of Mars During 1999-2003. Icarus, 167, 148-165.

Smith, M. D. (2008), Spacecraft Observations of the Martian Atmosphere, Annual Review of Earth and Planetary Sciences, 36, 191–219, doi:10.1146/annurev.earth.36.031207.124334.

Smith, M. D., M. J. Wolff, R. T. Clancy, and S. L. Murchie (2009), CRISM observations of water vapor and carbon monoxide,*J. Geophys. Res*, in press.

Stamnes, K., S. Tsay, W. Wiscombe, and K. Jayaweera (1988), Numerically stable algorithm for discrete-ordinate-method radiative transfer in multiple scattering and emitting layered media, *Appl. Opt.*, *27*, 2502-2509.

Stamnes, K., S.-C. Tsay, I. Laszlo (1999), DISORT , a general purpose Fortran program for discrete-ordinate-method radiative transfer in scattering and emitting layered media: Documentation and methodology, pp 112.

Tillman, J. E., N. C. Johnson, P. Guttorp, and D. B. Percival (1993), The Martian annual atmospheric pressure cycle – Years without great dust storms. J. Geophys. Res., 98, 10963–10971.

Thomas, G. E., Stamnes, K. (2002), *Radiative transfer in the atmosphere and ocean*, Cambridge University Press, New York, 546pp.

Wolff, M. J., R. T. Clancy, M. D. Smith, CRISM Science Team, and Marci Science Team (2007), Some studies of Martian aerosol properties using MRO/CRISM and MRO/Marci, *Sev. Intl. Conf. Mars*, 3121.

Wolff, M. J., M. D. Smith, R. T. Clancy, R. E. Arvidson, M. Kahre, F. P. Seelos IV, S. Murchie, H. Savij¨arvi, and the CRISM Science Team (2009), Wavelength Dependence of Dust Aerosol Single Scattering Albedo As Observed by CRISM, *J. Geophys. Res*, submitted.

CHAPTER 3 – PHYLLOSILICATE AND SULFATE-HEMATITE DEPOSITS WITHIN MIYAMOTO CRATER IN SOUTHERN SINUS MERIDINAI, MARS

3.1 Introduction

Miyamoto crater is a 160 km in diameter Noachian-aged crater that is located in southern Sinus Meridiani (Figure 3.1). The northeastern portion of the crater is buried by a plains forming unit (Figures 3.1 and 3.2), which is composed of layered sedimentary rock covered with a thin sand sheet. The extent of the plains unit corresponds with occurrences of crystalline gray hematite detected by the Thermal Emission Spectrometer (TES) [*Christensen et al*., 2000]. Previous analyses using Mars Express Observatoire pour la Minéralogie, l'Eau, les Glaces et l'Activité (OMEGA) [*Bibring et al.,* 2004] spectral reflectance data have shown that the surface of the plains unit is dominated spectrally by basaltic sand, gray hematite, and nanophase iron oxides in the visible/near infrared (VIS/NIR) between 0.4 to 2.6 μm [*Arvidson et al.,* 2006]. Analyses of higher resolution Mars Reconnaissance Orbiter (MRO) Compact Reconnaissance Imaging Spectrometer for Mars (CRISM) [*Murchie et al.,* 2007] images confirmed that outcrop exposed near the Mars Exploration Rover (MER) Opportunity landing site is spectrally dominated by nanophase ferric oxides in the VIS/NIR [*Wiseman et al.,* 2007a]. In situ observations made by the Opportunity rover [*Squyres et al.,* 2004] demonstrate that the outcrops are "dirty" sulfate-rich evaporites that formed in a low pH playa environment [*e.g., Grotzinger et al.,* 2005*; Morris et al.,* 2006]. Based on these analyses, we will refer to the plains unit as the sulfate- and hematite-bearing plains.

Using NIR (1.0 to 2.6 μm) spectral reflectance data from the CRISM and the OMEGA spectrometers and other orbital observations, we identify partially exhumed phyllosilicate-bearing deposits in the western portion of the Miyamoto crater floor (Figures 3.2) that predate the formation of the younger sulfate- and hematite-bearing plains unit. This work builds on detections of phyllosilicate minerals in other areas of Sinus Meridiani using OMEGA data [*Poulet et al.,* 2005*,* 2008] and provides a detailed geologic and stratigraphic context for the phyllosilicate identifications.

3.2 Geologic Context

Miyamoto crater is mapped within the Meridiani dissected cratered terrain (DCT) [*e.g., Hynek et al.,* 2002*; Arvidson et al.,* 2003]. The DCT is dissected by channel features that formed via fluvial erosion during the late Noachian period [*Hynek and Phillips,* 2001] and many craters within this unit have been partially buried and exhumed [*Edgett,* 2005]. Sulfate- and hematite-bearing plains deposits unconformably overlie the DCT and record a change in environmental conditions from a high energy erosive system to accumulation of evaporitic sediments in an arid environment [*Arvidson et al.,* 2006].

At less than 1 km deep (Figure 3.2b), Miyamoto crater is shallow relative to a similarly sized pristine impact crater, which should have a depth of ~3 km [*Howenstine and Kiefer,* 2005]. The steep slope of the interior wall and flat floor of Miyamoto crater suggest that fluvial erosion and deposition were a factor in crater degradation [*Craddock and Howard,* 2002]. Fluvial features that postdate crater formation occur in the vicinity of Miyamoto crater (Figure 3.1), and *Newsom et al.* [2003] hypothesize that Miyamoto was the site of a large drainage basin.

3.3 Spectral Reflectance Retrievals, Analysis, and Mapping

Our analyses of CRISM and OMEGA NIR spectral data focus on the identification of alteration minerals within Miyamoto crater using diagnostic H_2O and/or OH vibrational features that occur between 1.0 and 2.5 μm. Atmospheric gas bands were removed from I/F (radiance at sensor divided by the solar irradiance at the top of the Martian atmosphere divided by π) spectra by ratioing to a scaled atmospheric transmission spectrum derived from Olympus Mons observations [*Mustard et al.,* 2005]. Lambert albedo spectra were retrieved with DISORT [*Stamnes et al.,* 1988*; Wolff et al.,* 2007] atmospheric modeling to remove gas and aerosol contributions for selected spectra, using procedures outlined in *Arvidson* et al. [2006]. Analyses included detailed comparisons of CRISM and OMEGA spectra with laboratory spectra and band depth mapping to detect the presence of H_2O and OH vibrational modes.

Deposits within the western portion of the Miyamoto crater floor exhibit pronounced spectral absorption features near 1.9 and 2.3 μm and weaker features at 1.4 and 2.4 μm in CRISM and OMEGA spectra (Figure 3.3). Comparison of these spectral features to spectra of mineral samples with known compositions suggests that phyllosilicates contribute to the observed CRISM and OMEGA spectra. Saponite, a Mg-rich trioctahedral smectite, has distinct absorption features near 1.4 (O - H stretch overtone), 1.9 (combination of the H - O - H bend and O - H stretch), 2.31 (Mg - OH vibration), and a weak feature at 2.39 μm [*Clark et al.,* 1990]. Nontronite, an Fe^{3+} dioctahedral smectite, has features near 1.4, 1.9, 2.28 (Fe^{3+} - OH vibration), and 2.4 μm [*Frost et al*., 2002]. Increased proportions of Mg to Fe in smectite clays shift the ~2.3 μm band to slightly longer wavelengths [*Bishop et al.,* 2002*; Swayze et al.,* 2002].

The phyllosilicate-bearing deposits within Miyamoto crater were mapped based on the presence of the 2.3 μm spectral absorption feature using the D2.30 parameter index, where D2.30 = 1 – [(CR2.29 + CR2.32 + CR2.33) / (CR2.12 + CR2.17 + CR2.21)] and CR represents reflectance values at the specified wavelength divided by continuum values between 1.80 and 2.53 μm. This D2.30 parameter is the same parameter defined in Pelkey et al. [2007], with the exception that the 2.12 μm band is used instead of the 2.14 μm band. Because CRISM and OMEGA instruments sample different wavelength positions, the bands with wavelengths centers closest to those defined in the D2.30 parameter were utilized. D2.30 parameter values of ≥ 1.0 and 1.5% were used to indicate a positive detection of the 2.3 μm feature in CRISM and OMEGA spectra, respectively (Figure 3.2a).

The exact band center of the 2.3 μm feature in the western Miyamoto crater floor deposits varies between 2.29 and 2.31 μm, and the width of the feature is also somewhat variable. The CRISM and OMEGA spectra from the western Miyamoto crater floor deposits are consistent with the presence of Fe/Mg-rich smectite phyllosilicates (Figure 3.3b).

3.4 Miyamoto Crater Interior Materials

We examined the geomorphology and stratigraphy of Miyamoto crater interior materials using images from the MRO High Resolution Imaging Science Experiment (HiRISE) [*McEwen et al.,* 2007], the MRO Context Imager (CTX) [*Malin et al.,* 2007], the Mars Express High Resolution Stereo Camera (HRSC) [*Neukum et al.,* 2004], the Mars Orbiter Camera (MOC) [*Malin et al.,* 1992] and the Mars Odyssey Thermal

Emission Imaging System (THEMIS) [*Christensen et al.,* 2004] and topographic data from the Mars Orbiter Laser Altimeter (MOLA) [*Smith et al.,* 2001]. The sulfate- and hematite-bearing plains unit (Figures 3.1 and 3.2) buries the northeastern rim of Miyamoto crater and covers pre-existing crater floor materials. MOLA profiles through Miyamoto crater are consistent with the interpretation that the plains unit once extended further into the crater and was eroded back to produce the present topography within Miyamoto crater (Figure 3.2b). Portions of the crater floor are partly covered by ejecta from craters visible just outside of the crater rim (Figure 3.2a), and variable amounts of aeolian cover obscure some of the crater floor materials.

Polygonally fractured bedrock (Figure 3.4) that has been exhumed from beneath overlying crater floor capping material is exposed in the western portion of the Miyamoto crater floor. The CRISM and OMEGA phyllosilicate detections (Figures 3.2a and 3.3) correlate with exposures of polygonally fractured bedrock. The crater floor capping material appears to be a relatively thin unit (on the order of 10s of meters) that preserves small impact craters and is conformal with pre-existing crater floor topography. The morphology of the crater floor cap unit is similar to intercrater plains material found throughout the DCT. Morphologic features, including sinuous ridges and mesas, have been identified in the northwestern portion of the crater floor (Figure 3.2a) that have been interpreted as inverted channel deposits [*Edgett,* 2005*; Newsom et al.,* 2007].

3.5 Discussion and Implications

The exhumed phyllosilicate-bearing deposits exposed within the Miyamoto crater floor are interpreted to predate the formation of the sulfate- and hematite-bearing plains unit that covers the northeastern portion of the crater. These Fe/Mg-rich smectite phyllosilicates may have formed authigentically in a lacustrine or subsurface environment or may be remnants of fluvially transported material. High-resolution hydrological models that include rainfall, ground water infiltration, and ground water emergence predict that Miyamoto crater was the site of continued ground water emergence associated with the unique topography of the western Arabia Terra region (Figure 3.1) [*Andrews-Hanna et al.,* 2007*,* 2008]. Thus, Miyamoto crater likely experienced aqueous environmental conditions conducive to formation of phyllosilicate minerals and was later subjected to a steady flux of groundwater ultimately leading to deposition of evaporite deposits. As noted by *Bibring et al*. [2006], the age relationships between the phyllosilicates and sulfate-rich deposits are consistent with a change from an open hydrologic system with neutral pH conditions to a more arid acid-sulfate dominated ground water system.

The deposits within Miyamoto crater provide an important site for exploration by the 2009 NASA Mars Science Laboratory (MSL) rover and any future rover-based missions that are equipped to assess the past habitability on Mars. In particular, the site allows exploration of older phyllosilicate-bearing deposits and younger sulfate- and hematite-bearing plains materials that record a significant environmental and climatic transition that occurred during the Late Noachian / Early Hesperian period on Mars. And

finally, smectites have the potential to preserve biomarkers via absorption of organic material onto interlayer sites [e.g., *Butterfield,* 1990].

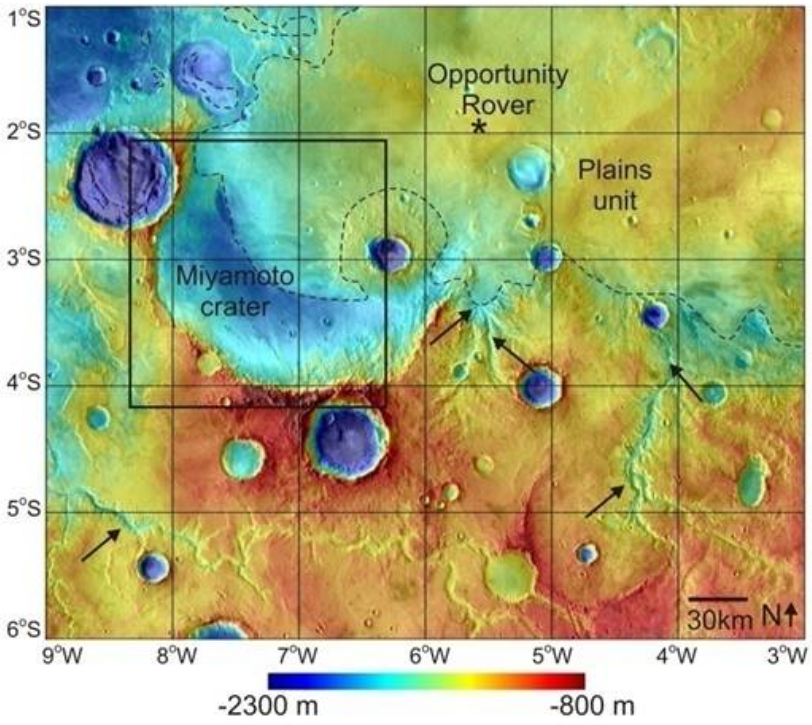

Figure 3.1. MOLA elevation map overlain on THEMIS daytime infrared mosaic. The southern extent of the sulfate- and hematite-bearing plains unit analyzed by the Opportunity rover is indicated with the dashed line on this context image. Fluvial features are indicated with arrows.

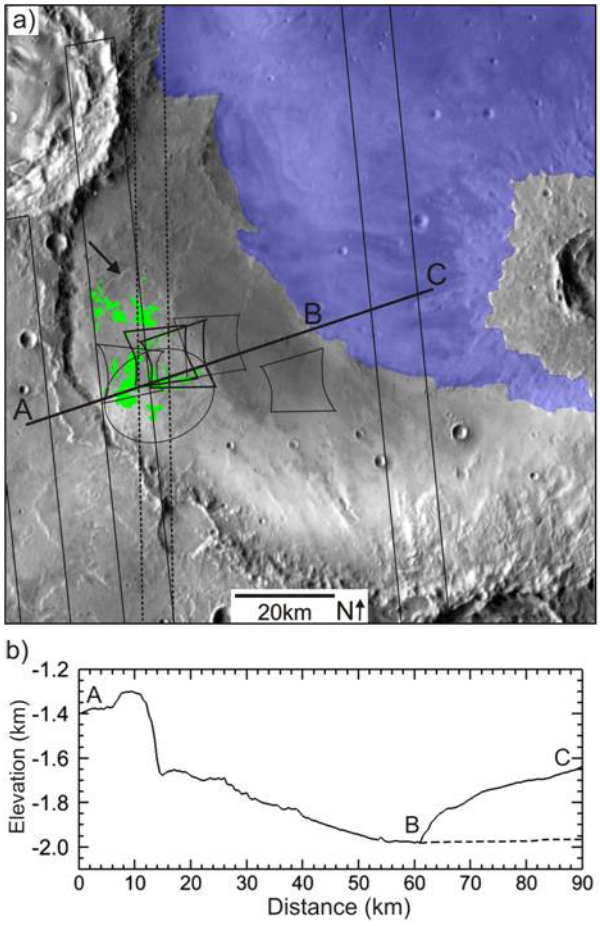
a)
A
B
C
20km
N
b)
Elevation (km)
-1.2
-1.4
-1.6
-1.8
-2.0
0
10
20
30
40
50
60
70
80
90
Distance (km)

Figure 3.2. (a) THEMIS daytime infrared mosaic (230 m/pixel) covering Miyamoto crater with CRISM and OMEGA D2.30 parameter values ≥ 1.0 and 1.5%, respectively, shown in green. The extent of the sulfate- and hematite-bearing plains unit is mapped in blue. The location of inferred inverted channel deposits in the northwestern portion of the crater is indicated with an arrow. D2.30 parameter values have been calculated for the entire area shown in the THEMIS mosaic using OMEGA images that range in spatial resolution from 650 to 1650 m/pixel. For areas covered at multiple resolutions with overlapping CRISM and OMEGA images, the D2.30 parameter values from the highest spatial resolution images are shown. Image footprints for the highest spatial resolution images are outlined in black. OMEGA image ORB2097_5 (340 m/pixel) is indicated with a dashed outline. CRISM multispectral mapping strips (200 m/pixel) are shown with solid outlines (from left to right: MSP00005C19_05, MSP00004886_07, MSP00005100_03) and CRISM full resolution (20 m/pixel) bowtie-shaped footprints are also outlined in solid black (from left to right: FRT00007B8B, FRT00009C02, FRT000097C9, FRT00009379, and FRT000081E0). The candidate Mars Science Laboratory (MSL) Miyamoto landing ellipse from the second MSL landing site workshop [*Wiseman et al.,* 2007b] is also shown. (b) MOLA elevation profile along the line from A to C shown in Figure 3.2a.

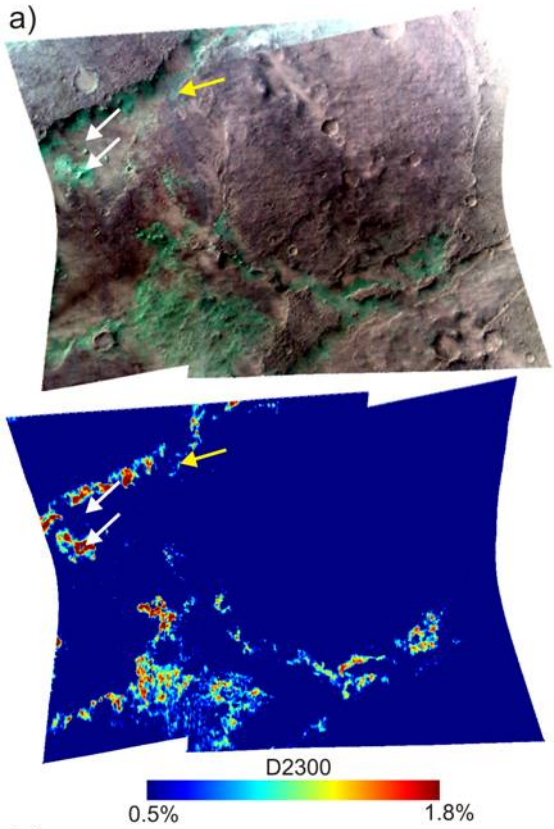
a)
D2300
0.5%
1.8%

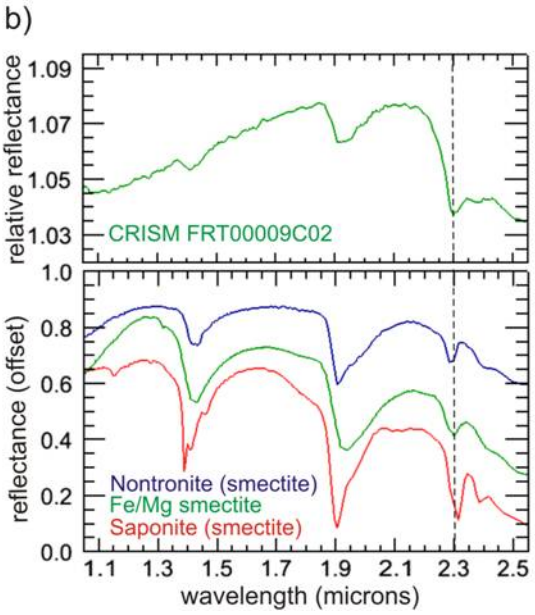
b)
relative reflectance
1.09
1.07
1.05
1.03
CRISM FRT00009C02
reflectance (offset)
1.0
0.8
0.6
0.4
0.2
0.0
Nontronite (smectite)
Fe/Mg smectite
Saponite (smectite)
1.1
1.3
1.5
1.7
1.9
2.1
2.3
2.5
wavelength (microns)

Figure 3.3. (a) *Upper:* CRISM false color composite of FRT00009C02 and FRT0000979C (locations shown in Figure 3.2a with bold outlines) with red = 2.5 μm – D2.30 value, green = 1.8 μm, and blue = 1.1 μm. *Lower*: D2.30 band depth map for CRISM images FRT00009C02 and FRT0000979C. (b) *Upper:* CRISM spectral ratio of an average of 150 Lambert albedo spectra extracted from the area indicated with the lower white arrow in Figure 3.3a to the average of 150 spectra extracted from a spectrally bland region indicated with the upper white arrow. *Lower*: Laboratory spectra of terrestrial samples that are similar in shape to the CRISM spectrum. The Fe/Mg smectite spectrum is a laboratory measurement from the CRISM spectral library [*CRISM Science Team*, 2006] and the nontronite and saponite spectra are from the USGS spectral library [*Clark et al*., 2007]. The yellow arrow indicates the location of the HiRISE image subset shown in Figure 3.4.

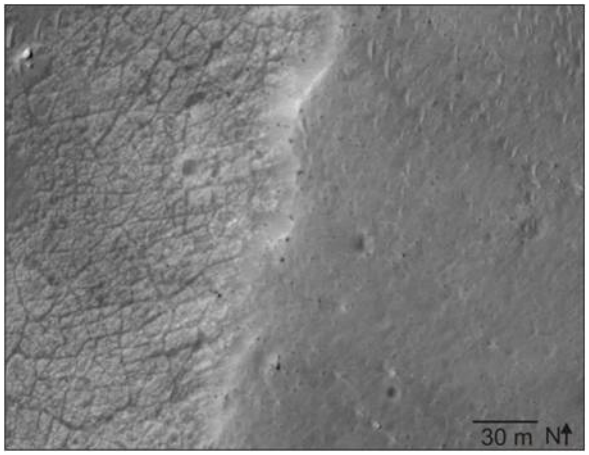

Figure 3.4. Subset of HiRISE image PSP 007124_1765_RED covering the area indicated with the yellow arrow in Figure 3.3a. Polygonally fractured phyllosilicate-bearing deposits appear on the left of the image and overlying capping material covers the right portion of the image. The phyllosilicate-bearing deposits were exhumed from beneath the capping material.

REFERENCES

Andrews-Hanna, J. C., R. J. Phillips, and M. T. Zuber (2007), Meridiani Planum and the global hydrology of Mars, *Nature*, *446*, 163-166.

Andrews-Hanna, J. C., M. T. Zuber, and R. J. Phillips (2008), Early Mars hydrology: Valley networks and evaporite deposits, *Lunar Planet. Sci.*, *XXXIX*, 1993.

Arvidson, R. E., et al. (2003), Mantled and exhumed terrains in Terra Meridiani, Mars, *J. Geophys. Res.*, *108*(E12), 8073, doi:10.1029/2002JE001982.

Arvidson, R. E., et al. (2006), Nature and Origin of the Hematite-Bearing Plains of Terra Meridiani Based on Analysis of Orbital and Mars Exploration Rover Data Sets, *J. Geophys. Res.*, *111*, E12S09, doi:10.1029/2006JE002728.

Bibring, J.-P., et al. (2004), OMEGA: Observatoire pour la Minéralogie, l'Eau, les Glaces et l'Activite´, in *Mars Express: The Scientific Payload*, edited by A. Wilson, pp. 37-49, ESA Spec. Publ., Noordwijk.

Bibring, J.-P., et al. (2006), Global mineralogical and aqueous Mars history derived from OMEGA/Mars Express Data, *Science*, *312*, 400-404.

Bishop, J. L., E. Murad, and M. D. Dyar (2002), The influence of octahedral and tetrahedral cation substitution on the structure of smectites and serpentines as observed through infrared spectroscopy, *Clay Minerals*, *37*, 617-628, doi: 10.1180/0009855023740064.

Butterfield, N. J. (1990), Organic preservation of non-mineralizing organisms and the taphonomy of the Burgess Shale, *Paleobiology*, *16*(3), 272-286.

Christensen, P. R., et al. (2000), Detection of crystalline hematite mineralization on Mars by the Thermal Emission Spectrometer: Evidence for near-surface water, *J. Geophys. Res*, *105*(E4), 9623-9642.

Christensen, P. R., et al. (2004), The Thermal Emission Imaging System (THEMIS) for the Mars 2001 Odyssey mission, *Space Sci. Rev.*, *110*, 85-130, doi:10.1023/B:SPAC.0000021008.16305.94.

Clark, R. N., T. V. V. King, M. Klejwa, and G. A. Swayze (1990), High resolution reflectance spectroscopy of minerals, *J. Geophys. Res*, *95*(B8), 12653-12680.

Clark, R. N., G. A. Swayze, R. Wise, K. E. Livo, T. M. Hoefen, R. F. Kokaly, and S. J. Sutley (2007), USGS digital spectral library, *U.S. Geological Survey, Data Series 231*.

Craddock, R. A., and A. D. Howard (2002), The case for rainfall on a warm, wet early Mars, *J. Geophys. Res*, *107*(E11), 5111, doi:10.1029/2001JE001505.

CRISM Science Team (2006), Mars Reconnaissance Orbiter CRISM Spectral Library, *NASA Planetary Data System*, MRO-M-CRISM-5-SPECLIB-V1.0.

Edgett, K. S. (2005), The sedimenatary rocks of Sinus Meridiani: Five key observations from data acquired by the Mars Global Surveyor and Mars Odyssey Orbiters, *Mars*, doi:10.1555/mars.2005.0002.

Frost, R. L., J. T. Kloprogee, and Z. Ding (2002), Near-infrared spectroscopic study of nontronites and ferruginous smectite, *Geochim. Cosmochim. Acta*, *58*, 1657-1668.

Grotzinger, J. P., et al. (2005), Stratigraphy and sedimentology of a dry to wet eolian depositional system, Burns formation, Meridiani Planum, Mars, *Earth Planet. Sci. Lett.*, *240*, 11-72.

Howenstine, J. B., and W. S. Kiefer (2005), Morphometry of large Martian impact craters, *Lunar and Planet. Sci.*, *XXXVI*, 1742.
Hynek, B. M., R. E. Arvidson, and R. J. Phillips (2002), Geologic setting and origin of Terra Meridiani hematite deposit on Mars, *J. Geophys. Res*, *107*(E10), 5088, doi:10.1029/2002JE001891, 2002.
Hynek, B. M., and R. J. Phillips (2001), Evidence for extensive denudation of the Martian highlands, *Geology*, *29*(5), 407-410, doi:10.1130/0091-7613(2001)029.
Malin, M. C., et al. (1992), Mars Observer Camera, *J. Geophys. Res*, *97*, 7699-7718.
Malin, M. C., et al. (2007), Context Camera Investigation on board the Mars Reconnaissance Orbiter, *J. Geophys. Res*, *112*, E05S04, doi:10.1029/2006JE002808.
McEwen, A. S., et al. (2007), Mars Reconnaissance Orbiter's High Resolution Imaging Science Experiment (HiRISE), *J. Geophys. Res*, *112*, E05S02, doi:10.1029/2005JE002605.
Morris, R. V., et al. (2006), Mössbauer mineralogy of rock, soil, and dust at Meridiani Planum, Mars: Opportunity's journey across sulfate-rich outcrops, basaltic sand and dust, and hematite lag deposits, *J. Geophys. Res*, *111*, E12S15, doi:10.1029/2006JE002791.
Murchie, S., et al. (2007), Compact Reconnaissance Imaging Spectrometer for Mars (CRISM) on Mars Reconnaissance Orbiter (MRO), *J. Geophys. Res*, *112*, E05S03, doi:10.1029/2006JE002682.
Mustard, J. F., et al. (2005), Olivine and pyroxene diversity in the crust of Mars, *Science*, *307*, 1594-1597.
Neukum, G., R. Jaumann, and the HRSC Co-Investigator and Experiment Team (2004), HRSC: The High Resolution Stereo Camera of Mars Express, in *Mars Express: The Scientific Payload*, edited by A. Wilson, pp. 17-35, Eur. Space Agency Spec. Publ., Noordwijk.
Newsom, H. E., C. A. Barber, T. M. Hare, T. Schelble, V. A. Sutherland, and W. C. Feldman (2003), Paleolakes and impact basins in southern Arabia Terra, including Meridiani Planum: Implications for the formation of hematite deposits on Mars, *J. Geophys. Res*, *108*(E12), 8075, doi:10.1029/2002JE001993.
Newsom, H. E., et al. (2007), Southwest Meridiani Planum (Runcorn Crater) Part 2 - Northern area, phyllosilicates, sediments, and evaporites in the ancient crust of Mars, *Sec. MSL Workshop*.
Pelkey, S. M., et al. (2007), CRISM multispectral summary products: Parameterizing mineral diversity on Mars from reflectance, *J. Geophys. Res*, *112*, E08S14, doi:10.1029/2006JE002831.
Poulet, F., et al. (2005), Phyllosilicates on Mars and implications for early Martian climage change, *Nature*, *438*, 632-627.
Poulet, F., et al. (2008), Mineralogy of Terra Meridiani and western Arabia Terra from OMEGA/MEx and implications for their formation, *Icarus*, *195*(1), 106-130, 10.1016/j.icarus.2007.11.031.
Smith, D. E., et al. (2001), Mars Orbiter Laser Altimeter: Experiment summary after the first year of global mapping of Mars, *J. Geophys. Res*, *106*(E10), 23689-23722.

Squyres, S. W., et al. (2004), The Opportunity Rover's Athena Science Investigation at Meridiani Planum, Mars, *Science*, *306*, 1698-1703.

Stamnes, K., S. Tsay, W. Wiscombe, and K. Jayaweera (1988), Numerically stable algorithm for discrete-ordinate-method radiative transfer in multiple scattering and emitting layered media, *Appl. Opt.*, *27*, 2502-2509.

Swayze, G. A., et al. (2002), Mineral mapping Mauna Kea and Mauna Loa shield volcanos on Hawaii using AVIRIS data and the USGS Tetracorder spectral identification system: Lessons applicable to the search for relict Martian hydrothermal systems, in *Proceedings of the 11th JPL Airborne Earth Science Workshop*, edited by R. O. Green, pp. 373-387.

Wiseman, S. M., et al. (2007a), New analyses of MRO CRISM, HiIRSE, and CTX data over layered sedimentary deposits in Meridiani, *Sev. Intl. Conf. Mars*, 3111.

Wiseman, S. M., et al. (2007b), Juxtaposition of phyllosilicates and sulfates, central Runcorn crater (southern Meridiani candidate MSL landing site), *Sec. MSL Workshop*.

Wolff, M. J., R. T. Clancy, M. D. Smith, the CRISM Science Team, and the Marci Science Team (2007), Some studies of Martian aerosol properties using MRO/CRISM and MRO/Marci, *Sev. Intl. Conf. Mars*, 3121.

CHAPTER 4 – SPECTRAL AND STRATIGRAPHIC MAPPING OF HYDRATED SULFATE AND PHYLLOSILICATE-BEARING DEPOSITS IN NORTHERN SINUS MERIDIANI, MARS

4.1 Introduction

Geomorphic and/or spectral evidence for past aqueous activity is preserved in multiple units that occur within Sinus Meridiani, Mars. Fluvially dissected Noachian-aged cratered terrain is unconformably overlain by extensive outcrops of hydrous light-toned sedimentary rock [*Malin* and *Edgett*, 2000; *Edgett* and *Malin*, 2002; *Hynek et al*., 2002; *Arvidson et al*., 2003; *Gendrin et al*., 2005; *Poulet et al*., 2008]. The Meridiani Planum sulfate and hematite-bearing unit investigated by the Mars Exploration Rover (MER) Opportunity [*Squyres et al*., 2004] occurs near the top of the stratigraphic section exposed in Sinus Meridiani [*Christensen et al*., 2001; *Hynek et al*., 2002; *Arvidson et al*., 2003; *Christensen* and *Ruff*, 2004].

In this paper we present detailed stratigraphic and spectral analyses that focus on a region in northern Sinus Meridiani located between 1º N to 5º N latitude and 3º W to 1º E longitude. The presence of outcrops with well exposed contacts and distinctive spectral signatures facilitates stratigraphic analyses in this region. Several stratigraphically distinct units were defined and mapped within the study area based on morphologic expression and superposition relationships. Previously identified layered deposits with monohydrated and polyhydrated sulfate spectral signatures [*Arvidson et al*., 2005; *Gendrin* et al.; 2005, *Griffes* et al., 2007] are reexamined using higher resolution Mars Reconnaissance Orbiter (MRO) Compact Reconnaissance Imaging Spectrometer for

Mars (CRISM) [*Murchie et al.,* 2007], Context Imager (CTX) [*Malin et al.,* 2007], and High Resolution Imaging Science Experiment (HiRISE) [*McEwen et al.,* 2007] data. Additional hydrated sulfate and Fe/Mg phyllosilicate-bearing exposures are identified using MRO CRISM and Mars Express (MEX) Observatoire pour la Minéralogie, l'Eau, les Glaces et l'Activité (OMEGA) [*Bibring et al.,* 2004] near-infrared (NIR) (1.0 to 2.5 μm) spectral reflectance observations.

4.2 Geologic Context

The Sinus Meridiani region of Mars, formerly termed Terra Meridiani, is located near the southwestern margin of Arabia Terra and is centered at 5° S, 0° E. Heavily cratered Noachian-aged terrain that has an ancient regional slope to the northwest [*Phillips et al*., 2001; *Andrews-Hanna et al*., 2009] is exposed at the base of the stratigraphic section in Sinus Meridiani. The Noachian cratered terrain was fluvially dissected and unconformably overlain by light toned indurated sedimentary rock referred to as 'etched' terrain [*Hynek et al*., 2002; *Arvidson et al*., 2003]. Low albedo, hematite-bearing plains dominate the surface of central Sinus Meridiani, Meridiani Planum [*Christensen et al*., 2001; *Hynek et al*., 2002; *Arvidson et al*., 2003].

To facilitate discussion of our study area (1º N to 5º N latitude and 3º W to 1º E longitude), we present an updated regional context map of Sinus Meridiani that is broadly similar to previous maps (Figure 4.1) [e.g., *Hynek et al.,* 2002; *Arvidson et al.*, 2003; *Hynek*, 2004]. Materials are subdivided into *Cratered Terrain* (CT), *Etched Terrain 1* (ET1), and the *Plains, Hematite-bearing* (Ph). ET1 is equivalent to the etched terrain unit mapped by *Hynek et al.* [2002], *Arvidson et al.* [2003], and *Hynek*, [2004].

Ph consists of rock overlain by an unconsolidated veneer [e.g., *Arvidson et al*., 2006]. In this paper, we classified the rock component of Ph as *Etched Terrain 2* (ET2) and the unconsolidated veneer as *Plains Mantle, Hematite-bearing* (Pm). Unit boundaries were mapped using a combination of attributes including morphology, topographic expression, relative thermal properties, selected spectral characteristics, and superposition relationships. Units are described in sections 4.2.1 through 4.2.3 and a brief overview of postulated formation mechanisms for ET1 and ET2 is presented in section 4.2.4.

4.2.1 Cratered Terrain (CT)

Although Noachian-aged *Cratered Terrain* (CT) was subdivided into multiple units in previous work [e.g., *Scott and Tanaka*, 1986; *Hynek et al.,* 2002], this level of distinction is not made in our regional context map (Figure 4.1). Some of the Noachian-aged craters in CT have prominent yet degraded rims [*Hynek et al*., 2002] whereas others are almost completely buried or exhibit a flat floored morphology that may have resulted from fluvial erosion and deposition [*Craddock* and *Howard*, 2002]. CT in southern Sinus Meridiani is heavily dissected by channels that are orientated in the direction of regional slope, to the northwest (Figure 4.1a) [*Scott* and *Tanaka*, 1986; *Hynek et al*., 2002]. A relatively intense episode of fluvial erosion occurred during the late Noachian period that reactivated preexisting channels and carved additional fluvial features in southern Sinus Meridiani [*Hynek and Phillips*, 2001; *Hynek and Phillips*, 2008].

Areas mapped as CT that appear bright in Figure 4.1b are mantled by aeolian dust deposits [*Arvidson et al*., 2003]. CT surfaces that are not mantled by dust generally have

low albedos [*Arvidson et al*., 2003], intermediate thermal inertias [*Arvidson et al*., 2003; *Hynek et al*., 2004], and have a basaltic spectral signature [*Poulet et al*., 2008]. Higher thermal inertia materials are exposed in some intracrater deposits and on limited intercrater surfaces. In addition, Fe/Mg phyllosilicate-bearing materials were previously identified in limited locations within CT (Figure 4.1, green arrows) [*Poulet et al*., 2008; *Wiseman et al*., 2008].

4.2.2 Etched Terrain 1 (ET1)

The *Etched Terrain 1* (ET1) unit unconformably overlies CT and is composed of relatively high thermal inertia indurated material [*Mellon et al.,* 2000; *Malin and Edgett*, 2000; *Edgett and Malin*, 2002; *Arvidson et al*., 2003; *Hynek et al*., 2004] that is 300 m thick in some areas. ET1 is laterally extensive across Sinus Meridiani and is characterized by intermediate albedos and relatively high thermal inertias [*Arvidson et al*., 2003; *Hynek et al.,* 2004]. Surfaces of ET1 are subhorizontal and typically dip between 0.01° to 1.0° in the direction of regional slope, to the northwest [*Hynek and Phillips*, 2008]. ET1 exhibits layering at multiple scales [*Malin and Edgett*, 2000; *Edgett,* 2005] and the presence of erosional mesas and grooves indicates variable material properties among layers [*Arvidson et al*., 2003; *Edgett ,* 2005]. ET1 consists of several morphologically distinct subunits that are not distinguished in this regional context map, but are detailed in section 4.4.

ET1 is inferred to have formed during the Late Noachian to Early Hepserian period [*Hynek et al*, 2002]. Along its southern margin, ET1 embays several channel

features that were incised into CT. However, there is some evidence that channel features that formed during the Late Noachian also cut lower layers of ET1 [*Hynek and Phillips*, 2008].

Although the western margin of ET1 is mantled with bright dust (Figure 4.1b), this area is mapped as ET1 because it is laterally continuous with and morphologically similar to unmantled areas. The central and eastern portions of ET1 are well exposed and have higher thermal inertias than other portions of the unit (Figure 4.1c) [e.g., *Hynek,* 2004]. Hydrous materials were detected in OMEGA spectral reflectance observations more frequently in areas of ET1 with the highest thermal inertias (Figure 4.1d) [*Poulet et al*., 2008]. Previously identified areas of ET1 that exhibit distinctive hydrated sulfate and Fe/Mg phyllosilicate spectral signatures are indicated in Figure 4.1 (red and green arrows, respectively) [*Gendrin et al*., 2005; *Griffes et al*., 2007; *Poulet et al*., 2008].

4.2.3 Plains, Hematite-bearing (Ph)

The *Plains, Hematite-bearing* (Ph) unit is a composite unit that consists of rock, *Etched Terrain 2* (ET2), overlain by an unconsolidated veneer, the *Plans Mantle, Hematite-bearing* (Pm). ET2 occurs stratigraphically above ET1 [*Hynek et al*., 2002; *Arvidson et al*., 2003]. In situ investigations of Ph made by the MER Opportunity rover (landing site indicated in Figure 4.1) revealed that the bedrock component of Ph, ET2, is composed of ~20 wt% SO_3 and contains jarosite at the ~10 wt% level [*Klingelhöfer et al.,* 2004; *Morris et al.,* 2006]. Positive correlations between Mg and S in Alpha Particle X-

Ray Spectrometer data suggest the presence of Mg-bearing sulfate minerals in ET2 [*Rieder et al.*, 2004; *Clark et al*., 2005]. The bulk of Pm is composed of low albedo basaltic sand [*Christensen et al*., 2000] that was transported into the region via aeolian processes and was not derived from erosion of underlying sulfate-rich bedrock [*Squyres et al*., 2004; *Arvidson et al.,* 2006]. The hematite signature detected in orbital Mars Global Surveyor (MGS) Thermal Emission Spectrometer (TES) [*Christensen et al*, 2000] infrared (IR) spectra [*Christensen et al*, 2001] of Ph results from hematitic concretions that weathered out of ET2 and concentrated at the surface via aeolian processes [*Squyres et al*., 2004; *Klingelhoefer et al.,* 2004; *Morris et al.*, 2006; *Arvidson et al*., 2006]. Pm discontinuously covers the surface of Ph in some areas and patches of ET2 are visible in high resolution orbital images of Ph.

Crater counting of Ph indicates a Late Noachian to Early Hesperian age for ET2 [*Arvidson et al*., 2006] whereas crater counting restricted to small craters (< 250 m diameter) suggests a Late Amazonian crater retention age for Pm [*Lane et* al., 2003]. Ph is a few hundred meters thick in some areas but is an order of magnitude thinner near its northern margin. The surface of Ph is aerially dominated by Pm. *Christensen and Ruff* [2004] noted that the extent of the hematite-bearing mantle is largely controlled by the extent of underlying bedrock. Because the bedrock component (ET2) and the mantle component (Pm) of Ph appear to be coupled, the extent of Pm is a proxy for the presence of underlying ET2. In this paper, Ph is mapped based on a combination of high TES hematite index values [*Christensen et al.*, 2001; *Christensen and Ruff,* 2004] and geomorphic expression.

OMEGA spectra of Ph are relatively flat in the NIR (1.0 to 2.5 μm) and are consistent with a mixture of unaltered to weakly altered basaltic sand, gray hematite, and nanophase iron oxides [*Arvidson et al*., 2006]. Distinctive H_2O and/or OH related spectral absorption features indicative of hydrated and/or hydroxylated sulfates were not identified in OMEGA spectra of Ph. Initial analyses of higher resolution CRISM spectra over the Opportunity rover landing site [*Wiseman et al*., 2007] are consistent with *Arvidson et al*. [2006].

4.2.4 Formation Mechanisms for ET1 and ET2

A brief discussion of proposed formation mechanisms for ET2 is presented first because more observational constraints exist for it than for ET1. The bedrock explored by the Opportunity rover, part of ET2, is most commonly interpreted as a "dirty" sulfate-rich evaporitic deposit composed of reworked materials that formed in an inter-dune playa environment [e.g., *Grotzinger et al.,* 2005; *Arvidson et al.,* 2006; *McLennan et al*., 2005; *Morris et al.,* 2006; *Squyres et al.,* 2006]. Other formation hypotheses including volcanic [*McCollum and Hynek*, 2005] and impact surge [*Knauth et al*., 2005] were also proposed. Although most outcrops investigated by the Opportunity rover are interpreted as cemented aeolian deposits, some primary sedimentary features consistent with subaqueous deposition are also observed [*Grotzinger et al*., 2005]. The hematitic concretions within ET2 may have formed via hydrolysis of jarosite during diagenesis [*McLennan et al.,* 2005; *Golden et al.*, 2008]. The presence of jarosite implies that low pH (0 - 4) [*Stoffregen et al.,* 2000; *Morris et al*., 2006] and oxidizing aqueous conditions

occurred during formation and/or diagenesis of ET2.

Regardless of the sediment source, ET2 experienced aqueous alteration, likely within a ground water-dominated environment [*Andrews-Hanna et al.,* 2007, 2008]. A hydrologic model that includes rainfall, ground water infiltration, and ground water emergence predicts that some sites in Sinus Meridiani hosted persistent ground water emergence and evaporation driven by the unique topography of the southwestern Arabia Terra region [*Andrews-Hanna et al.,* 2007, 2008]. Ground water upwelling in the absence of an enclosing basin provides a plausible mechanism for the extensive formation of evaporitic deposits in Meridiani Planum.

Prior to the MER Opportunity and the MEX OMEGA missions, several authors suggested a sedimentary aeolian or pyroclastic origin for ET1 [e.g., *Tanaka et al.,* 1986; *Schultz and Lutz,* 1988; *Arvidson et al*., 2003; *Hynek et al*., 2003]. Subaqueous deposition was also considered [*Edgett* and *Parker*, 1997]. However, after evaporitic process were inferred from Opportunity rover observations of overlying ET2 materials and hydrated exposures were detected in OMEGA spectra of ET1, *Arvidson et al*. [2006] and *Poulet et al*. [2008] favored formation of ET1 in ground-water driven regimes. The variable spectral and morphologic characteristics of ET1 and ET2 suggest that geochemical conditions changed during the formation of these deposits. More neutral or mildly acidic aqueous conditions likely transitioned to the low pH geochemical environment inferred from the presence of jarosite in ET2 [*Poulet et al*., 2008].

4.3 Data Sets and Methods

4.3.1 CRISM and OMEGA Data Preprocessing

The CRISM spectrometer aboard MRO is a hyperspectral imager that has short (S) and long (L) wavelength detectors that operate between 0.36 to 1.06 μm and 1.00 to 3.94 μm, respectively [*Murchie et al.,* 2007, 2009a]. CRISM is capable of acquiring both hyperspectral (544 channels) and multispectral (72 band subset) images. Hyperspectral full resolution targeted (FRT) images at a spatial resolution of 20 m/pixel, hyperspectral half resolution long (HRL) and short (HRS) targeted images at 40 m/pixel, multispectral survey (MSP) image at 200m/pixel, and multispectral window (MSW) images at 100 m/pixel were analyzed. The CRISM spectrometer utilizes 2-dimensional detector arrays that cause slight column dependencies in CRISM data [*Murchie et al*., 2007].

The OMEGA spectrometer [*Bibring et al.*, 2004, 2005] covers the wavelength range from 0.35 to 5.1 μm in 352 channels using VNIR (0.35 to 1.07 μm), C (0.93 to 2.70 μm), and L (2.53 to 5.10 μm) detectors. OMEGA images vary in spatial resolution depending on spacecraft altitude and are acquired in 16, 32, 64, or128 pixel modes. Analyses were limited to OMEGA images with spatial resolutions ≤ 2.5 km/pixel. The OMEGA spectrometer utilizes a 1-dimensional NIR detector in which images are built up by across track scanning and along track orbital motion.

Spectral analyses used CRISM L spectrometer and OMEGA C spectrometer data and were limited to the NIR wavelength region between 1.0 and 2.5 μm in which reflected solar radiation dominates the signal. CRISM and OMEGA I/F spectra (where I/F is the radiance at sensor, I, divided by the solar irradiance, F, at the top of the Martian

atmosphere divided by π) were calibrated as described by *Murchie et al*., [2007, 2009a] and [*Bibring et al.*, 2004, 2005] respectively. For most analyses, atmospheric gas bands were removed to first-order by ratioing I/F spectra to a scaled atmospheric transmission spectrum derived from Olympus Mons high and low altitude observations [*Langevin et al.,* 2005; *Murchie et al*., 2006; *Mustard et al*., 2008; *Wiseman et al*., 2009]. Surface Lambert Albedo spectra (i.e., atmospherically corrected spectra assuming isotropic surface scattering) were retrieved from selected CRISM *I*/*F* spectra using Discrete Ordinate Radiative Transfer (DISORT) [*Stamnes et al*., 1988; *Wolff et al.*, 2009] model results. Atmospheric gas and dust contributions were simultaneously accounted for in the DISORT models and removed during atmospheric correction using procedures outlined by *Wiseman et al*. [2009].

Spectral parameter maps designed to detect spectral features at wavelengths of known H_2O and/or OH vibrational features indicative of hydrated and/or hydroxylated phases [e.g., *Pelkey et al.* 2007] were generated from atmospherically corrected CRISM and OMEGA observations. Parameter calculations and threshold values are defined in Table 4.1. CRISM parameter maps were spatially filtered to reduce speckling from noise [*Parente*, 2008; *Murchie et al*., 2009a]. Isolated pixels with relatively high parameter values were assumed to result from noise and not surface contributions. A sliding kernel was used to determine areas that had a high density of pixels (9 out of 16) with relatively high parameter values (Table 4.1). All parameter values within the kernel were retained unaltered if the 9 out of 16 criterion was met and parameter values within kernels that did not meet the criterion were set to 0.

Spectral ratios were used to suppress instrumental and/or residual atmospheric artifacts and to highlight spectral features of interest. These ratios were calculated by dividing an atmospherically corrected CRISM spectrum (typically the average of 25 spectra) by a relatively bland spectrum from the same image. Numerator and denominator spectra for spectral ratios were extracted from the same CRISM columns. Because artifacts can be introduced in ratio spectra, the shapes of numerator and denominator spectra were also considered in detailed analyses.

4.3.2 Identification of Spectral Features

Detailed spectral analyses focused on identification of candidate phases responsible for producing H_2O and/or OH related vibrational features detected in CRISM spectra. Spectrally dominate hydrated and/or hydroxylated mineral phases were determined by comparing band positions of spectral absorption features in CRISM spectra with spectra of terrestrial samples contained in publically available spectral libraries (Figure 4.2) [*Clark et al.,* 2007; *CRISM Science Team*, 2006; *Cloutis et al*., 2006]. Spectra contained in the libraries were typically acquired at ambient terrestrial conditions or in an environment that was purged with nitrogen for a limited time interval. Experiments in which hydrated and/or hydroxylated mineral samples were exposed to Martian surface-like conditions for long durations showed that characteristic H_2O and/or OH related vibrational features of stable phases measured were persistent but that some absorption features, particularly H_2O related features, did decrease in amplitude [*Cloutis et al*., 2007; *Morris et al*., 2009]. Spectral features apparent in Martian spectra are not

expected to match perfectly with library spectra because multiple phases and/or phases that deviate in composition from those contained in the spectral libraries likely contribute to the Martian spectra.

NIR spectra are dominated by contributions from the upper 100s of micrometers of exposed materials. Spectral contrast and intensity are affected by multiple parameters that include mineralogy, grain size, and surface texture. Some phases are spectrally bland in the NIR (e.g., Fe-free anhydrous silicate minerals) and spectra of intimately mixed materials are nonlinear with respect to component proportions. Coatings that are not representative of the bulk mineralogy can contribute disproportionally to spectra.

Some hydrated and hydroxylated minerals exhibit distinctive spectral features in the NIR resulting from vibrational modes of H_2O and/or OH that can be spectrally diagnostic of the presence of a mineral or mineral group. OH related vibrations caused by bound OH commonly produce diagnostic spectral features. A broad H_2O related spectral absorption feature near 1.9 μm indicates that the H_2O molecule is present in some form in a material (e.g., trapped H_2O, absorbed H_2O, adsorbed H_2O, or bound H_2O). Therefore, exposures that exhibit a ~1.9 μm spectral absorption feature that lack other diagnostic vibrational bands are identified nonspecifically as hydrous materials (Figure 4.2a).

Surfaces with spectral absorption features near 1.9 (H_2O-related) and 2.3 μm (OH-related) are evident in D1900 and D2300 parameter maps (Table 4.1) of the study area in northern Sinus Meridiani. Phyllosilicates with Fe and/or Mg in octrahedral sites typically exhibit vibrational features caused by OH bound to Fe and/or Mg (e.g., Fe-OH

and Mg-OH) near 2.3 μm whereas Al-rich phyllosilicates typically exhibit distinct Al-OH related vibrational features near 2.2 μm. Spectral absorption features near 2.2 μm were not identified in current CRISM and OMEGA coverage of the study area.

Saponite, a Mg-rich trioctahedral smectite, has distinct spectral absorption features near 1.4, 1.91 (H_2O-related), 2.31 (Mg-OH vibration), and a weak feature at 2.39 μm [*Clark et al.,* 1990]. The feature at 2.39 μm is caused by the presence of OH or H_2O in the mineral structure; however a band assignment has not been made [*Decarreau* et al., 2008]. Nontronite, an Fe^{3+} dioctahedral smectite, has absorption features near 1.4, 1.9, and 2.28 (Fe^{3+}-OH vibration), and 2.4 μm [Bishop et al., 2002; *Frost et al*., 2002]. Increased proportions of Mg to Fe in smectite clays shift the ~2.3 μm band to slightly longer wavelengths [*Bishop et al.,* 2002, *Swayze et al.,* 2002]. Chlorite is another common Fe/Mg phyllosilicate mineral group that has spectral absorption features near 1.4 and 2.3 μm [*King and Clark,* 1989]. Because chlorite contains OH but lacks H_2O in its structure, spectra of pure samples should lack an absorption feature near 1.9 μm. The ~2.3 μm Fe/Mg-OH absorption feature in several chlorite spectra contained in the USGS spectral library [*Clark et al.,* 2007] occurs at slightly longer wavelengths (between 2.32 and 2.33 μm) than the corresponding Fe/Mg-OH feature in Fe/Mg smectites (Figure 4.2b).

Surfaces that exhibit spectral absorption features near 1.9 (H_2O-related) or 2.1 (H_2O-related) plus 2.4 μm (H_2O- and/or OH-related) are also evident in the study area in D1900, D2100, and D2400 parameter maps (Table 4.1). Spectra of Mg and/or Fe polyhydrated sulfate minerals, or hydrated sulfates with multiple water molecules per unit

cell [*Hawthorne et al*., 2000], exhibit absorption features near 1.9 and 2.4 μm [*Cloutis et al*., 2006]. Monohydrated Mg and Fe sulfates exhibit band minima near 2.1 and 2.4 μm [*Cloutis et al*., 2006]. Some sulfate minerals, including gypsum (Ca polyhydrated sulfate), alunite (Al hydroxylated sulfate), and jarosite (Fe^{3+} hydroxylated sulfate), exhibit spectral absorption features near 2.20 to 2.27 μm that were not identified in the study area in northern Sinus Meridiani.

The central wavelength position of absorption features near 1.9 μm in spectra of polyhydrated sulfates is affected by hydrogen bonding and the number of structurally distinct sites occupied by H_2O molecules [*Cloutis et al*., 2006]. Overlapping H_2O absorption features can result in the appearance of a broad feature near 1.9 μm in spectra of some polyhydrated sulfate minerals. Band minima between 1.93 and 1.98 μm are commonly observed in spectra of Mg and/or Fe polyhydrated sulfates (Figure 4.2c) [*Cloutis et al*., 2006]. Assignment of the ~2.4 μm micron feature is equivocal because a feature at this wavelength is detected in spectra of both hydrated sulfate minerals and non-sulfate hydrated phases [*Crowley et al*., 2003; *Bishop et al.*, 2005; *Bishop and Maurd* 2005; *Decarreau et al*., 2008].

The spectral feature resulting from H_2O typically observed near 1.9 μm is shifted to ~2.1 μm in spectra of monohydrated sulfates as a consequence of strong hydrogen bonding (Figure 4.2d) [*Cloutis et al*., 2006]. The Mg and Fe^{2+} monohydrated sulfates kieserite and szomolnokite are structurally similar. Spectra of naturally occurring kieserite exhibit an H_2O feature near 2.13 μm and szomolnokite spectra exhibit an H_2O feature near 2.10 μm (Figure 4.2d). Additional laboratory studies are needed to confirm

whether there is a systematic relationship between the central wavelength position of the ~2.1 μm spectral feature and the dominant cation in monohydrated sulfates.

4.3.3 Image and Topographic Data

CTX images (5 m/pixel), HiRISE images (35 cm/pxiel), MGS Mars Orbital Camera (MOC) [*Malin et al*., 1992] wide angle (WA) mosaics (230 m/pixel), Mars Odyssey Thermal Emission Imaging System (THEMIS) [*Christensen et al.,* 2004] daytime and nighttime IR scaled brightness mosaics (230 m/pixel) at 12.57μm, MGS Mars Orbiter Laser Altimeter (MOLA) [*Smith et al.,* 2001] gridded topography mosaics (450 m/pixel), and MOLA profile point data (150 m footprint) were utilized for geomorphic and topographic analyses. CRISM spectral reflectance observations were also displayed and analyzed as three band false color composite images. Data visualization and analysis were performed using IDL/ENVI and GIS software. Map coordinates were defined in aerocentric latitude and positive east longitude.

Relative stratigraphic positions of materials based on embayment and superposition relationships were inferred from morphologic expression and analyses of shadowed or sunlit margins in HiRISE, CTX, and MOC images. THEMIS daytime and nighttime thermal IR scaled brightness mosaics were used to compare relative differences in material properties. Geomorphic variations are evident in daytime images acquired in the late afternoon, partially as a result of differential solar heating. Nighttime brightness temperatures are controlled by physical properties of the surface and are dominated by thermal inertia. Reported material thicknesses were estimated from MOLA profile

elevation point data.

4.4 Spectral and Stratigraphic Mapping in Northern Sinus Meridiani

Well exposed contacts between Ph, ET1, and CT facilitate stratigraphic analyses in northern Sinus Meridiani (Figure 4.3). Previous analyses of OMEGA NIR spectral reflectance observations revealed mono- and poly- hydrated sulfates within layered deposits associated with a ~120 km long northwest-southeast trending valley [*Gendrin et al.*, 2005; *Arvidson et al*., 2005; *Griffes et al.,* 2007] and Fe/Mg phyllosilicate-bearing exposures within a 50 km diameter crater [*Poulet et al*., 2008] (Figure 4.3, red and green arrows). Detailed stratigraphic and spectral analyses are focused on a region in northern Sinus Meridiani located between 1º N to 5º N latitude and 3º W to 1º E longitude (Figure 4.4).

Detailed morphologic, stratigraphic, and spectral analyses of materials within the study area are presented in sections 4.4.1 through 4.4.5 and implications of these results are discussed in section 4.5. We subdivided ET1 into four laterally continuous subunits, $ET1_A$, $ET1_B$, $ET1_C$, and $ET1_D$, based on the geomorphic expression of ET1 materials and their superposition relationships (Figure 4.4b and 4.4c). Layered deposits associated with the northwest-southeast trending valley located in the center of the study area that exhibit hydrated sulfate spectral signatures are distinguished from ET1 and are mapped as *Layered Hydrated Sulfate* (LHS) deposits. Upper layers associated with the northeastern margin of the LHS deposits are mapped as the *Layered Hydrated Sulfate Cap* (LHS_{cap}) (Figure 4.4b). The possibility that LHS_{cap} is laterally continuous with $ET1_D$ is shown in

Figure 4.4d and is considered in section 4.5.3. Areas of ET1, LHS, and LHS_{cap} that are mantled with dark material are classified as $[ET1/LHS/LHS_{cap}]_{mantled}$ (Figure 4.4b).

CRISM and OMEGA parameter maps of the study area are shown in Figure 4.5. Red areas exhibit spectral features near 2.4 μm plus ~1.9 μm or 2.4 μm plus ~2.1 μm, consistent with the presence hydrated sulfates. Green areas exhibit a feature near 2.3 μm that is typically caused by Fe/Mg-OH vibrations in Fe/Mg phyllosilicates (Figure 4.5).

4.4.1 CT, Northern Sinus Meridiani

Several impact craters within CT in northern Sinus Meridiani are partially filled with high thermal inertia intracrater deposits (Figure 4.1c). A prominent northwest-southeast trending ridge and adjacent valley occur in the center of the study area (Figure 4.3a). Intercrater surfaces of CT are predominately low in albedo (Figure 4.3b) and are relatively smooth (Figure 4.6), retain small impact craters, and have polygonal fractures in some areas (Figure 4.6c, yellow inset). Small channel features that sometimes transition to sinuous ridges occur in CT (Figure 4.6c, white arrow). These sinuous ridges are similar to other features in Sinus Meridiani that were interpreted as inverted channels, or channel features that were filled with material that is more resistant to erosion than the surface into which the channel was originally incised [*Newsom et al*., 2003; *Edgett*, 2005; *Newsom et al*., 2009]. Channel features are buried by ET1 (Figure 4.6c), which indicates that channel formation predated emplacement of ET1. Dark surfaces of CT exhibit a basaltic spectral signature (Figure 4.7, labeled '(7a) FRT000099C8_den CT', location shown in Figure 4.8) [*Poulet et al*., 2008].

4.4.1.1 Phyllosilicate-bearing Exposures in CT

Fe/Mg phyllosilicate-bearing deposits were previously detected on the floor of a 50 km diameter crater in the study area in northern Sinus Meridiani (Figure 4.5) [*Poulet et al*., 2008]. CRISM spectra extracted from these deposits are similar to OMEGA spectra [*Poulet et al*., 2008] and exhibit spectral absorption features centered near 1.91 and 2.31 μm, weaker features near 1.4 and 2.39 μm, and a shoulder near ~2.24 μm (Figure 4.7, labeled '(7b) FRT0000960F'). The spectral features at 1.41, 1.91, 2.31, and 2.39 μm are consistent with contributions from Mg-rich smectite (Figure 4.2b). The shape of the 2.31 band and the shoulder near ~2.24 μm may result from the presence of chlorite in addition to Mg-rich smectite (Figure 4.2b). Alternatively, the shoulder near ~2.23 μm could be produced from Al-OH vibrations resulting from substitution of Al into octahedral sites in the Mg-rich smectite [e.g., *King and Clark*, 1989]. Additional exposures that exhibit spectral absorption features near 2.3 μm are detected in CT in CRISM image FRT000099C8 on and to the north of rampart ejecta [*Barlow et al*., 2000] from a 16 km diameter impact crater (Figure 4.8). Spectral features centered near 1.92 and 2.30 to 2.31 μm and weaker features at ~1.4 and 2.39 μm (Figure 4.7, labeled '(7a) FRT00099C8') are consistent with the presence of Fe/Mg smectites (Figure 4.2b).

4.4.2 $[ET1/LHS/LHS_{cap}]_{mantled}$ Description

Where well exposed, surfaces of ET1, LHS, and LHS_{cap} have intermediate to high

albedos and relatively high thermal inertias (Figure 4.1c and Figure 4.3b). Some portions of ET1, LHS, and LHS_{cap} are mantled by low albedo, relatively low thermal intertia material. Where the dark mantle covers small areas, the unit underlying the mantle can be inferred from surrounding exposures. However, in areas where the mantle is relatively extensive, identification of the underlying unit (e.g., $ET1_A$, $ET1_B$, $ET1_C$, $ET1_D$, LHS or LHS_{cap}) is difficult. Therefore, mantled areas that are laterally continuous with or occur at similar stratigraphic levels as $ET1_A$, $ET1_B$, $ET1_C$, $ET1_D$, LHS, or LHS_{cap} were classified as $[ET1/LHS/LHS_{cap}]_{mantled}$ and specific assignment of the unit(s) underlying the mantle was not made (Figure 4.4b).

The dark mantle material commonly occurs in the vicinity of impact craters deep enough to have excavated and emplaced CT as ejecta deposits on surrounding surfaces. The dark mantle component of $[ET1/LHS/LHS_{cap}]_{mantled}$ located in the eastern portion of the study area adjacent to a 30 km diameter impact crater appears to have originated as ejecta from the 30 km diameter crater (Figure 4.3 and Figure 4.4b, white arrow). High thermal inertia light-toned layers that stand ~200 m above CT are visible in exposures along the western margin of this mantled area (Figure 4.9). Continuous ejecta deposits mantle ET1 shown in Figure 4.10a and remnants of dark ejecta mantle the surface of ET1 shown in Figure 4.10c.

4.4.3 ET1, Northern Sinus Meridiani

Multiple outliers of ET1 that are separated by 10s of kilometers from larger exposures occur in northern Sinus Meridiani (Figure 4.3). The smallest outliers of ET1

surround craters and may have been armored from erosion by crater ejecta deposits, resulting in pedestal-like craters (Figure 4.4b). The presence of outliers of ET1 suggests that substantial differential erosion occurred in this region [*Hynek and Phillips*, 2001; *Hynek et al*., 2002].

4.4.3.1 $ET1_A$, $ET1_B$, $ET1_C$, and $ET1_D$ Descriptions

Four geomorphically distinct subunits of ET1, $ET1_A$, $ET1_B$, $ET1_C$, and $ET1_D$, were identified in the study area in northern Sinus Meridiani (Figure 4.4b). $ET1_A$ is the stratigraphically lowest subunit within ET1 and $ET1_D$ is the stratigraphically highest subunit (Figure 4.4c). $ET1_A$, $ET1_B$, and $ET1_C$ are consistently exposed in the southern and western portion of the study area and in outliers of ET1 that occur to the north (Figure 4.4b). $ET1_D$ is exposed in the eastern portion of the study area (Figure 4.4b). Subunits are described in reverse stratigraphic order with the exception that $ET1_D$ is presented last.

$ET1_C$ commonly exhibits a distinctive knob to ridged morphology that is visible at intermediate spatial scales (10s to 100s of meters) (Figure 4.11). Analyses of CTX images show that the knobs and ridges are traceable to more continuous material that is preserved near the margin of overlying Ph (Figure 4.11c). Thus, the knob and ridges appear to be an erosional morphology of $ET1_C$. The thickness of $ET1_C$ is difficult to determine because it caps ridges whose walls may consist of stratigraphically lower materials. The thickness of $ET1_C$ is estimated at 10 to 30 m. A spectral absorption feature near 2.3 μm is detected in some exposures of $ET1_C$ located in the southwestern

portion of the study area (Figure 4.5, green pixels). Spectra extracted from the surface of $ET1_C$ covered by CRISM image FRT000097F8 (Figure 4.12) exhibit spectral absorption features centered near 1.92, 2.30 to 2.31 μm, and 2.39 μm (Figure 4.7, labeled '(7c) FRT000097F8 $ET1_C$'), consistent with the presence of Fe/Mg smectite (Figure 4.2b).

$ET1_B$ occurs stratigraphically below $ET1_C$ and is exposed in surfaces intervening remnant knobs and ridges of $ET1_C$ (Figure 4.11). $ET1_B$ is relatively smooth at intermediate and small spatial scales (Figure 4.11c, 4.11e). $ET1_B$ is estimated to be 40 and 60 m thick. Spectra of $ET1_B$ extracted from FRT000097F8 (Figure 4.11) exhibit a shallow H_2O related absorption feature near 1.92 μm and an indistinct spectral drop-off at wavelengths longward of ~2.2 μm (Figure 4.13, labeled '(13a) FRT000097F8 $ET1_B$'). This spectral shape is consistent with spectra of multiple hydrated phases, including hydrous hydroxides and some hydrated ferric sulfates (Figure 4.2a). A small exposure of material with spectral features near ~1.9 and 2.4 μm, indicative of the presence of polyhydrated sulfates, is also detected in FRT000097F8 (Figure 4.12b, magenta pixels). This spectral signature is not representative of $ET1_B$ and will be discussed in section 4.4.5.

$ET1_A$ is the stratigraphically lowest subunit of ET1 and is exposed in heavily eroded areas that include plateau or mesa walls and low regions surrounding mesas (Figure 4.6 and Figure 4.14). $ET1_A$ has a higher albedo than $ET1_B$ and $ET1_C$ and exhibits a distinctive scalloped texture that is visible in HiRISE images (Figure 4.6d and Figure 4.14b, red inset). The thickness of $ET1_A$ is variable and appears to be controlled by underlying CT topography. The thickest exposures of $ET1_A$ (~150 m thick) occur in a

scarp wall located along the southern margin of the northeast-southwest trending valley (Figure 4.4b). $ET1_A$ is well exposed in a portion of the scarp wall covered by CRISM image FRT0001252F (Figure 4.14c). Although spectral signatures indicative of hydrated sulfates are present in FRT0001252F, they occur in association with LHS deposits and are not detected in $ET1_A$. Instead, spectra extracted from $ET1_A$ are relatively bland between ~1.0 and 2.5 μm and do not exhibit obvious H_2O and/or OH related vibrational features (Figure 4.13, labeled '(13b), FRT0001252F $ET1_A$').

$ET1_D$ is identified in the eastern portion of the study area and occurs stratigraphically above $ET1_C$ (Figure 4.15). Multiple strata within $ET1_D$ are exposed along a ~70 m topographic rise that occurs near the margin between $ET1_C$ and $ET1_D$ (Figure 4.15d). $ET1_D$ contacts with ET2 for a short interval (Figure 4.15) and appears to underlie ET2; however this interpretation is not definitive and it is possible that $ET1_D$ actually postdates ET2 formation. Spectra extracted from $ET1_D$ in CRISM image FRT0000CC22 (Figure 4.16) exhibit pronounced H_2O related absorptions features near 1.92 μm and an indistinct spectral drop-off at wavelengths longward of ~2.2 μm (Figure 4.13, labeled '(13c) FRT0000CC22 $ET1_D$' and '(13d) FRT0000CC22_$ET1_D$') that is consistent with spectra of multiple hydrated phases that include hydrous hydroxides and some hydrated ferric sulfates (Figure 4.2a). Similar spectral shapes are observed in ET1 located to the east of the study area *Poulet et al*. [2008]. Polyhydrated sulfate spectral signatures were detected along the margin of low albedo mantle in FRT0000CC22 (Figure 4.16b, magenta pixels) that will be detailed in section 4.4.5.

4.4.4 LHS and LHS_{cap}

4.4.4.1 LHS and LHS_{cap} Descriptions

Layered Hydrated Sulfate (LHS) deposits are exposed on the floor of the northwest-southeast trending valley located in the center of the study area and within higher elevation plateaus near the northeastern margin of the valley (Figure 4.17 and Figure 4.18). LHS deposits exhibit spectral absorptions features near ~1.9 plus 2.4 μm and ~2.1 plus 2.4 μm, indicative of mono- and poly- hydrated sulfates, respectively (Figure 4.5). Polyhydrated sulfates are spectrally dominant over a large area of the valley floor and monohydrated sulfates occur on the western portion of the valley floor and in higher elevation, plateau-forming exposures in the northeastern portion of the LHS deposits (Figure 4.5 and Figure 4.17b) [*Griffes et al*., 2007]. Analyses of high resolution CRISM, CTX, and HiRISE images reveal that layers containing monohydrated sulfates are intercalated with polyhydrated layers near the northeastern margin of the LHS deposits (Figure 4.19 and Figure 4.20). Polyhydrated spectral signatures are detected in both low and high albedo layers but monohydrated sulfate spectral signatures are typically associated with relatively low albedo layers within the LHS deposits (Figure 4.19). LHS deposits exhibit erosional pits and grooves at small to intermediate spatial scales (Figure 4.19d).

CRISM spectra extracted from areas with high D1900 and D2400 parameter values in FRT00004616 exhibit broad spectral absorption features centered near 1.94 μm and a reflectance drop off longward of ~2.3 μm with a band minimum near 2.39 to 2.40 μm (Figure 4.21, labeled '(21) FRT00004616 LHS_poly') that is spectrally consistent

with the presence of Mg and/or Fe polyhydrated sulfates (Figure 4.2c). CRISM spectra extracted from areas with high D2100 and D2400 parameter values exhibit a spectral absorption feature centered near 2.13 μm and a reflectance drop off longward of ~2.3 μm with a well defined band minimum near 2.40 μm (Figure 4.21, labeled '(21b) FRT00004616 LHS_mono'). Although a band centered at 2.13 μm is more consistent with spectra of the Mg monohydrated sulfate kieserite than spectra of the Fe monohydrated sulfate szomolnokite (Figure 4.2d), the relationship between the wavelength center of the spectral feature at ~2.1 μm and cation is not well established. CRISM spectra extracted from LHS deposits also typically exhibit a broad spectral absorption feature centered near ~1 μm (Figure 4.21). This electronic feature could arise from the presence of ferric hydrated sulfate minerals or from contributions by other ferric hydrous or anhydrous phases that occur in the CRISM pixels from which the spectra were extracted. Low albedo aeolian deposits that have a basaltic spectral signature similar to spectrum '(7a) FRT000099C8_den CT' shown in Figure 4.7 are observed in the valley.

The LHS_{cap} occurs on plateau surfaces (Figure 4.18) and is higher in albedo and smother at intermediate spatial scales than LHS deposits (Figure 4.19d). Multiple small mesas capped by LHS_{cap} are visible in highly eroded areas adjacent to larger exposures of the LHS_{cap} (Figure 4.18d). Spectra extracted from the LHS_{cap} in FRT00004616 (Figure 4.19) exhibit an H_2O related feature at 1.92 μm and an indistinct spectral drop-off at wavelengths longward of ~2.2 μm (Figure 4.21, labeled '(21c) FRT00004616 LHS_{cap}') that is consistent with spectra of multiple hydrated phases that include hydrous hydroxides and some hydrated ferric sulfates (Figure 4.2a).

4.4.4.2 Stratigraphic Analyses - LHS and LHS_{cap}

A ~200 m section of ET1 is exposed along the southern margin of the LHS deposits in which both steep faces and more gradual slopes are observed (Figure 4.17). Hydrated sulfate spectral signatures are not identified in existing high resolution CRISM coverage of the scarp wall. Instead, hydrated sulfate detections are limited to LHS deposits that occur on the valley floor (Figure 4.14c). $ET1_A$ is visible at the base of the section of ET1 exposed in the southern scarp wall (Figure 4.17). The configuration of the contact along the southern margin of the valley suggests that the LHS deposits either underlie or embay $ET1_A$. However, the stratigraphic relationship between LHS deposits and $ET1_A$ is difficult to determine from analysis along this margin because aeolian debris obscures direct contacts between the two units (Figure 4.14). Mesas that consist of $ET1_A$, $ET1_B$, and $ET1_C$ occur near the center of the valley (Figure 4.22). LHS deposits on the valley floor appear to embay $ET1_A$ that is exposed in these mesa walls (Figure 4.22).

Exposures along the northern margin of the LHS deposits show that LHS deposits are stratigraphically above CT. LHS deposits embay and partially cover rampart ejecta from a preexisting crater in CT (Figure 4.18). LHS deposits also embay a channel feature eroded into the surface of CT that extends to the north and cuts a northwest-southeast trending ridge (Figures 4.17c). This embayment and cross cutting relationship establishes that emplacement of LHS deposits postdates the formation of the ridge within CT.

Layers within the LHS deposits terminate in low mesas along their northwestern margin (Figure 4.23). High albdeo material is exposed at the base of the low mesas

(Figure 4.23). Some exposures of the underlying light toned material have the distinctive scalloped morphology characteristic of $ET1_A$ (Figure 4.23c). Analyses of CRISM spectra in conjunction with higher resolution CTX and HiRISE images indicate that these areas do not exhibit distinctive hydrated sulfate spectral signatures (Figure 4.23b). The LHS deposits shown in Figure 4.23c overlie the small exposure of $ET1_A$.

LHS_{cap} appears to occur stratigraphically above LHS (Figure 4.18d and Figure 4.19). Multiple layers in the LHS deposits are exposed in areas surrounding LHS_{cap}, with higher elevation layers occurring closest to LHS_{cap}. Analysis of HiRISE anaglyph PSP_002680_1825_PSP_003392_1825, which covers deposits shown Figure 4.19d, does not reveal obvious deformation textures or steeply dipping beds. Instead layers at multiple elevations within the LHS deposits appear to be exposed as a result of differential erosion.

4.4.5 Additional Hydrated Sulfate Exposures in Northern Sinus Meridiani

Materials that exhibit hydrated sulfate spectral signatures are not restricted to LHS deposits. Polyhydrated sulfates occur in a topographic low to the northwest of the LHS deposits and exposures containing mono- and poly- hydrated sulfate spectral signatures were identified to the north of LHS deposits in low areas near the bases of high-standing outcrops in two locations (Figure 4.5). Polyhydrated sulfate spectral signatures were also detected in limited exposures on high-standing surfaces of ET1 located to the southwest, south, and east of the LHS deposits (Figure 4.5).

4.4.5.1 Hydrated Sulfate Exposures Located to the North of LHS Deposits

Polyhydrated sulfates detected ~20 km to the northwest of LHS deposits occur in a topographic low that is an extension of the northwest-southeast trending valley (Figure 4.24). These polyhydrated sulfates occur at a similar elevation as the LHS deposits and in a similar setting, e.g., at the base of a heavily eroded section consisting of $ET1_A$, $ET1_B$, and $ET1_C$. Mono- and poly- hydrated sulfates were detected near the base of $[ET1/LHS/LHS_{cap}]_{mantled}$ located ~40 km to the northeast of the LHS deposits in CRISM image FRT000099C8 (Figure 4.8) and FRT0000893E (Figure 4.25). These exposures occur at a similar elevation to upper layers of the LHS deposits. Exposures closest to the base of $[ET1/LHS/LHS_{cap}]_{mantled}$ are mantled with low albedo fines and/or high albedo dust. The stratigraphic relationships of the hydrated sulfate-bearing materials is difficult to determine because the hydrated sulfate exposures are limited in spatial extent and partially obscured by aeolian deposits. The hydrated sulfates either underlie or embay the higher-standing mesas of $[ET1/LHS/LHS_{cap}]_{mantled}$ and ET1. Spectra extracted from the hydrated sulfate bearing materials have relatively weak absorption features, consistent with contamination from mobile fines (Figure 4.26, labeled '(26a) FRT000099C8 poly' and '(26b) FRT0000893E poly'). A restricted exposure of material with a monohydrated sulfate spectral signature (Figure 4.26, labeled '(26c) FRT000099C8_mono') also occurs ~5 km from the base of $[ET1/LHS/LHS_{cap}]_{mantled}$ in FRT000099C8 (Figure 4.8).

Both mono- and poly- hydrated spectral signatures were also detected in materials that occur near the base of an outlier of ET1 located ~130 km to the north of LHS deposit (Figure 4.27). The outlier of ET1 is partially eroded and multiple mesas of ET1 occur in

which $ET1_A$, $ET1_B$, and $ET1_C$ are exposed (Figure 4.6). Analysis of FRT000062E6 shows that hydrated spectral signatures are restricted to materials that occur at the base of the mesas of ET1 and are not detected in mesa walls (Figure 4.27; polyhydrated sulfate example spectrum shown in Figure 4.26, labeled '(26d) FRT000062E6 poly'). This indicates that the hydrated sulfate-bearing materials were deposited subsequent to the erosion of the mesas of ET1.

4.4.5.2 Hydrated Sulfate Exposures Located in to the South, Southwest, and East of LHS Deposits

Small exposures of polyhydrated sulfates were detected to the southwest of the valley in CRISM image FRT000097F8 and are limited to a cluster of pixels located near the center of the image (Figure 4.12; spectrum shown in Figure 4.26, labeled '(26e) FRT000097F8 poly'). The material that exhibits a polyhydrated sulfate spectral signature occurs in the midst of a surface dominated by $ET1_B$ that was exposed following erosion of overlying $ET1_C$. The limited spatial extent of the polyhydrated sulfate exposures in FRT000097F8 makes stratigraphic analyses difficult. These polyhydrated sulfates were deposited either prior to the formation of $ET1_C$ or after the formation and subsequent erosion of $ET1_C$.

Material with a polyhydrated sulfate spectral signature is exposed in CRISM image FRT00003CE0 near the base of a plateau composed of Ph (Figure 4.28; spectrum shown in Figure 4.26, labeled '(26f' FRT00003CE0 poly'). The northwestern portion of FRT00003CE0 is partially mantled by aeolian debris. Polyhydrated sulfate spectral

signatures are detected in areas that are relatively free from debris. Clean exposures of $ET1_C$ located in the northeastern portion of FRT00003CE0 are spectrally similar to the $ET1_C$ spectrum extracted from FRT000097F8 and exhibit spectral absorptions features at ~1.92 and 2.30 to 2.31 μm, consistent with the presence of Fe/Mg smectites (Figure 4.7, labeled '(7d) FRT00003CE0 ET1C'). The polyhydrated sulfate exposures in FRT00003CE0 overlie $ET1_C$ and either underlie or embay Ph.

Polyhydrated sulfates are exposed in FRT0000CC22 near the margin of low albedo mantle that covers a small area of $ET1_D$ located to the east of the LHS deposits (Figure 4.16b, magenta pixels). The polyhydrated sulfates overlie $ET1_D$ and are possibly remnants of a more extensive layer that was stripped by aeolian erosion in areas unprotected by the dark mantle.

4.5 Discussion

4.5.1 Regional Overview

Three main units, heavily cratered Noachian-aged terrain, indurated rock termed 'etched' terrain, and hematite-bearing plains, are extensively exposed in Sinus Meridiani. These materials are mapped as *Cratered Terrain* (CT), *Etched Terrain 1* (ET1), and *Plains, Hematite-bearing* (Ph) in the regional context map shown in Figure 4.1. Ph is a composite unit that consists of layered, indurated rock, *Etched Terrain 2* (ET2) that is overlain by an unconsolidated veneer, the *Plains Mantle, Hematite-bearing* (Pm). ET1 unconformably overlies CT and Ph occurs at the top of the stratigraphic section.

4.5.2 Stratigraphic Relationships, Northern Sinus Meridiani

Detailed stratigraphic analyses presented in section 4.4 focused on a region in northern Sinus Meridiani located between 1º N to 5º N latitude and 3º W to 1º E longitude. ET1 was subdivided into four geomorphically distinct subunits, $ET1_A$, $ET1_B$, $ET1_C$, and $ET1_D$, that were mapped using superposition relationships (Figure 4.4b). $ET1_A$ is the stratigrahically lowest subunit of ET1 and $ET1_D$ is the stratigraphically highest subunit. The thickness of $ET1_A$ is variable (~150 m thick in places) and appears to be controlled by the underlying topography of CT. $ET1_B$ is several 10 to 30 m thick, $ET1_C$ is a 40 to 60 m thick, and $ET1_D$ is composed of multiple strata that have a combined thickness of ~70 m where exposed in the study area.

Layered deposits associated with a ~120 km long northwest-southeast trending valley located in the center of the study area that exhibit hydrated sulfate spectral signatures were mapped as *Layered Hydrated Sulfate* (LHS) deposits and upper layers in which specific hydrated sulfate spectral signatures were not identified were mapped as the *Layered Hydrated Sulfate Cap* (LHS_{cap}) (Figure 4.4b). LHS deposits are exposed on the valley floor and within higher elevation plateaus near the northeastern margin of the valley (Figure 4.17 and Figure 4.18). Detailed analyses of exposures along the margins of LHS deposits presented in section 4 show that the stratigraphic relationship among materials cannot be described by a simple layered stratigraphy in which LHS deposits underlie $ET1_A$.

4.5.2.1 Stratigraphic Relationships Between LHS Deposits and $ET1_A$, ETI_B, and $ET1_C$

We constructed two vertical cross sections from MOLA elevation profiles that transect the LHS deposits (Figure 4.29, locations shown in Figure 4.17). Both cross sections are oriented roughly parallel to regional strike, in the northeast-southwest direction. LHS deposits that are exposed within plateaus near the northeastern margin of the valley occur at significantly higher elevations than LHS deposits on the valley floor. These northeastern LHS deposits reach elevations that are similar in height to high-standing surfaces of ET1 located to the south of the valley, even if comparisons are made along the direction of regional strike, to the northeast-southwest (Figure 4.17). LHS deposits along the northeastern margin of the valley do not project to corresponding layers to the southwest of the valley (Figure 4.29b). We infer a lateral facies change to explain the observed configuration of the LHS deposits and ET1 because we found no evidence for post depositional structural deformation of the LHS deposits. Both conformable and unconformable facies changes are considered.

If the LHS deposits are conformable with ET1 then a lateral facies change occurred in response to lateral variations in local depositional conditions that resulted in an abrupt contact with ET1 along the southern margin of the valley. If the LHS deposits are unconformable with ET1 then this implies that ET1 was originally laterally continuous and subsequently eroded. LHS deposits were unconformably deposited and embay $ET1_A$ where the two units contact.

On the basis of detailed analysis presented in section 4.4, we favor an unconformable facies change in which at least $ET1_A$, $ET1_B$, and $ET1_C$ were originally

laterally continuous, subsequently eroded, and embayed by younger LHS deposits. The presence of outliers of ET1 located to the north of the LHS deposits that consist of $ET1_A$, $ET1_B$, and $ET1_C$, the same sequence of strata observed in large expanses of ET1 located to the south and west of the LHS deposits, supports the hypothesis that $ET1_A$, $ET1_B$, and $ET1_C$ were originally laterally extensive across the study area. The occurrence of exposures of $ET1_A$ in both the scarp wall along the southern margin of the LHS deposits and on the northwestern valley floor underlying LHS deposits is consistent with an unconformable facies change because $ET1_A$ is observed to be a thick, relatively easily erodible unit. The presence of isolated mesas that consist of $ET1_A$, $ET1_B$, and $ET1_C$ located in the center of the valley that appear to be embayed by LHS deposits (Figure 4.22) is consistent with an unconformable facies change and inconsistent with a conformable facies change.

4.5.2.2 Stratigraphic Relationships Between $ET1_C$, $ET1_D$, and ET2

$ET1_D$ occurs stratigraphically above $ET1_C$ and appears to underlie ET2 (the bedrock component of Ph) in the eastern portion of the study area (Figure 4.4c 1.I). However, the possibility that $ET1_D$ postdates ET2 cannot be excluded (Figure 4.4c, vertical section 1.II). $ET1_D$ is not identified in the western and southwestern portion of the study area (Figure 4.4b). The units map shown in Figure 4.4b can be produced by two possible vertical configurations: *Configuration I*) $ET1_D$ occurs between $ET1_C$ and ET2 in the western portion of the study area but was eroded back where not protected by overlying ET2 such that the margin of $ET1_D$ is approximately coincident with the margin

of ET2, making $ET1_D$ difficult to identify (Figure 4.4c, vertical section 2.I) or *Configuration II*) ET2 occurs directly stratigraphically above $ET1_C$ in the western portion of the study area (Figure 4.4c, vertical section 2.II). *Configurations I* and *II* can both be explained if $ET1_D$ was originally laterally continuous or deposition and/or diagenesis of $ET1_D$ was laterally variable. Alternatively, *Configuration I* can be explained if $ET1_D$ formation postdated ET2.

If $ET1_D$ was originally laterally continuous, then either $ET1_D$ was buried by ET2 and subsequently eroded in the western portion of the study area, resulting in *Configuration I* or $ET1_D$ was eroded prior to the unconformable deposition of ET2, resulting in *Configuration II*. However, if deposition and/or diagenesis of $ET1_D$ was laterally variable, then *Configuration I* would be observed if $ET1_D$ was originally laterally continuous but the western portion of $ET1_D$ was pervasively altered during diagenesis to form lower strata of ET2 and *Configuration II* would have resulted if deposition of $ET1_D$ was restricted to eastern locations. Alternatively, *Configuration II* would result if $ET1_D$ postdates ET2 formation (Figure 4.4c, 1.II). Discrimination between *Configuration I* and *Configuration II* is difficult because multiple hypotheses can explain both configurations and $ET1_D$ and ET2 only contact for a short interval in the eastern portion of the study area (Figure 4.15).

4.5.3 Relative Age Relationships Between LHS Deposits and $ET1_A$, $ET1_B$, $ET1_C$, $ET1_D$, and ET2

The occurrence of an unconformable facies change requires that LHS deposits are

younger than $ET1_A$, $ET1_B$, and $ET1_C$ and that LHS deposits embay $ET1_A$ (Figure 4.29) where they contact for ~120 km along their southern margin (Figure 4.17). Analyses of contacts between LHS deposits on the valley floor and $ET1_A$ exposed in scarp walls along the valley margin and in mesas in the center of the valley are consistent with the interpretation that LHS deposits embay $ET1_A$ (Figure 4.22).

Ph covers a plateau that forms the western margin the valley and occurs on surfaces to the south of the valley. LHS deposits contact with $ET1_A$ at the base of the plateau. The presence of Ph on this high surface suggests that ET2 (the bedrock component of Ph) formed prior to the erosion of ET1 and the subsequent deposition of LHS deposits. This indicates that the LHS deposits and the LHS_{cap} may be the youngest stratigraphic unit exposed in northern Sinus Meridiani and that the LHS deposits and LHS_{cap} should not be included as part of ET1 in the regional context map (Figure 4.1). .

$ET1_D$ occurs stratigraphically above $ET1_C$ and appears to underlie ET2. However, the inference that $ET1_D$ predates ET2 is not definitive and it is possible that $ET1_D$ is younger than ET2. Materials mapped as LHS_{cap} and $ET1_D$ are geomorphically and spectrally similar but are separated by surfaces covered by low albedo mantle deposits that preclude determination of the stratigraphic relationship between LHS_{cap} and $ET1_D$ (Figure 4.15). It is possible that $ET1_D$ is laterally continuous with LHS_{cap}. If so, this is not inconsistent with a relatively young age for the LHS_{cap}.

4.5.4. LHS Deposits

4.5.4.1 Original Thickness and Extent of LHS Deposits

The current exposures of LHS deposits represent a lower bound to the original extent of the deposits. There is morphologic evidence for differential erosion of the LHS deposits that includes the presence of plateaus and small scale pits and groves (Figure 4.19d). LHS deposits are ~50 m thick near their northwestern margin and ~150 m thick near their northeastern margin (Figure 4.18). LHS deposits extend to the scarp walls along the western, southern, and eastern margins of the valley. However, LHS deposits terminate in low mesas along their northwestern margin. This indicates that the LHS deposits may have originally extended further to the north (Figure 4.23). The occurrence of hydrated sulfate-bearing materials ~30 km to the northwest of the LHS deposits (Figure 4.24) in a stratigraphically similar setting as the LHS deposits provides additional evidence that the LHS deposits may have` extended further to the north. Additional hydrated sulfate-bearing materials that occur further from the margin of the LHS deposits are discussed in section 4.5.4.

4.5.4.2 Candidate Formation Environments

LHS deposits are exposed both on the valley floor and within higher elevation plateaus near the northeastern margin of the valley (Figure 4.17). Exposures directly to the northeast of the higher-standing LHS deposits and the LHS_{cap} are mantled by dark material that obscures identification of underlying units and potential contacts between

these units. Emplacement of the LHS deposits was shown via embayment and cross cutting relationships to postdate CT, which rises to form a ridge to the north of the LHS deposits (Figure 4.17b). LHS deposits were also determined to postdate the formation of the scarp wall in ET1 that forms the eastern, southern, and southwestern margin of the valley (Figure 4.17). Prior to formation of the LHS deposits, the topographic configuration of materials resulted in the presence of a nearly closed basin. The occurrence of a thick sequence of layered deposits with hydrated sulfate spectral signatures within this nearly closed valley is suggestive of deposition in an evaporitic setting.

The observed compositional layering in the LHS deposits, specifically intercalated layers of mono- and poly- hydrated sulfates (Figure 4.19 and Figure 4.20), implies that multiple wetting events and/or brine recharge occurred to produce depositional layering, although diagenetic processes may have modified the initial depositional layering. The exact depositional setting in which the LHS deposits formed is uncertain. LHS exposures could be consistent with formation in deep or shallow saline aquifers, surface brines, or some combination of these. The presence of LHS deposits at relatively high elevations along the northeastern margin of the valley implies that brines reached this level. These high elevation layers could be consistent with deposition in a deep water basin setting in which a thicker evaporitic sequence is deposited along shallow margins of the basin and a thinner sequence of evaporitic deposits accumulates in the deeper central portion of the basin. The asymmetry of the valley basin, specifically the relatively steep southern margin and the gentle rise to the north of the LHS deposits (Figure 4.29) would have resulted in accumulation of significant evaporitic shelf deposits

along the northern margin only. In this scenario, a sequence of LHS deposits similar to those that occur in the northeastern portion of the valley should have also formed along the northwestern margin. However, a thick sequence of LHS deposits is not observed in this area. It is possible that additional layers were deposited to the northwest and subsequently eroded. There is some evidence that the LHS deposits originally extended further to the north (section 4.5.4.1). Alternatively, the valley may have been episodically inundated with shallow brines that evaporated to leave layers cemented with hydrated sulfates that accumulated on the valley floor and near the northeastern margin, incrementally shallowing the basin or portions of the basin. In this scenario, it is possible, but not required, that the valley eventually filled with LHS deposits and the northeastern layers are late-stage deposits. If this was the case, then subsequent erosion stripped substantial deposits from the valley resulting in the current configuration of the deposits.

The proportion of chemical precipitants to siliciclastic material in the LHS deposits is undetermined. Input of siliciclastics may have been significant. Difference in albedo between layers in the LHS deposits could have resulted at least partially from variable contributions of low albedo basaltic fines and/or high albedo dust.

4.5.5 Implications of Additional Hydrated Sulfate Exposures

Exposures with hydrated sulfate spectral signatures are not restricted to LHS deposits. Multiple spatially limited hydrated sulfate exposures were detected in the study area in northern Sinus Meridiani, some of which are only evident in the highest spatial

resolution CRISM images (20 m/pixel FRTs). Hydrated sulfates were identified on both relatively low- and high- standing surfaces. Some of these hydrated sulfate exposures occur in topographic shadows or near the margins of mantled areas and appear to be erosional remnants of materials that were originally more extensive.

In addition to the exposures of hydrated sulfates discussed in section 4.5.4.1, hydrated sulfates were detected in two locations within low areas located 40 km to the northeast and 130 km to the north of the LHS deposits, respectively. These northern exposures of hydrated sulfates occur at similar elevations to upper layers of the LHS deposits and are consistent with deposition after substantial differential erosion of $ET1_A$, $ET1_B$, and $ET1_C$ occurred. It is possible that one or both of the northern exposures of hydrated sulfates are genetically related to the LHS deposits or formed during the same time period by similar processes but in different local environments.

Hydrated sulfates were also detected in limited locations on three high-standing surfaces of ET1 located to the southwest, south, and east of the LHS deposits, respectively. The relatively small spatial extent and/or poor quality of these exposures hinder stratigraphic analyses. All three of the hydrated sulfate exposures are constrained to postdate $ET1_B$. One exposure overlies $ET1_C$ and may pre- or post- date the formation of ET2 and another exposure overlies $ET1_D$.

The presence of multiple small exposures of hydrated sulfates separated by large expanses suggests that formation of deposits with hydrated sulfate spectral signatures was widespread. The stratigraphic context of these hydrated sulfate deposits is consistent with that of the LHS deposits and may record relatively late stage wetting events driven

by ground water.

4.5.6 Spectral and Textural Differences Between LHS Deposits and ET2

Although the bedrock component of Ph, ET2, is known to be sulfate rich based on in situ MER Opportunity rover investigations, NIR spectra of this unit do not exhibit distinct vibrational features associated with hydrated and/or hydroxylated phases (Figure 4.7, labeled '(7a) FRT000097F8_den Ph' and Figure 4.13, labeled '(13a) FRT000097F8_den Ph') [*Arvidson et al.,* 2006]. In contrast, spectra extracted from LHS deposits in the valley exhibit relatively strong vibrational features indicative of the presence of both mono- and poly- hydrated sulfates (Figure 4.21). Gray crystalline hematite was detected in orbital IR spectra of Ph but not of the LHS deposits [*Christensen et al*., 2001]. Analysis made by the Opportunity rover along its traverse revealed that ET2 is chemically homogenous [*Rieder et.al*, 2004]. In contrast, compositional layering that likely records fluctuations in brine concentration and/or composition is observed in LHS deposits.

The erosional texture of the LHS deposits is variable, but groves and pits are typically present at intermediate spatial scales (Figure 4.19c). In contrast, ET2 is relatively smooth at a similar spatial scale (Figure 4.11f). ET2 is extensively covered by a mantle (Pm) that armors the surface and slows deflation [*Sullivan et al*., 2005]. Coatings on ET2 were identified in Opportunity rover observations [*Knoll et al.,* 2008]. Extensive coatings and/or alteration/dehydration rinds present at the surface of ET2 could obscure the spectral signature of underlying hydroxylated and/or hydrated sulfate

minerals in orbital NIR reflectance spectra. In contrast, there is geomorphic evidence that LHS deposits are easily erodible. The timescale of erosion may be shorter than that of coating formation for the LHS deposits.

4.5.7 Scale of Evaporitic Setting and Comparison to Other Deposits on Mars

The largest exposure of gray crystalline hematite detected on Mars occurs in Meridiani Planum [*Christensen et al*., 2001]. Smaller exposures of gray hematite were detected within Aram Chaos and in association with some interior layered deposits (ILDs) in Valles Marineris [*Christensen et al*., 2001]. Crater counts indicate that the Meridiani Planum hematite-bearing unit formed in the late Noachian to Early Hesperian [*Arvidson et al*., 2006], but that the Aram Chaos hematite-bearing deposits formed later in Martian history, during the Late Hesperian period [*Rotto and Tanaka*, 1995; *Glotch et al*., 2005]. The Valles Marineris ILDs are also inferred as Hesperian in age [*Scott and Tanaka*, 1986].

Hydrologic modeling predicts that ground water upwelling occurred in Sinus Meridiani, Aram Chaos, and Valles Marineris during the late Noachian and the Hesperian [*Andrews-Hanna et al.*, 2007; 2008]. Modeled ground water upwelling is driven by topographic gradient and is not confined to closed basins.

Hydrated sulfate detections in Aram Chaos occur near exposures containing gray crystalline hematite [*Gendrin et al*., 2005; *Glotch et al*., 2005; *Noe Dobrea*, 2008]. Gray hematite deposits detected in Valles Marineris typically occur near the base of ILDs

[*Christensen et al*., 2001]. Both monohydrated and polyhydrated sulfates also occur in some ILDs [*Mangold et al*., 2008; *Bishop et al.,* 2009; *Murchie et al*., 2009b].

4.5.8 Fe/Mg Phyllosilicate-bearing Deposits

4.5.8.1 Implications

Fe/Mg smectites are detected in limited exposures associated with the oldest unit (CT) in the study area and on surfaces of $ET1_C$, a sedimentary unit that predates the formation of ET2, the sulfate and hematite-bearing unit explored by the Opportunity rover (Figure 4.4b). The presence of Fe/Mg smectites on the surface of $ET1_C$ indicates that this unit formed in a geochemical environment that differed from that of ET2. The low pH conditions experienced by ET2 are probably not representative of the conditions that prevailed during the formation of ET1. The detection of phyllosilicate-bearing deposits in association with the oldest terrains in northern Sinus Meridiani is consistent with the hypothesis that phyllosilicates formed within the oldest terrains on Mars and that geochemical conditions became less favorable to phyllosilicate formation in later periods [*Bibring et al.,* 2006].

4.5.8.2 Spectral Comparisons

The phyllosilicate-bearing deposits associated with CT are characterized spectrally by bands at 1.91 and 2.30 to 2.31 μm, consistent with the presence Mg-rich

smectites (Figure 4.2 and Figure 4.7). The ~2.3 μm band is relatively deeper than the ~1.9 μm feature in these deposits and chlorite may also contribute to the spectral signature. A similar spectral shape occurs within Fe/Mg phyllosilicate-bearing deposits detected to the south of our study area and within Miyamoto crater [*Wiseman et al*., 2009].

Phyllosilicate-bearing deposits in $ET1_C$ exhibit shallow bands at 1.92 and 2.30 to 2.31 μm, consistent with the presence of Fe/Mg smectite (Figure 4.2 and Figure 4.7). The ~1.9 μm feature is relatively stronger than the 2.31 μm band in spectra of $ET1_C$. Phyllosilicates exposed in ET1 to the east of our study area also exhibit a relatively strong ~1.9 μm feature [*Poulet et al*., 2008]. The fact the phyllosilicate-bearing materials associated with $ET1_C$ have slightly different spectral shapes than older phyllosilicate-bearing deposits in Sinus Meridiani may be significant. However, several factors, including the composition [e.g., *Calvin and King*, 1997], the degree of crystallinity, the amount of hydration and/or absorbed water in a sample [*Milliken et al.*, 2005], or the presence of coatings [*Cooper and Mustard,* 1999], can contribute to the strength of the ~1.9 μm band. In addition, the abundance of the phyllosilicates influences band strengths and mixing with additional hydrated phases can affect the relative strengths of the ~1.9 and 2.3 μm bands.

4.6 Conclusion

Sedimentary deposits indicative of an aqueous history that evolved over time are preserved in Sinus Meridiani. Laterally continuous strata were mapped over 100s of

kilometers in extensive indurated sedimentary deposits (ET1) that predate the formation of the sulfate and hematite-bearing unit (Ph) explored by the MER rover Opportunity. A thick sequence (~150 m thick is some locations) of layered mono- and poly- hydrated sulfate (LHS) deposits that are texturally and spectrally distinct from the sulfate and hematite rich unit (Ph) explored by the Opportunity rover were unconformably deposited following the partial erosion of older sedimentary units ($ET1_A$, $ET1_B$, $ET1_C$). These hydrated sulfate deposits may postdate the formation of Ph and, if so, indicate a relatively late-stage wetting event. The presence of Fe/Mg smectites in older sedimentary deposits ($ET1_C$) indicates that the low pH formation conditions inferred for the younger sulfate and hematite-bearing unit (Ph) are not representative of the aqueous geochemical environment that prevailed during the formation of earlier materials (CT and ET1).

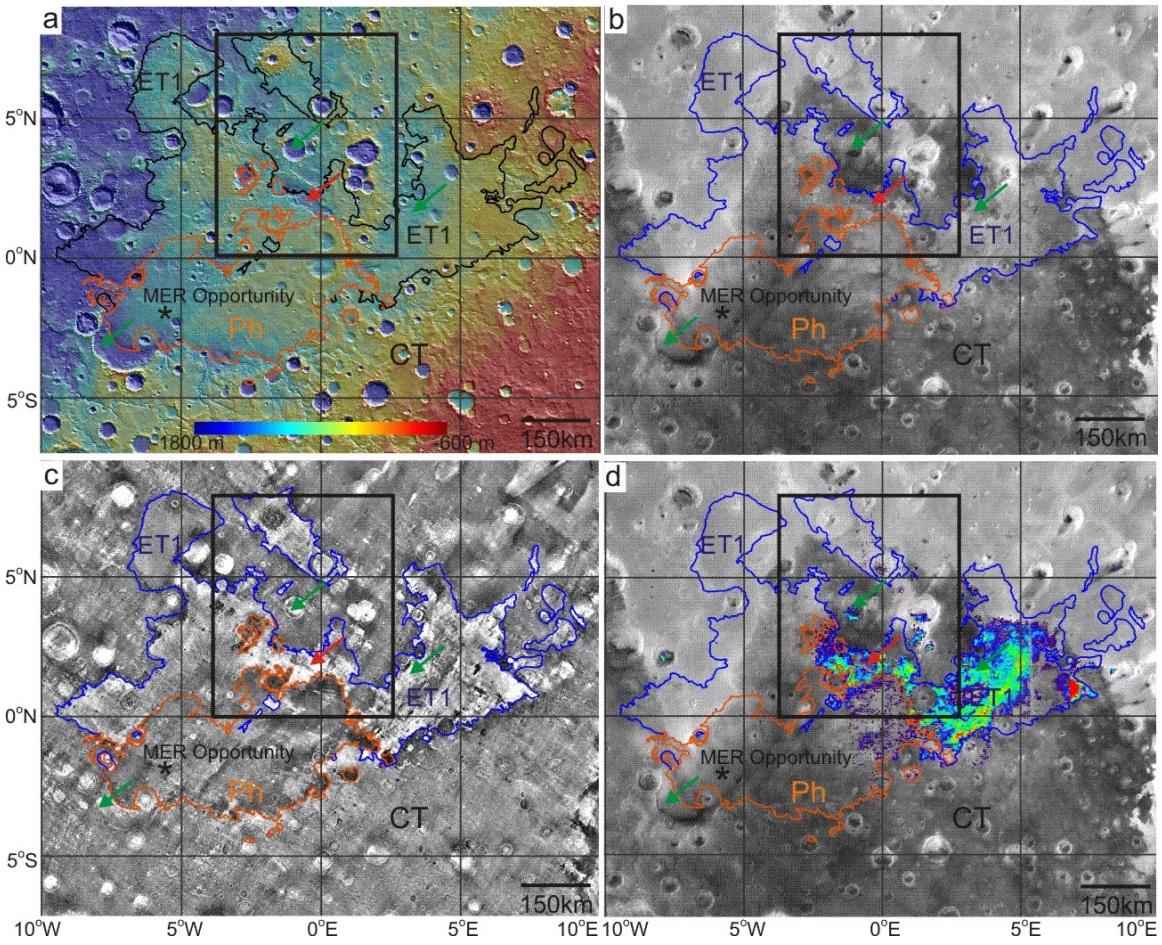
a
b
c
d
ET1
ET1
MER Opportunity
Ph
CT
1800 m
600 m
150km
5°N
0°N
5°S
10°W
5°W
0°E
5°E
10°E

Figure 4.1. Regional context map showing main units exposed in Sinus Meridiani with unit outlines overlain on multiple basemap mosaics. Oldest materials exposed are mapped as *Cratered Terrain* (CT). Indurated sedimentary rock, *Etched Terrain 1* (ET1), unconformably overlies CT. *Plains, Hematite-bearing* (Ph) is the stratigraphically youngest mapped unit. Ph is a composite unit that consists of indurated sedimentary rock, *Etched Terrain 2* (ET2), overlain by an unconsolidated veneer, the *Plans Mantle, Hematite-bearing* (Pm). The MER Opportunity rover landing site on Ph is indicated with an asterisk. The black box outlines the area shown in Figure 4.3. Green arrows indicate the locations of previously identified Fe/Mg phyllosilicate-bearing materials [*Poulet et al*., 2005; *Poulet et al*., 2008; *Wiseman et al*., 2009] and red arrows indicate previously identified hydrated sulfate deposits [*Gendrin et al*., 2005; *Griffes et al*., 2007]. Early Hesperian volcanic ridged plains cover a small portion of CT in western Sinus Meridiani near 1° S, 9° W [*Scott and Tanaka*, 1986]. Intracrater deposits within craters in CT that may be relatively younger are not distinguished in this regional context map. a) MOLA color coded elevations overlain on a MOLA hill shade mosaic. b) MOC WA mosaic c) THEMIS NIR mosaic. d) OMEGA 1.9 μm parameter map overlain on a MOC WA mosaic.

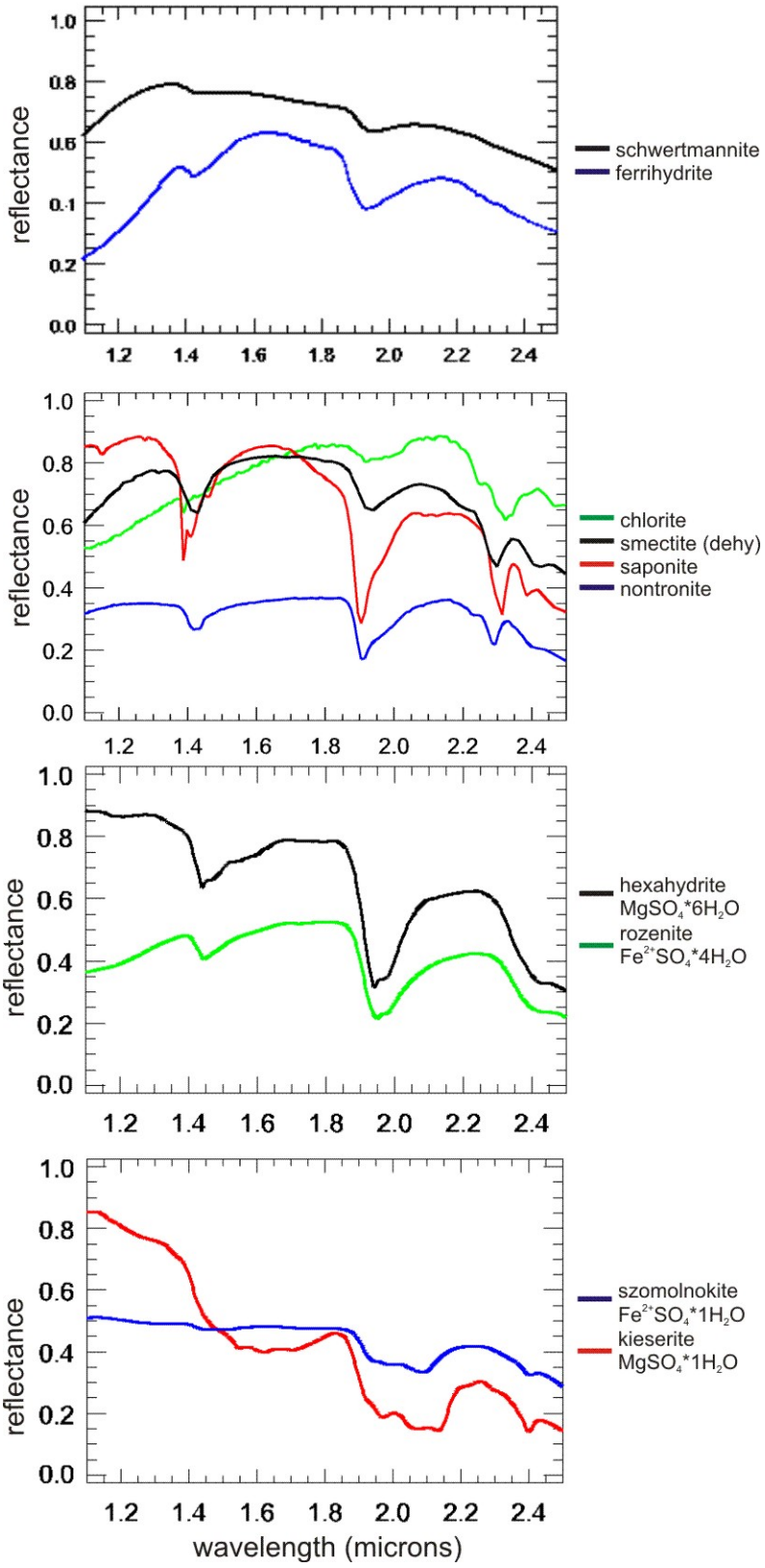
reflectance
schwertmannite
ferrihydrite
chlorite
smectite (dehy)
saponite
nontronite
hexahydrite
MgSO4*6H2O
rozenite
Fe2+SO4*4H2O
szomolnokite
Fe2+SO4*1H2O
kieserite
MgSO4*1H2O
wavelength (microns)

Figure 4.2. Laboratory reflectance spectra of selected terrestrial samples that include a) hydrated minerals that exhibit an indistinct spectral drop-off longward of ~2.2μm, b) Fe, Mg, and Fe/Mg phyllosilicates, c) Fe and Mg monohydrated sulfates, d) and polyhydrated sulfates. Ideal mineral formulas are included for reference in part c). Chemical analyses for most samples are available in supplementary data associated with the spectral libraries from which the laboratory spectra plotted in were derived [*Clark et al.,* 2007; *CRISM Science Team*, 2006; *Cloutis et* al., 2006].

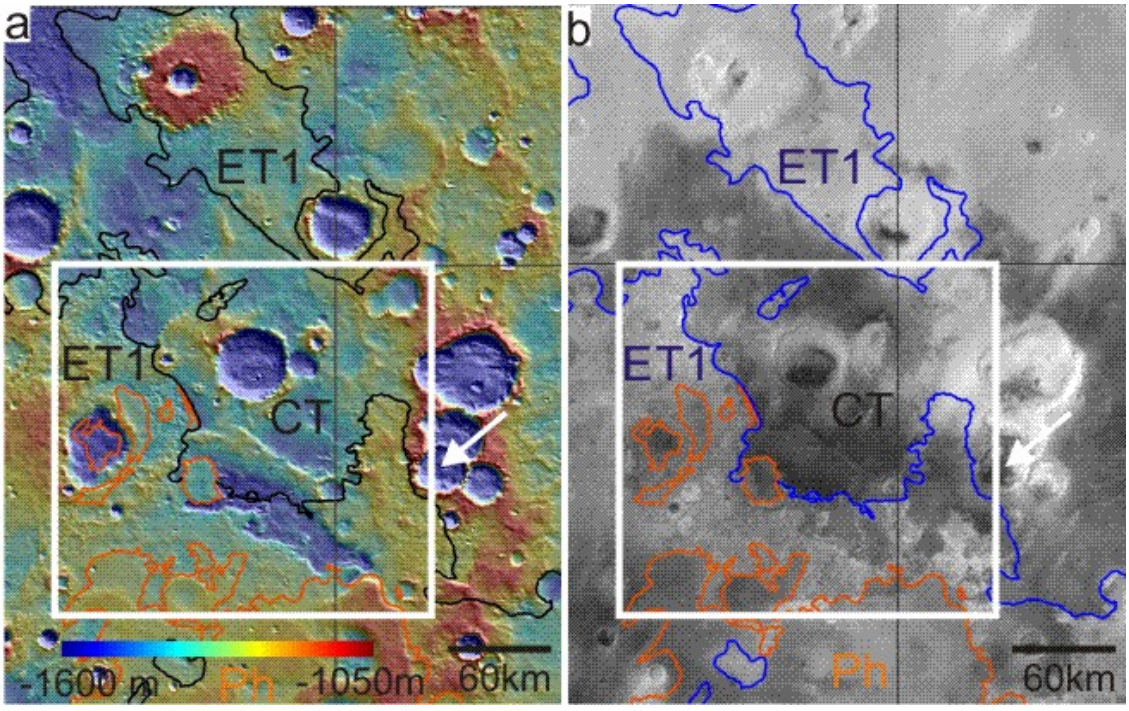

Figure 4.3. Context maps showing the area of northern Meridiani indicated with a black box in Figure 4.1. Previous identified phyllosilicate-bearing deposits [*Poulet et al*., 2005; *Poulet et al*., 2008; *Wiseman et al*., 2009] and hydrated sulfate deposits [*Gendrin et al*., 2005; *Griffes et al*., 2007] are indicated with green and red arrows, respectively. Oldest materials exposed are mapped as *Cratered Terrain* (CT). Indurated sedimentary rock, *Etched Terrain 1* (ET1), unconformably overlies CT. *Plains, Hematite-bearing* (Ph) is the stratigraphically youngest mapped unit and is a composite unit that consists of indurated sedimentary rock, *Etched Terrain 2* (ET2), overlain by an unconsolidated veneer, the *Plans Mantle, Hematite-bearing* (Pm). The location of the study area is shown with a white outline. The location of a 30 km diameter crater is indicated with a white arrow. a) MOLA color coded elevations overlain on a MOLA hill shade mosaic. b) MOC WA mosaic.

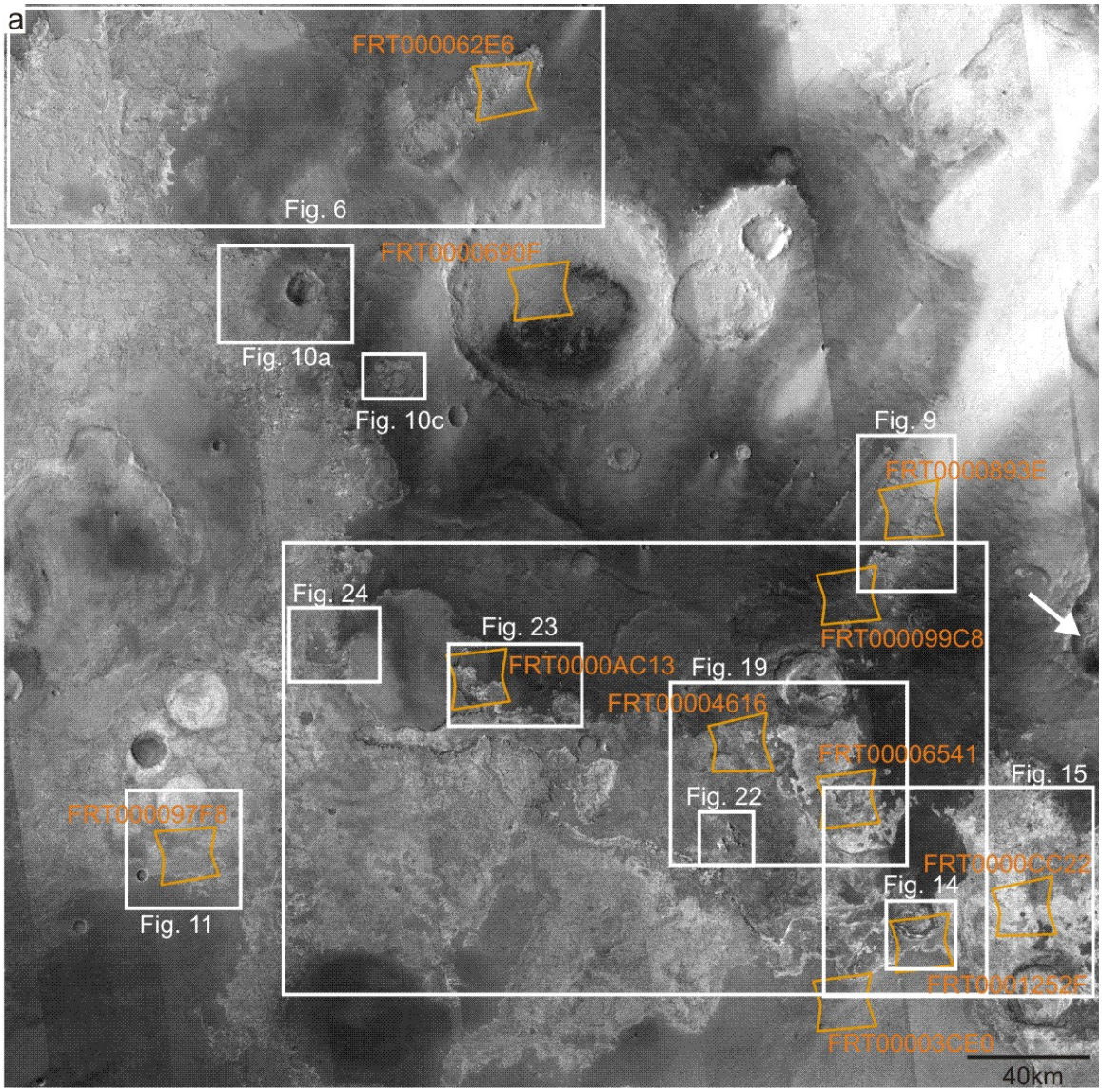
a
FRT000062E6
Fig. 6
FRT0000690F
Fig. 10a
Fig. 10c
Fig. 9
FRT0000893E
Fig. 24
Fig. 23
FRT0000AC13
Fig. 19
FRT00004616
FRT000099C8
FRT00006541
Fig. 15
Fig. 22
FRT000097C8
Fig. 11
FRT0000CC22
Fig. 14
FRT00001252F
FRT00003CE0
40km

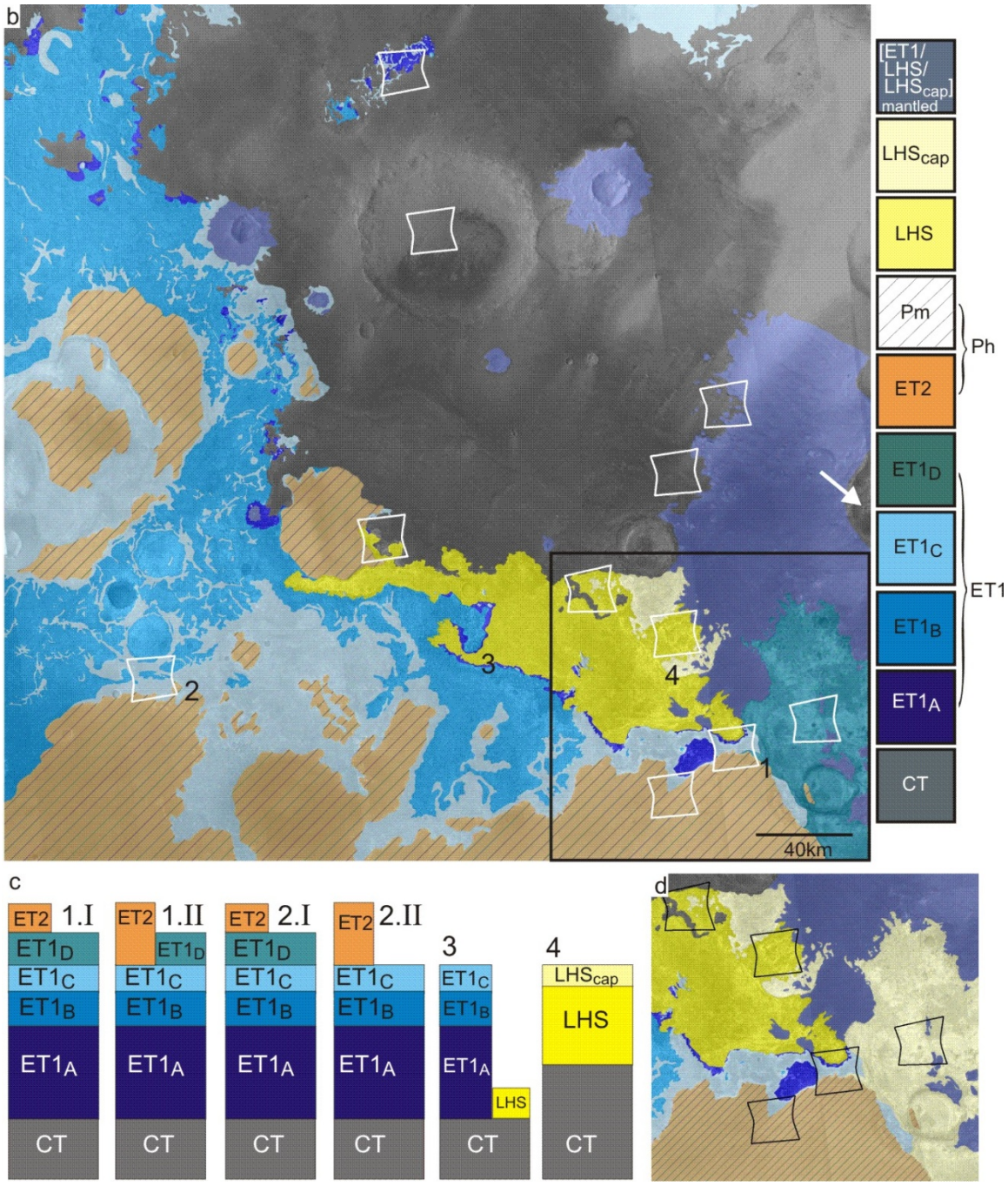
b
[ET1/ LHS/ LHScap] mantled
LHScap
LHS
Pm
Ph
ET2
ET1D
ET1C
ET1
ET1B
ET1A
CT
1
2
3
4
40km
c
ET2 1.I
ET2 1.II
ET2 2.I
ET2 2.II
3
4
ET1D
ET1C
ET1B
ET1A
LHS
LHScap
CT
d

Figure 4.4. a) CTX mosaic of the study area in northern Meridiani indicated with a white box on the context maps shown in Figure 4.3. Locations of figures and CRISM FRT observations shown in subsequent figures are indicated with white and yellow outlines, respectively. b) CTX mosaic shown in part a) with detailed units map overlain. Intracrater deposits within *Cratered Terrain* (CT) may be younger than CT, but are not distinguished in this map for simplicity. *Etched Terrain* (ET1) is subdivided into $ET1_A$, $ET1_B$, $ET1_C$, and $ET1_D$. *Layered Hydrated Sulfate* (LHS) deposits and the Layered Hydrated Sulfate Cap (LHS_{cap}) are mapped separately from ET1. Mantled areas of ET1, LHS and the LHS_{cap} are classified as $[ET1/LHS/LHS_{cap}]_{mantled}$. The bedrock and mantle component of the *Plains, Hematite-bearing* (PH) are mapped as *Etched Terrain 2* (ET2) and the *Mantle, Hematite-bearing* (Pm), respectively. c) Stylized vertical cross sections showing units at locations 1, 2, 3, and 4 labeled in part b). I and II represent two different possibilities that are consistent with the map shown in part b). Contact types between units are not indicated in these stylized vertical cross sections. d) left: Alternate portion of the map shown in part b) in which LHS_{cap} and $ET1_D$ are laterally continuous.

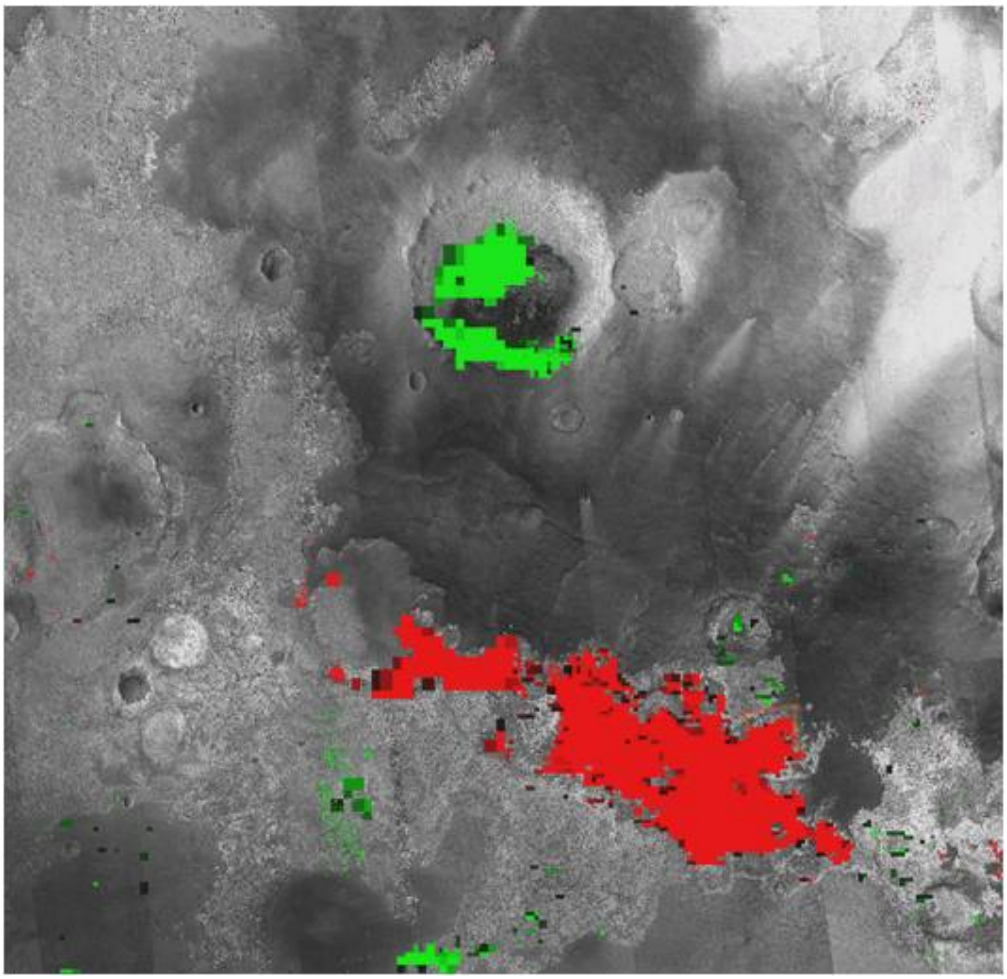

Figure 4.5. CTX mosaic shown in Figure 4.4a with CRISM and OMEGA parameters maps overlain. Red areas exhibit spectral features near 2.4 μm plus ~1.9 μm or 2.4 μm plus ~2.1 μm, consistent with the presence hydrated sulfates. Green areas exhibit a feature near 2.3 μm that is typically caused by Fe/Mg-OH vibrations in Fe/Mg phyllosilicates. Threshold values for D1900, D2100, D2300, and D2400 parameter maps are listed in Table 4.1.

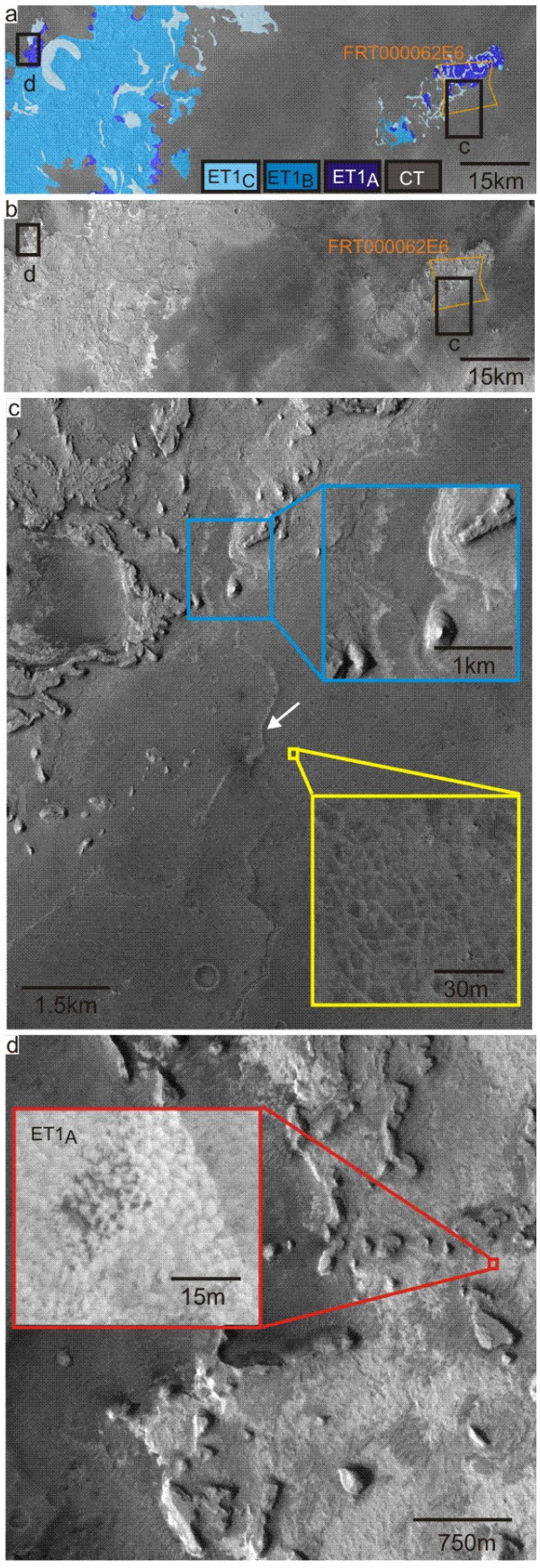
a
d
FRT000062E6
c
ET1C
ET1B
ET1A
CT
15km
b
d
FRT000062E6
c
15km
c
1km
1.5km
30m
d
ET1A
15m
750m

Figure 4.6. a) Subset of units map, location indicated in Figure 4.4. b) Subset of CTX mosaic covering the same area as shown in part a). c) Higher resolution view of the white box labled 'c' in part b) P03_002390_1840_XI_04N001W_070129. The part of the channel feature indicated with a white arrow is inverted, or has positive relief. The yellow inset shows an area in CT that exhibits polygonal fracturing (HiRISE PSP_004091_1845_RED). Layers of $ET1_A$, $ET1_B$, and $ET1_C$ are visible in mesa walls in the cyan inset. d) Higher resolution view of the white box labeled 'd' in part b) (P06_003379_1827_XN_02N002W_070416). Mesas that consists of $ET1_A$, $ET1_B$, and $ET1_C$ are located near the edge of a large, continuous expanse of ET1. A subset of HiRISE PSP_003946_1850 that shows the distinctive scallop texture of $ET1_A$ is inset in red.

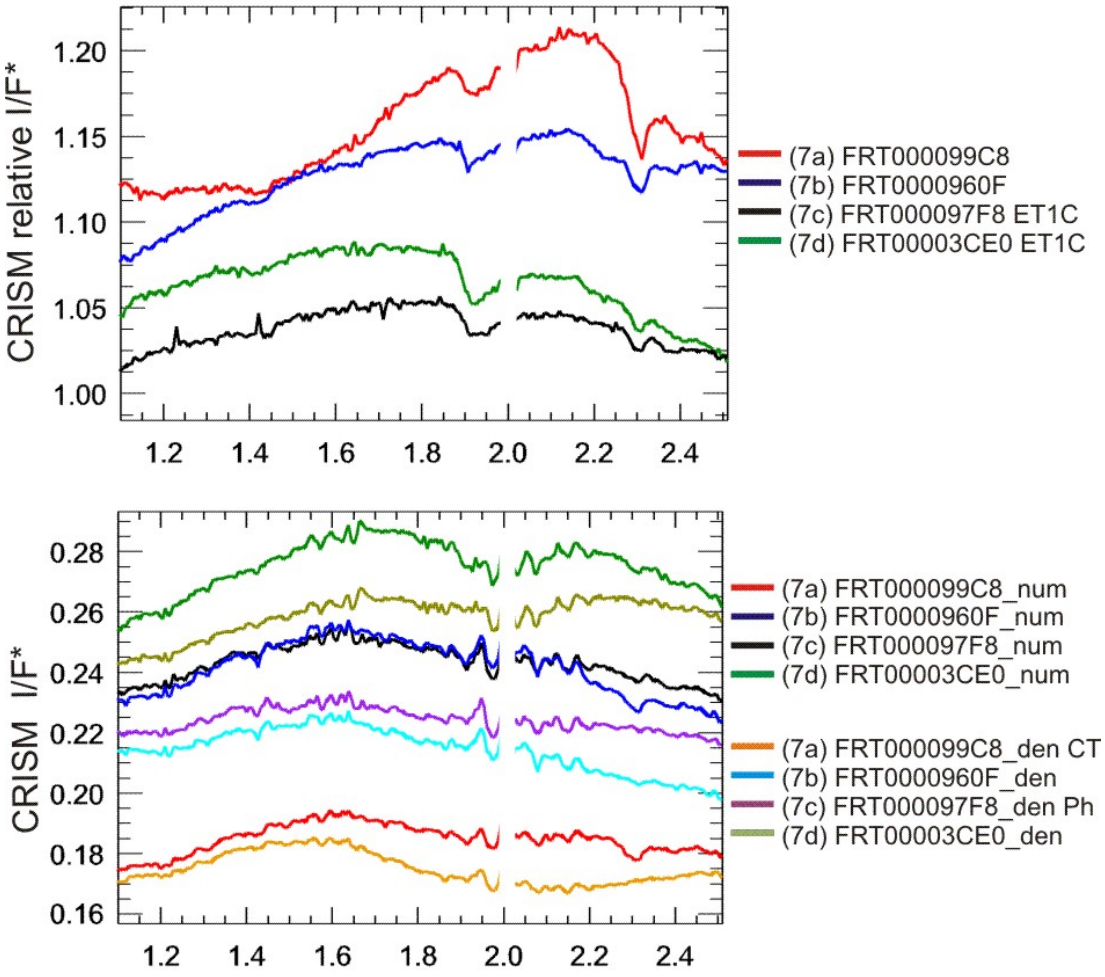

Figure 4.7. Upper: CRISM relative reflectance spectra from areas of selected FRTs with phyllosilicate like spectral signatures. Lower: CRISM I/F* (cos(i) and volcano scan corrected) numerator and denominator spectra that were used to generate the ratio spectra shown in the upper plot. Spectra are averages of 25 spectra.

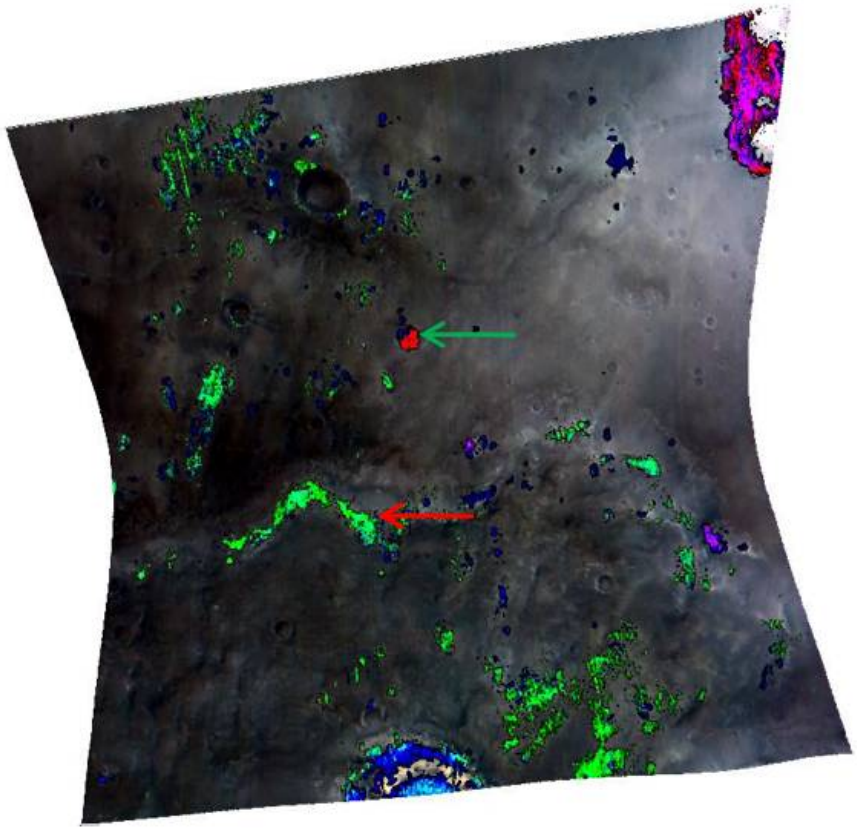

Figure 4.8. a) False color composite of CRISM image FRT000099C8 (R = 2.5 μm, G = 1.5 μm, B = 1.1 μm) with parameter map color composite overlain (R = D2400, G = D2300, and B = D1900). Blue areas exhibit high D1900 parameter values, red areas exhibit high D2400 parameter values, green areas exhibit high D2300 parameter values, magenta areas exhibit high D1900 plus D2400 values, and cyan areas exhibit high D1900 plus D2300 values. Spectra extracted from the areas indicated with the red and green arrows are shown in Figure 4.7 and Figure 4.26, respectively.

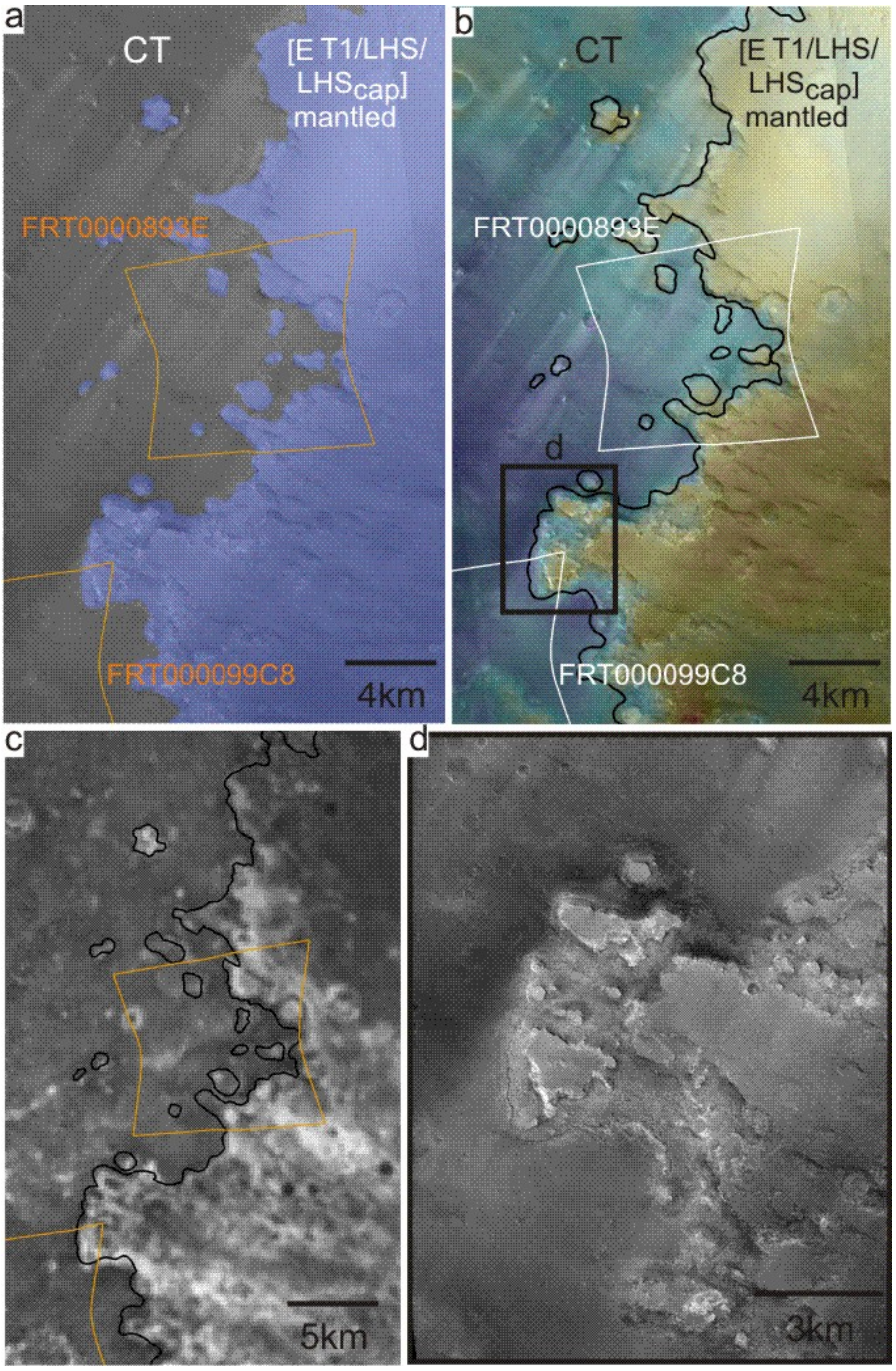
a
CT
[E T1/LHS/
LHS$_{cap}$]
mantled
FRT0000893E
FRT000099C8
4km
b
CT
[E T1/LHS/
LHS$_{cap}$]
mantled
FRT0000893E
d
FRT000099C8
4km
c
5km
d
3km

Figure 4.9. a) Subset of units map shown in Figure 4.4b. Footprints of CRISM images FRT000099C8 (shown in Figure 4.8) and FRT0000893E (shown in Figure 4.25) are overlain in white. This area of $[ET1/LHS/LHS_{cap}]_{mantled}$ is ~3 crater radii from the center of the 30 km impact crater indicated with a white arrow in Figure 4.4 and stands up to ~200 m above the surface of CT. At a distance of three crater radii, initial ejecta deposition of < 10 m thick is expected [*McGretchin* 1974, *Garvin and Frawley*, 1998]. b) CTX mosaic of area shown in part a) with MOLA color coded topography overlain. c) THEMIS NIR mosaic of area shown in part a). Relatively high thermal inertia areas appear bright. d) Zoom in of red box shown in part b) (CTX P13_005937_1834_XI_03N359W_071102) showing light toned material exposed at margins of $[ET1/LHS/LHS_{cap}]_{mantled}$.

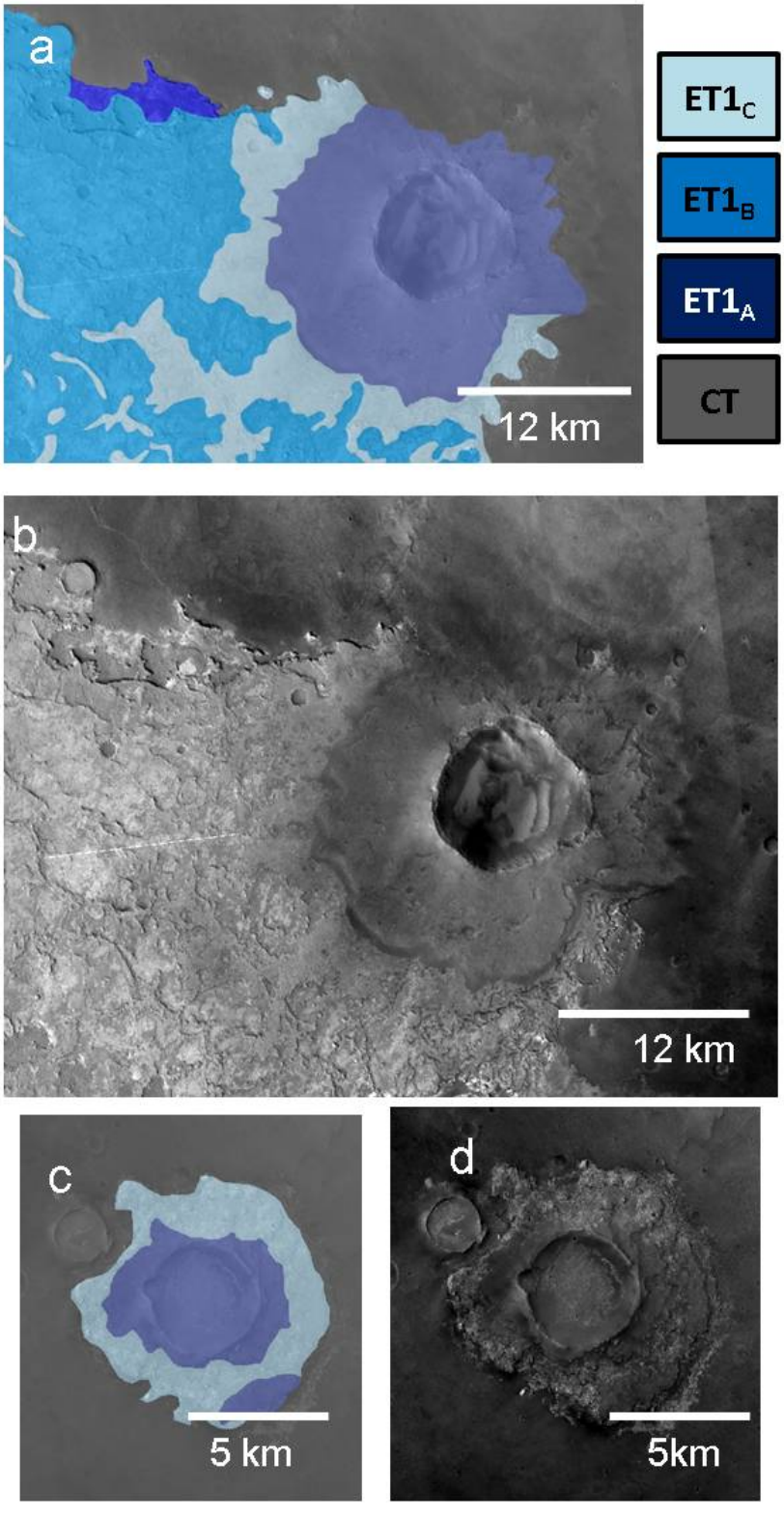
a
12 km
ET1C
ET1B
ET1A
CT
b
12 km
c
5 km
d
5km

Figure 4.10. Dark material that appears to have originated as crater ejecta mantles higher albedo ET1. a) Subset of units map, location shown in Figure 4.4. b) CTX mosaic of area shown in part a). c) Subset of units map, location shown in Figure 4.4. d) CTX P03_002179_1855_XI_05N001W_070113 subset, same as part c).

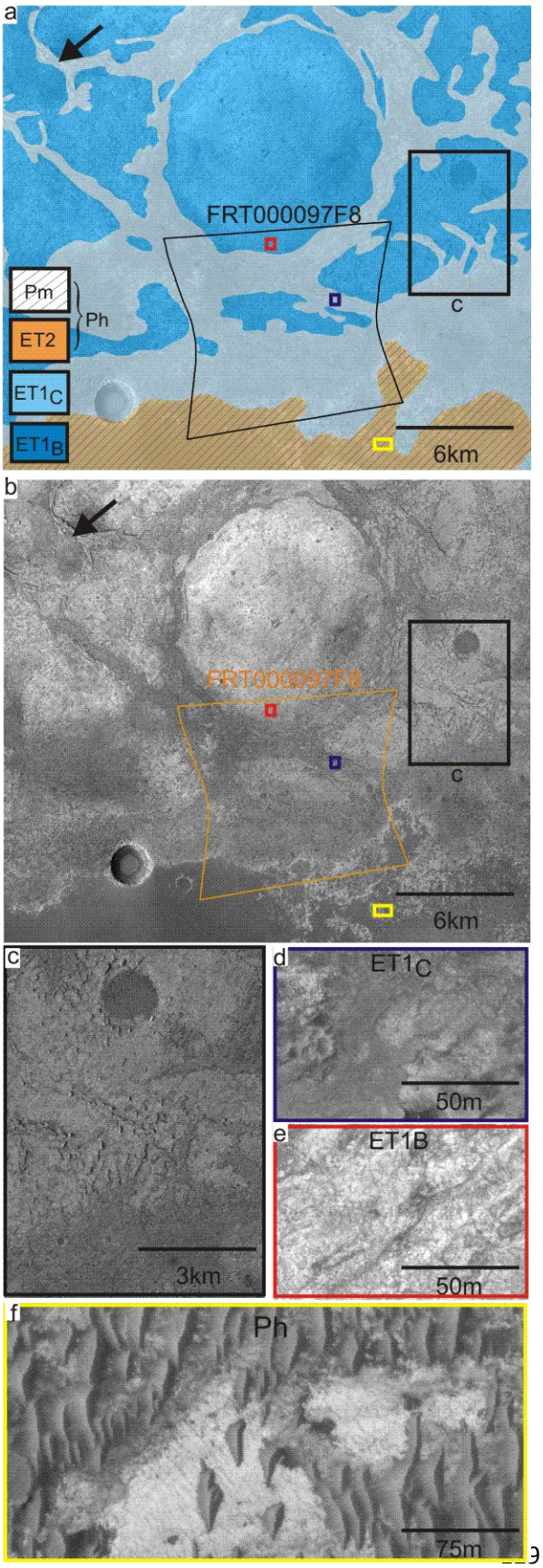
a
FRT000097F8
Pm
Ph
ET2
ET1C
ET1B
c
6km
b
FRT000097F8
c
6km
c
3km
d
ET1C
50m
e
ET1B
50m
f
Ph
75m

Figure 4.11. a) Units map of a subregion indicated in Figure 4.4a. The footprint for CRISM image FRT000097F8 is outlined. A low ridge is indicated with a black arrow. b) CTX mosaic of part a). c) Blow up of box labeld 'c' in part a). A knobby portion of the knob and ridge-bearing $ET1_C$ transitions to a more continuous layer (CTX image P04_002746_1808_XI_00N002W_070226). $ET1_B$ is visible below knobs. d) HiRISE PSP_007572_1820_RED subset showing the small scale morphology of $ET1_C$. e) HiRISE PSP_007572_1820_RED subset showing small scale morphology of $ET1_B$. f) HiRISE PSP_007572_1820_RED subset showing ET2.

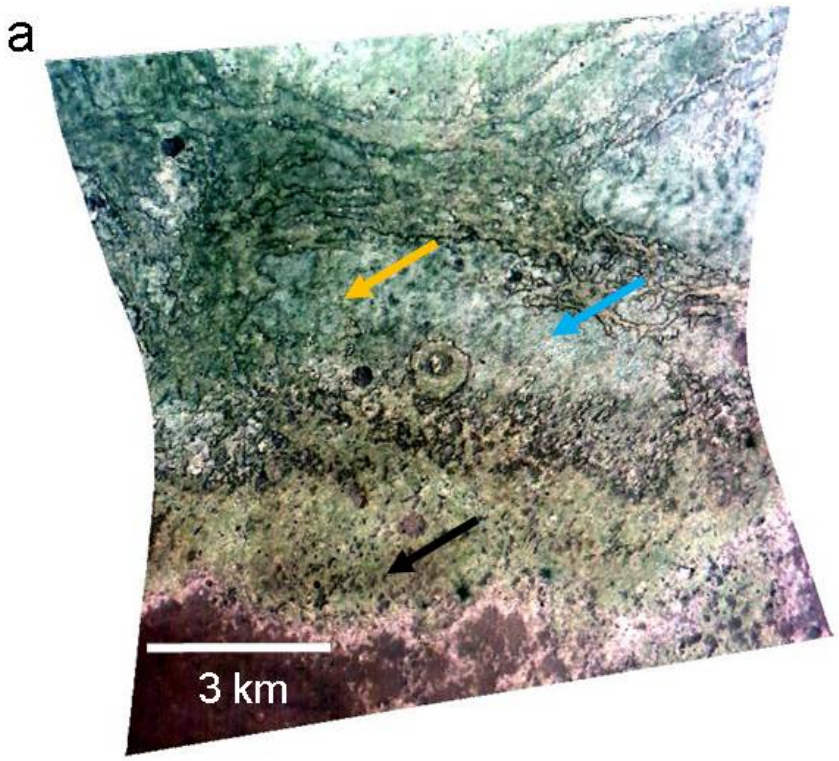
a
3 km

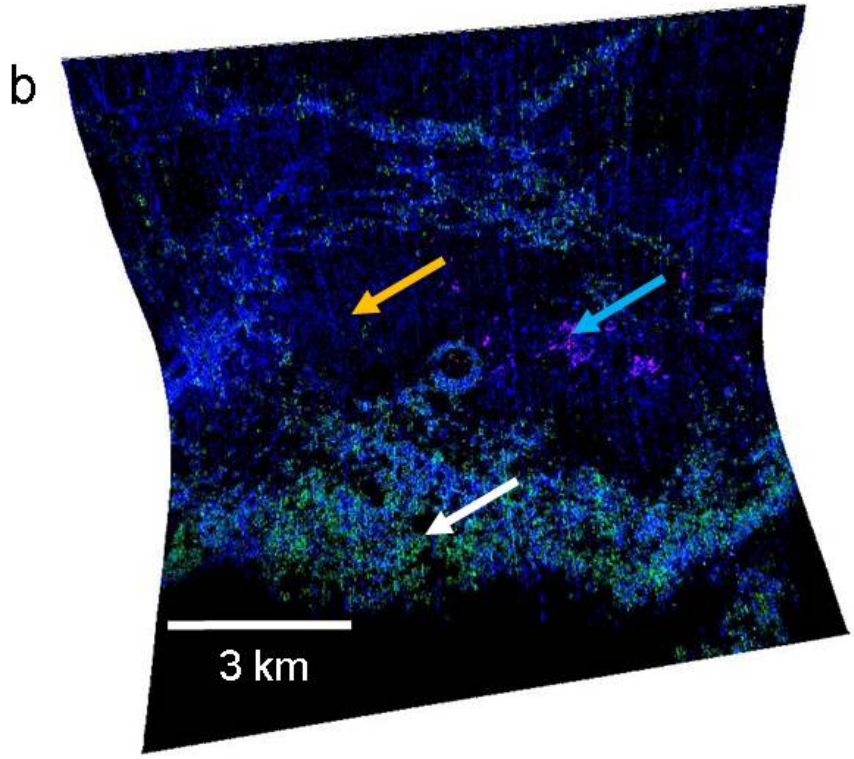
b
3 km

Figure 4.12. a) CRISM image FRT000097F8 (footprint shown in Figure 4.11) mainly covering $ET1_C$ and ET1B with Ph is exposed in the southwestern portion of the image. Black/white, cyan, and blue arrows indicate locations of spectra extracted from $ET1_C$, $ET1_B$, and a spectrally anomalous area, respectively, that are shown in Figure 4.7, Figure 4.13, and Figure 4.26, respectively. a) False color composite with R =2 .5 μm, G = 1.5 μm, B = 1.1 μm. b) Parameter map color composite of FRT000097F8 in which R = D2400, G = D2300, and B = D1900. Areas that appear blue have high D1900 parameter values, areas that appear green have relatively high D2300 values, and areas that appear magenta exhibit high D1900 plus D2400 parameter values.

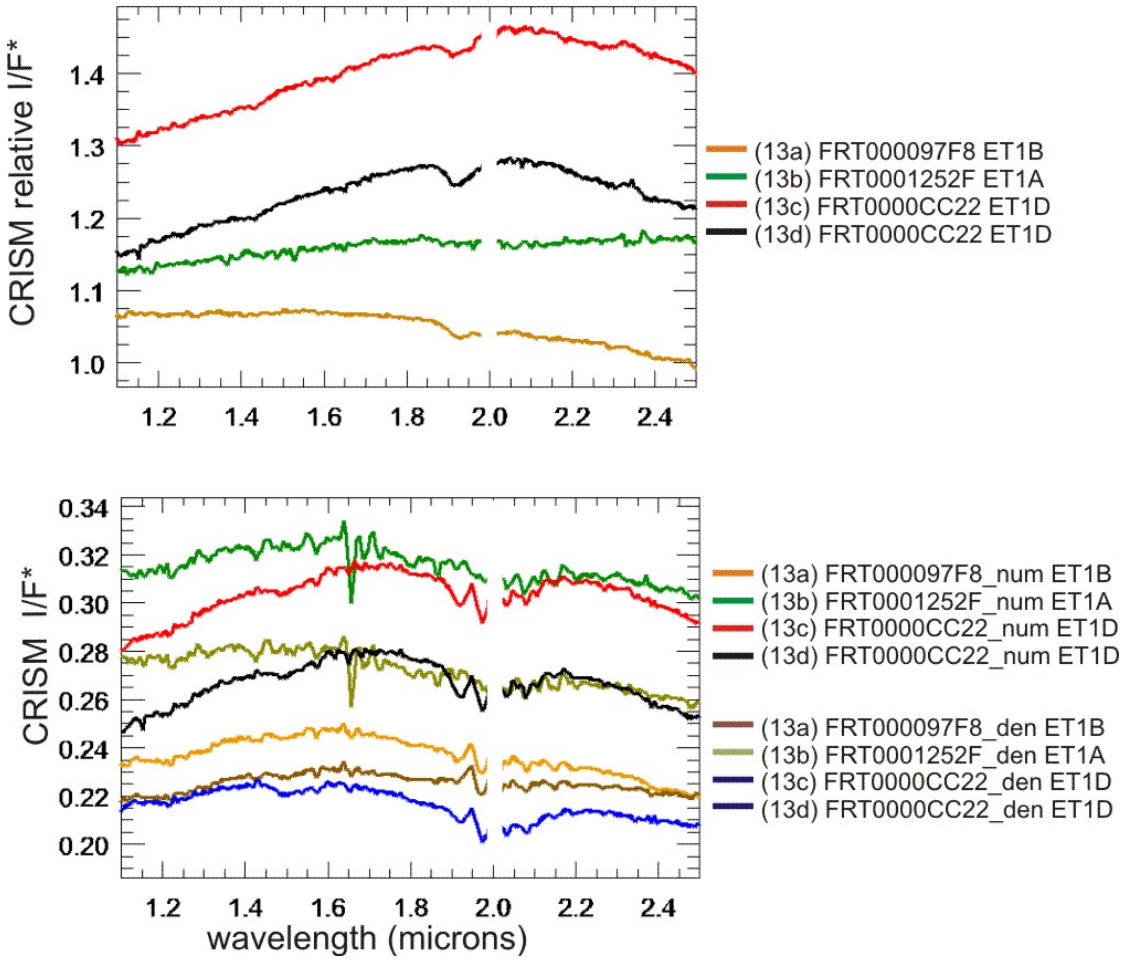

Figure 4.13. Upper: CRISM relative reflectance spectra from areas of selected FRTs with hydration features at 1.9 μm but that lack additional diagnostic vibrational features at longer wavelengths. Lower: CRISM I/F* (cos(i) and volcano scan corrected) numerator and denominator spectra that were used to generate the ratio spectra shown in the upper plot. Spectra are averages of 25 spectra.

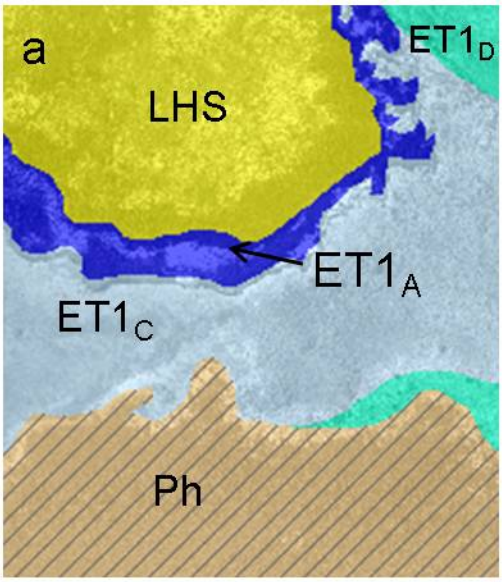
a
LHS
ET1D
ET1A
ET1C
Ph

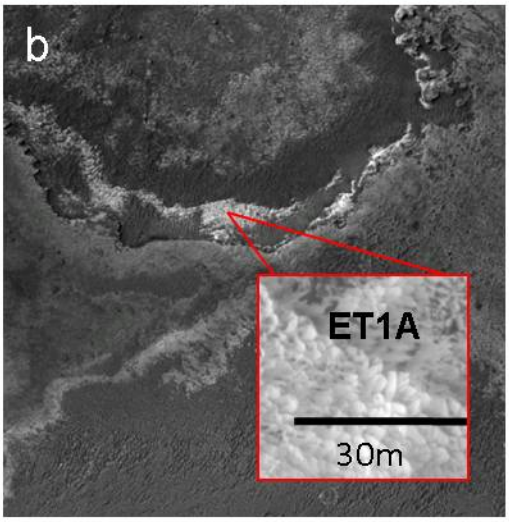
b
ET1A
30m

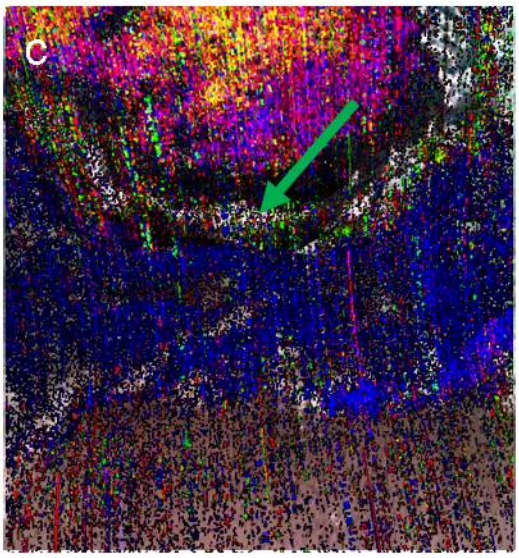
c

Figure 4.14. a) Subset of units map, location indicated in Figure 4.4. b) CTX subset (T01_000820_1816_XN_01N359W_060929l), same area as part a). The red inset shows the distinctive scallop texture of $ET1_A$ exposed in the cliff wall (HiRISE image PSP_001493_1815_RED.LBL). Scalloped textured terrain that has a broadly similar morphology to this but occurs in low thermal intertia areas was analyzed by Bridges et al. [2009]. c) Subset CRISM image FRT0001252F (footprint shown in Figure 4.4) covering part a). False color composite (R = 2.5 μm, G = 1.5 μm, B = 1.1 μm) with parameter map color composite (R = D2400, G = D2100, and B = D1900). Areas that appear magenta exhibit high D1900 and D2400 parameter values, consistent with the presence of presence of polyhydrated sulfates and areas that appear yellow have high D2100 and D2400 values, consistent with the present of monohydrated sulfates. Green arrow indicates location of spectrum extracted from $ET1_A$, shown in Figure 4.13.

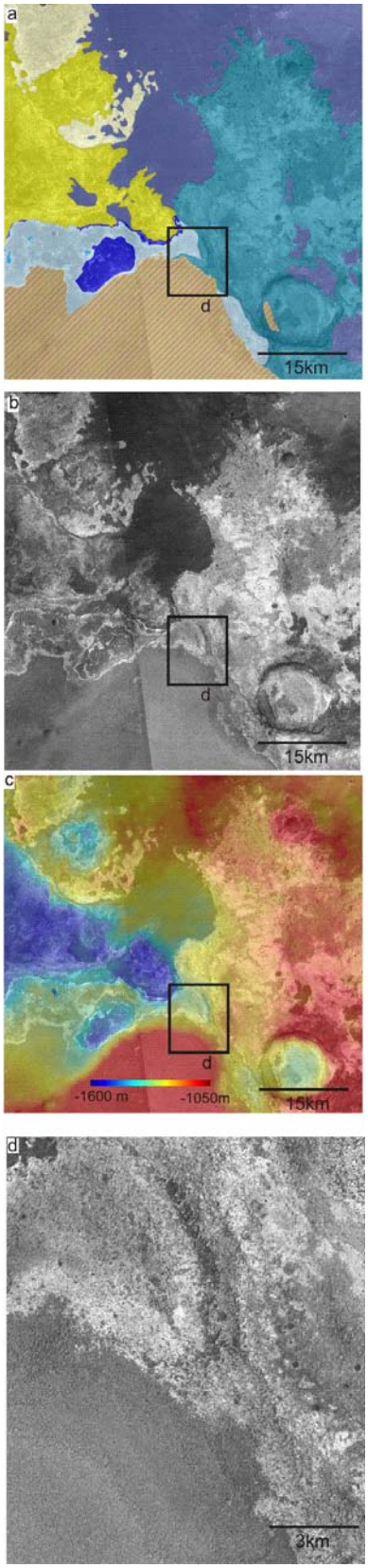
a
d
15km
b
d
15km
c
d
-1600 m
-1050m
15km
d
3km

Figure 4.15. a) Units map, location show in Figure 4.4. Contact between $ET1_C$ and $ET1_D$ occurs. $ET1_D$ and LHS_{cap} obscured by intervening $[ET1/LHS/LHS_{cap}]_{mantled}$, makes it difficult to interpret stratigraphic relationship. b) CTX mosaic same area as part a). c) CTX mosaic show in part b), but with MOLA color coded topography overlain. d) Blow up showing layers in $ET1_D$.

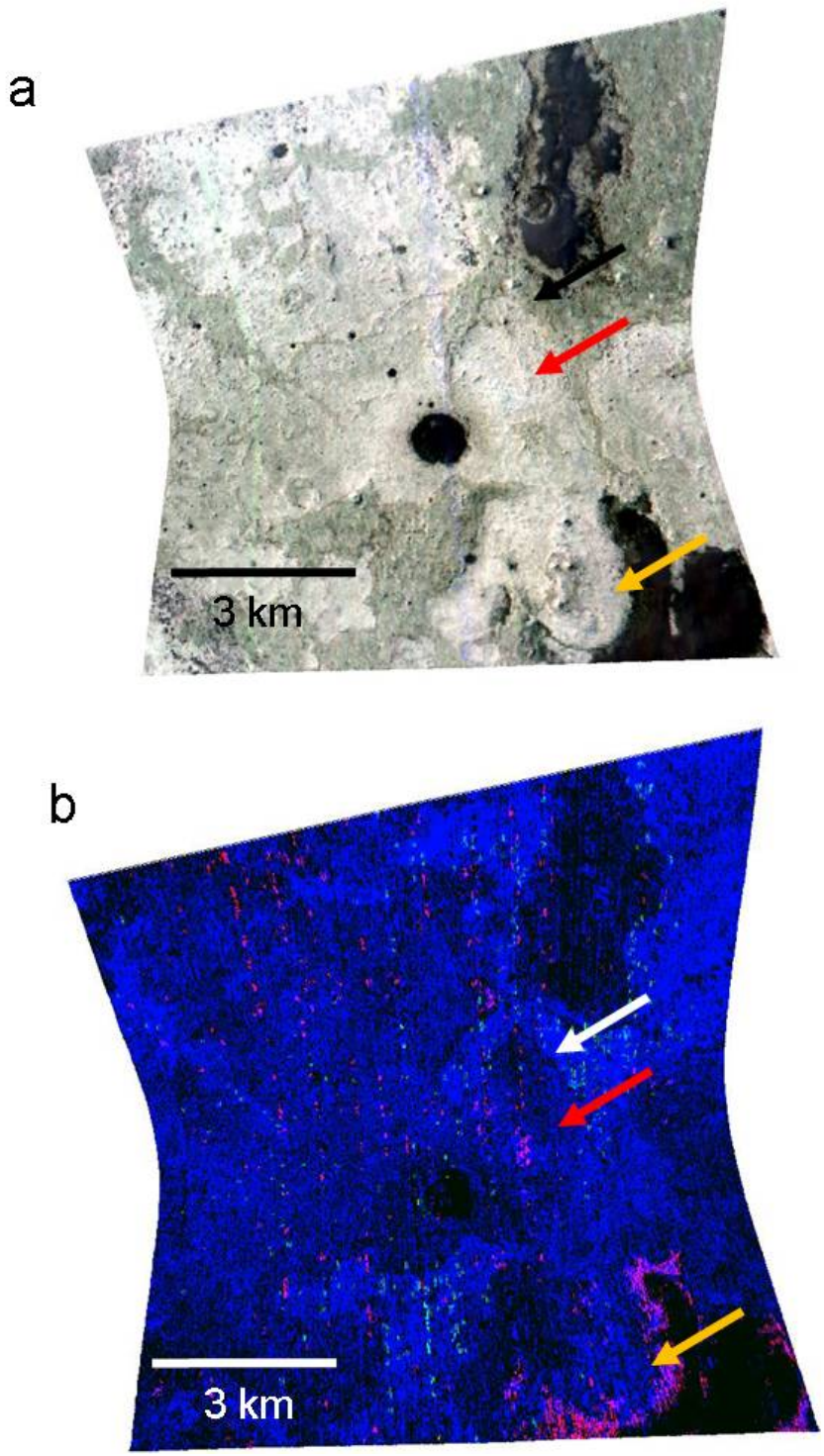
a
3 km
b
3 km

Figure 4.16. a) CRISM image FRT0000CC22 mainly covering $ET1_D$ (footprint shown in Figure 4.15). Black/white and red arrows indicate locations of spectra extracted from $ET1_D$ shown in Figure 4.13. Yellow arrow indicates spectrally anomalous area, spectrum shown in Figure 4.26. a) False color composite of FRT0000CC22 with R =2 .5 μm, G = 1.5 μm, B = 1.1 μm. b) Parameter map color composite of FRT0000CC22 in which R = D2400, G = D2300, and B = D1900. Areas that appear blue have high D1900 parameter values and areas that appear magenta exhibit high D1900 plus D2400 parameter values.

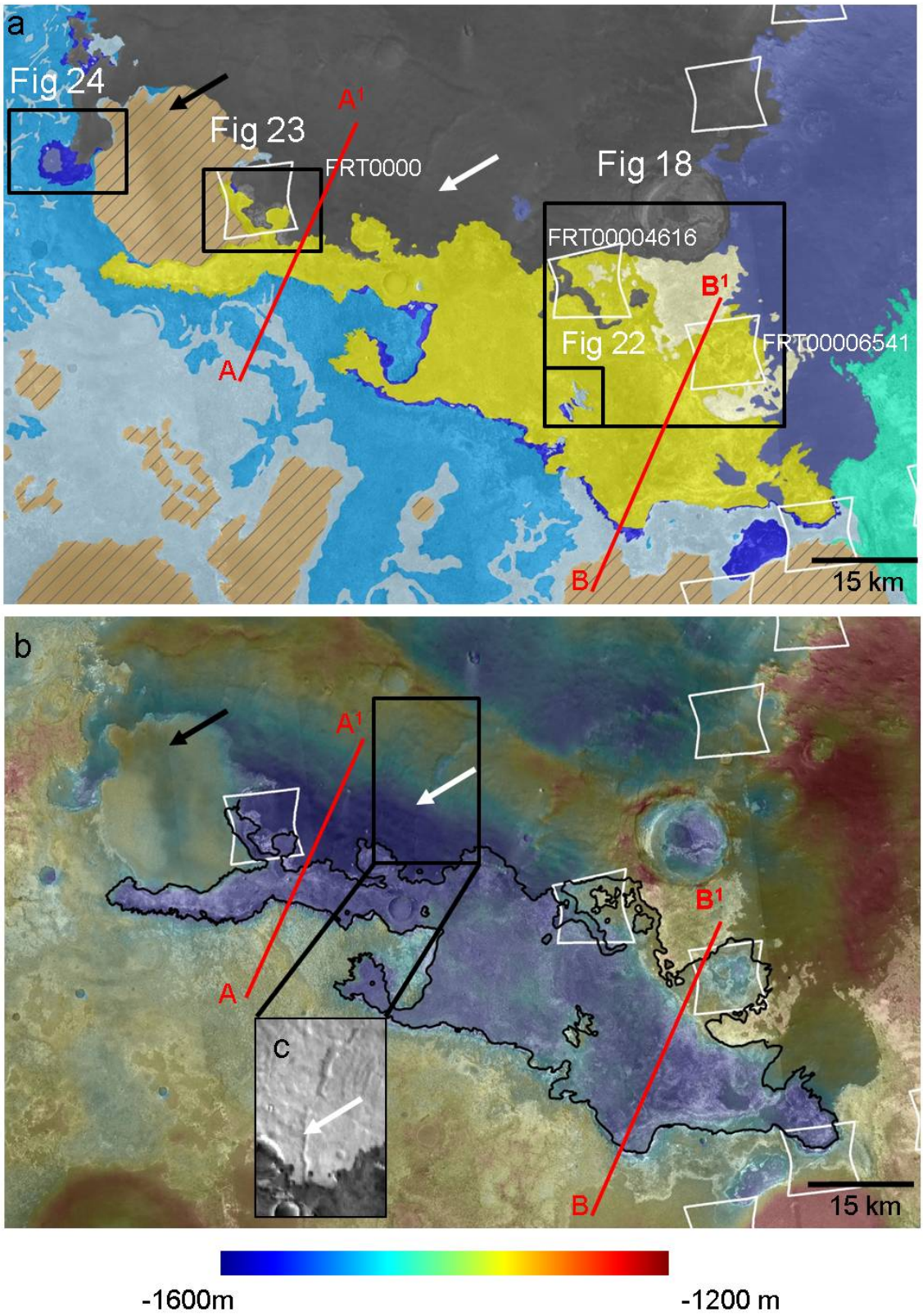
a
Fig 24
Fig 23
A1
FRT0000
Fig 18
FRT00004616
B1
Fig 22
FRT00006541
A
B
15 km
b
A1
B1
A
C
B
15 km
-1600m
-1200 m

Figure 4.17. a) Units map covering area indicated in Figure 4.4. Locations of Figures 4.19, 4.22, 4.22, and 4.24 are outlined. Locations of MOLA profiles shown in Figure 4.29 are indicated in red. A channel feature in CT is indicated with a white arrow. b) CTX mosaic of area in part a) with MOLA color coded elevation overlain. The boundary of the LHS deposits is outlined in black. c) THEMIS DIR mosaic over an area showing a channel feature in CT that is embayed by LHS deposits.

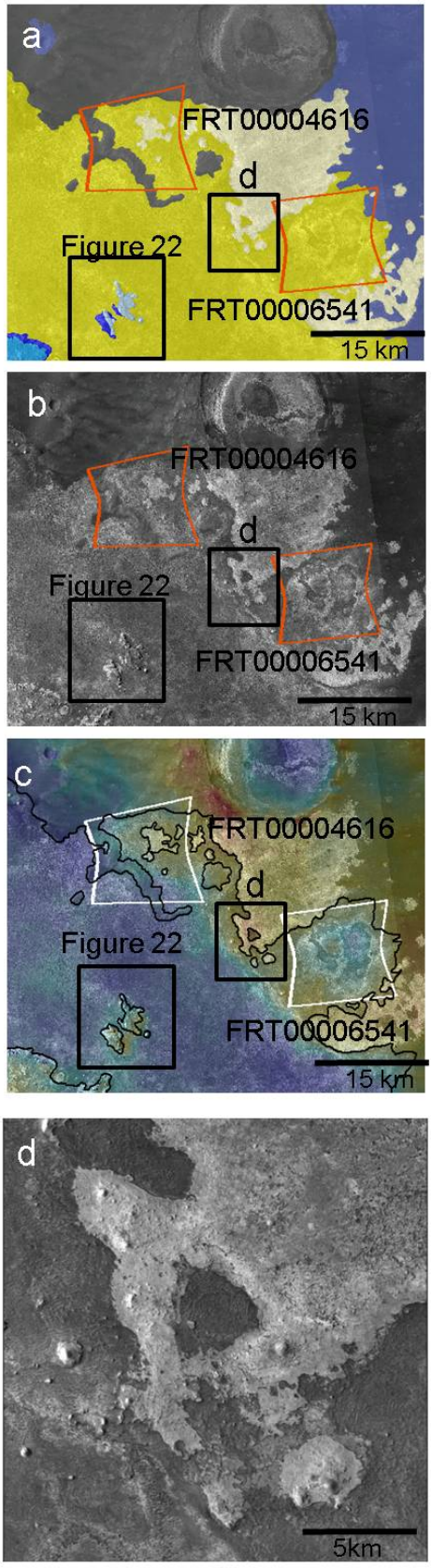
a
FRT00004616
d
Figure 22
FRT00006541
15 km
b
FRT00004616
d
Figure 22
FRT00006541
15 km
c
FRT00004616
d
Figure 22
FRT00006541
15 km
d
5km

Figure 4.18. Subset of area shown in Figure 4.17. a) Units map. b) CTX mosaic. c) CTX with MOLA color coded topography overlain and boundary of LHS deposits indicated in black. d) Subset of part b) showing the morphology of LHS_{cap}.

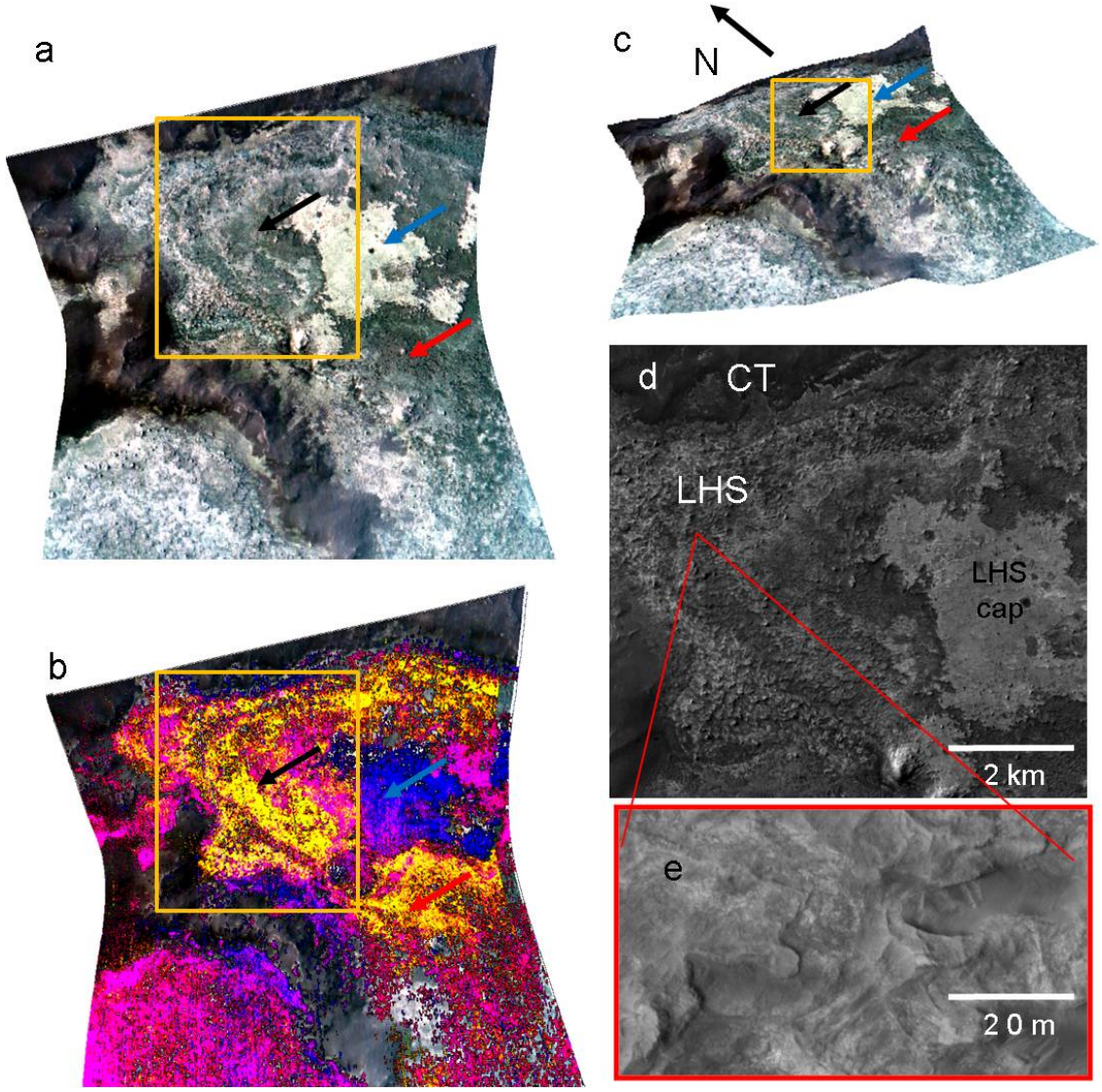
a
b
c
N
d
CT
LHS
LHS
cap
2 km
e
2 0 m

Figure 4.19. a) False color composite of CRISM image FRT00004616 (footprint shown on Figure 4.18) with R = 2.5 μm, G = 1.5 μm, B =1.1 μm. b) Parameter map color composite of FRT00004616 in which R = D2400, G=D2100, and B=D1900. Areas that appear blue have high D1900 parameter values, consistent with the presence of hydrated phases; areas that appear magenta exhibit high D1900 and D2400 parameter values, consistent with polyhydrated sulfates; and areas that appear yellow exhibit high D2100 and D2400 parameters, consistent with monohydrated sulfates. Spectra extracted from black and red arrow shown in Figure 4.21 and spectrum extracted from blue arrow shown in Figure 4.13. c) CRISM FRT00004616 shown in part a) draped on MOLA topography (vertical exaggeration = 10). d) Bright and dark toned layers are evident in CTX image T01_000886_1819_XN_01N000W_061004. A subset of HiRISE PSP_002680_1825_RED indicates that the dark toned material is indurated.

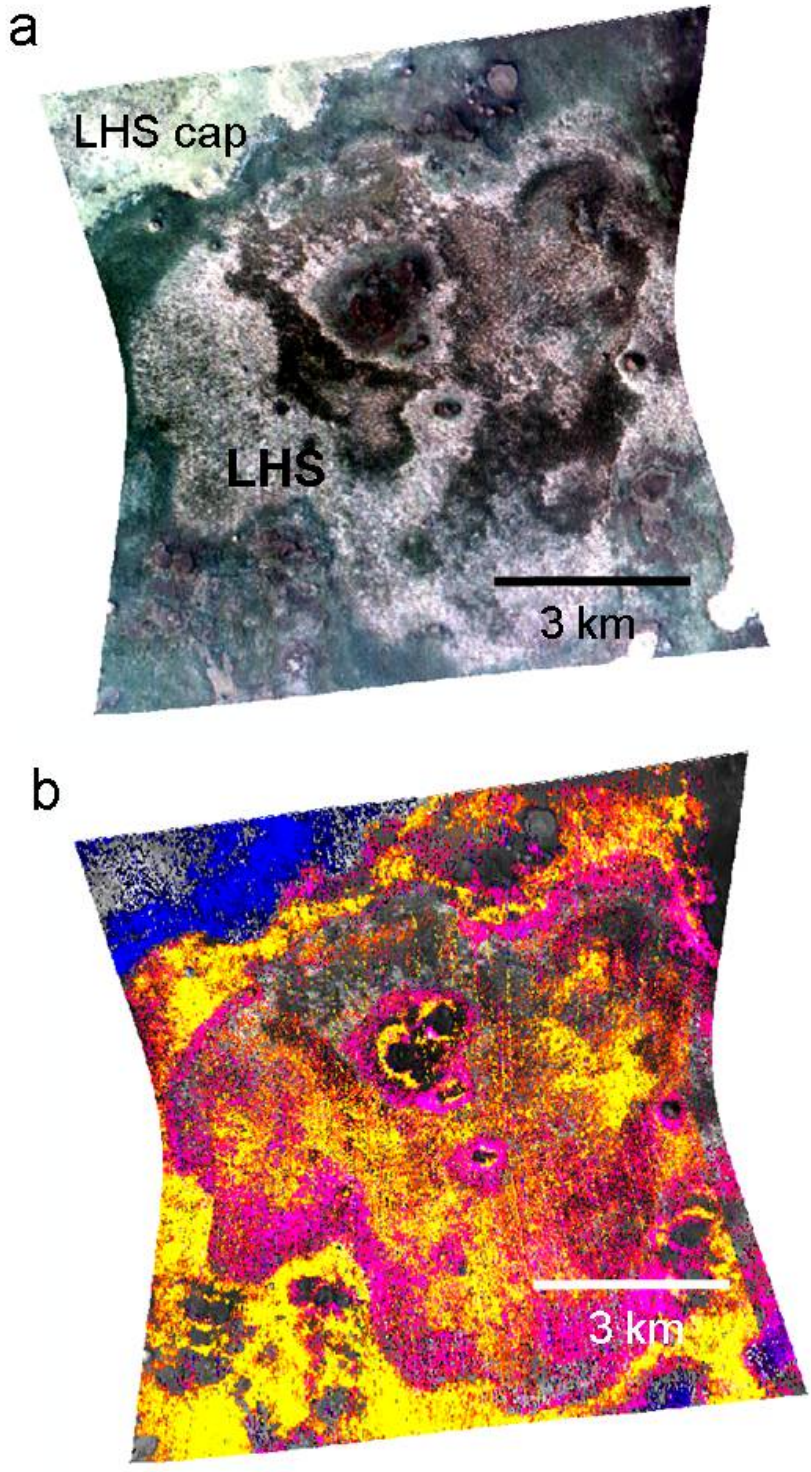
a
LHS cap
LHS
3 km
b
3 km

Figure 4.20. a) False color composite of CRISM image FRT00006541 (footprint shown on Figure 4.18) with R = 2.5 μm, G = 1.5 μm, B = 1.1 μm. b) Parameter map color composite of FRT00006541 in which R = D2400, G=D2100, and B = D1900. Areas that appear blue have high D1900 parameter values, areas that appear magenta exhibit high D1900 plus D2400 parameter values, and areas that appear yellow exhibit high D2100 plus D2400 parameters.

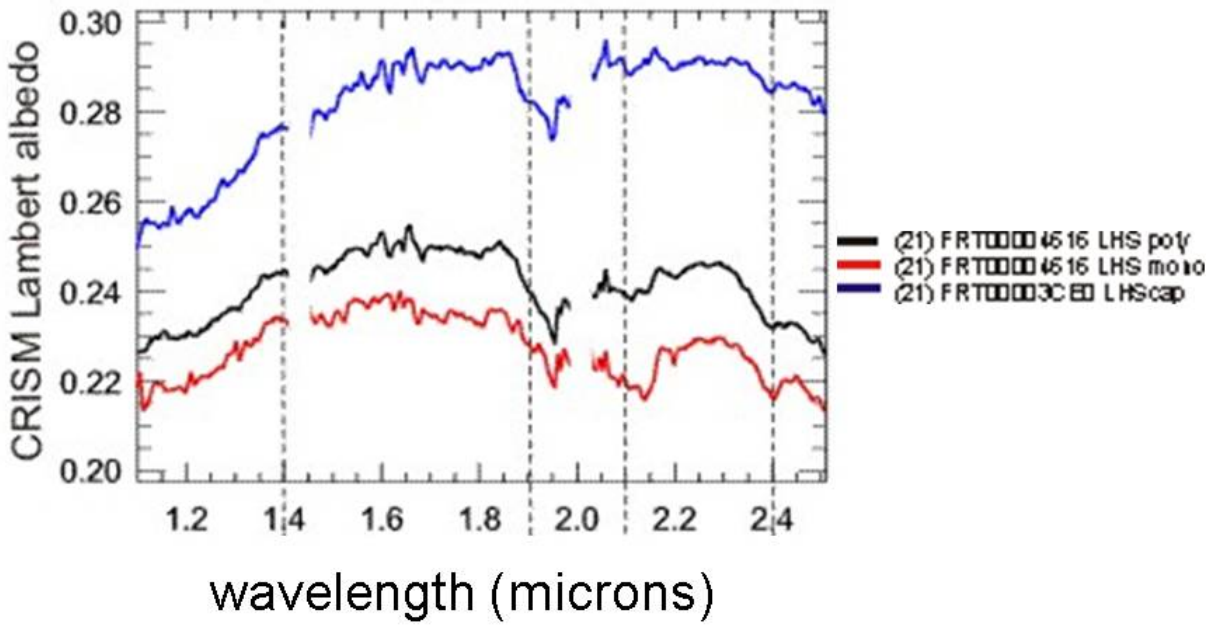

Figure 4.21. Lambert Albedo spectra retrieved using DISORT modeling for areas indicated in Figure 4.19. Each spectrum is an average of 25 spectra.

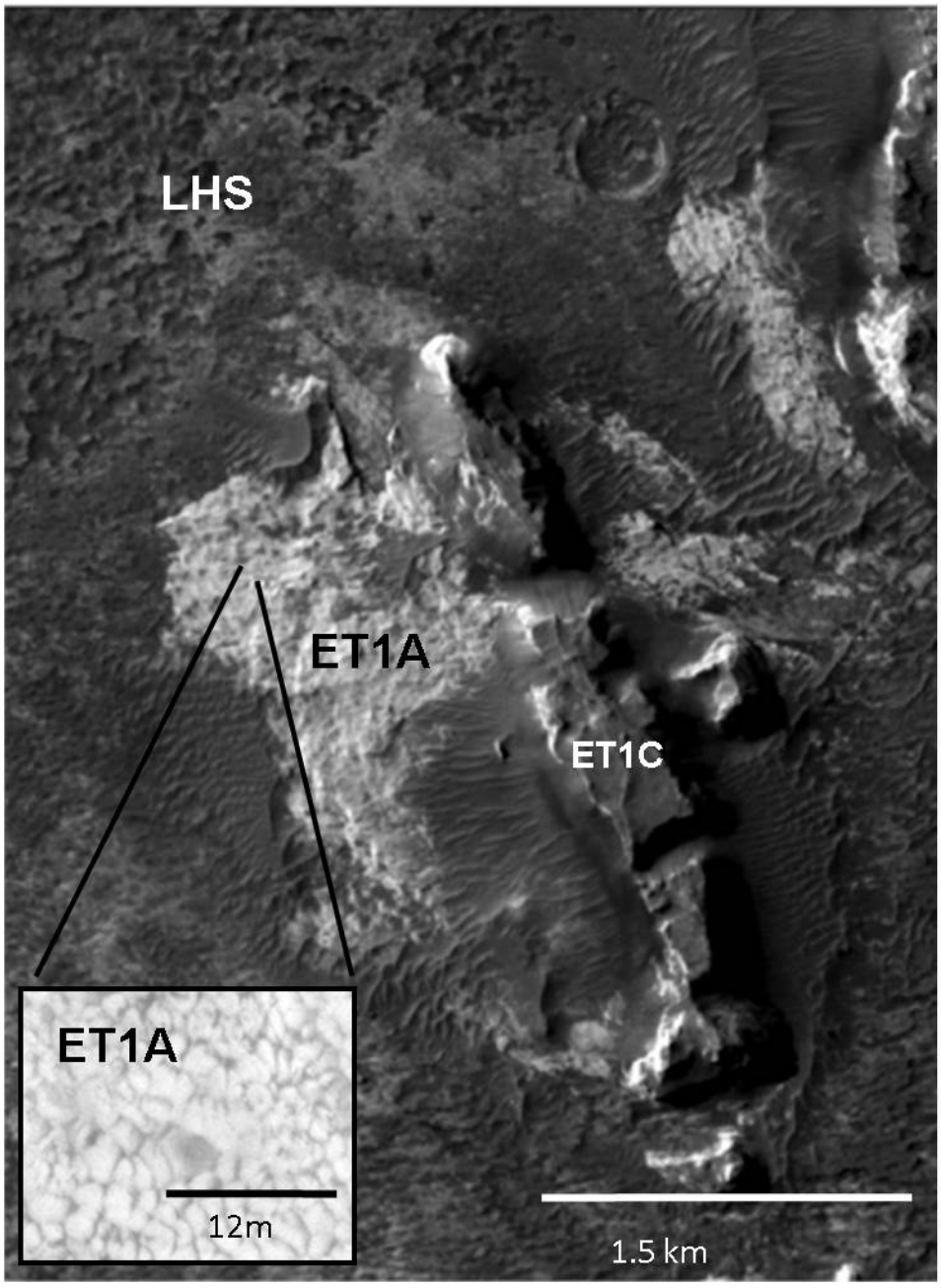
LHS
ET1A
ET1C
ET1A
12m
1.5 km

Figure 4.22. CTX image T01_000886_1819_XN_01N000W_061004 showing mesas within the valley that exhibit the same sequence of layers that occur to the south of the valley, $ET1_A$, $ET1_B$, $ET1_C$, location shown in Figure 4.17. HiRISE inset (PSP_006148_1820_RED) shows scallop texture of $ET1_A$.

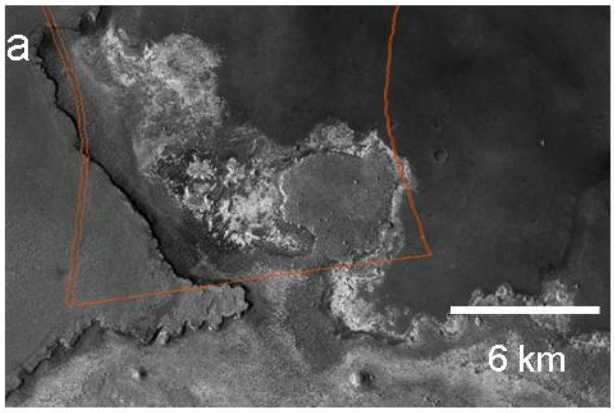
a
6 km

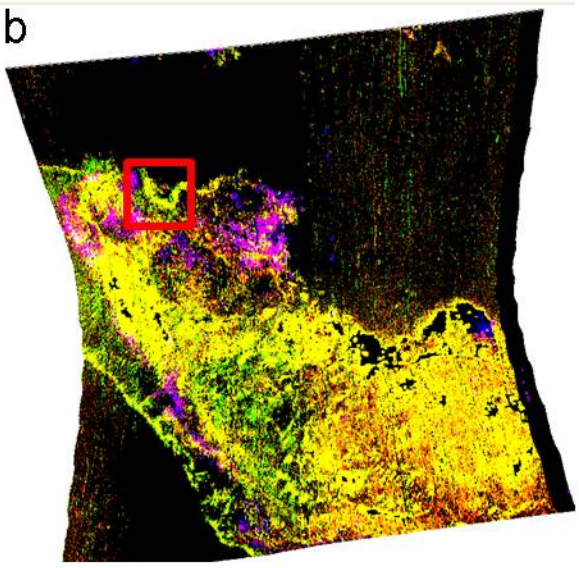
b

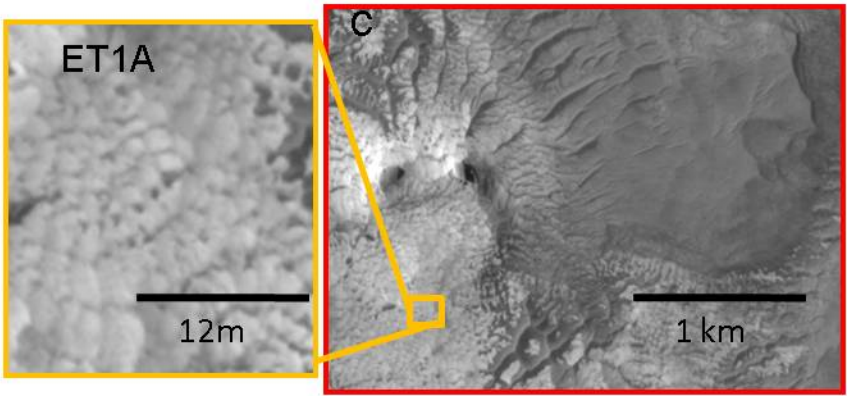
ET1A
12m
c
1 km

Figure 4.23. a) CTX mosaic subset, location shown in Figure 4.17. b) CRISM FRT0000AC13 parameter maps with R = D2400, G = D2100, and B = D1900. Areas that appear magenta exhibit high D1900 plus D2400 parameter values and areas that appear yellow exhibit high D2100 plus D2400 parameters. c) HiRISE PSP_001691_1825_RED subset showing $ET1_A$ and darker overlying material that has a hydrated sulfate spectral signature. Inset shows scalloped texture of $ET1_A$.

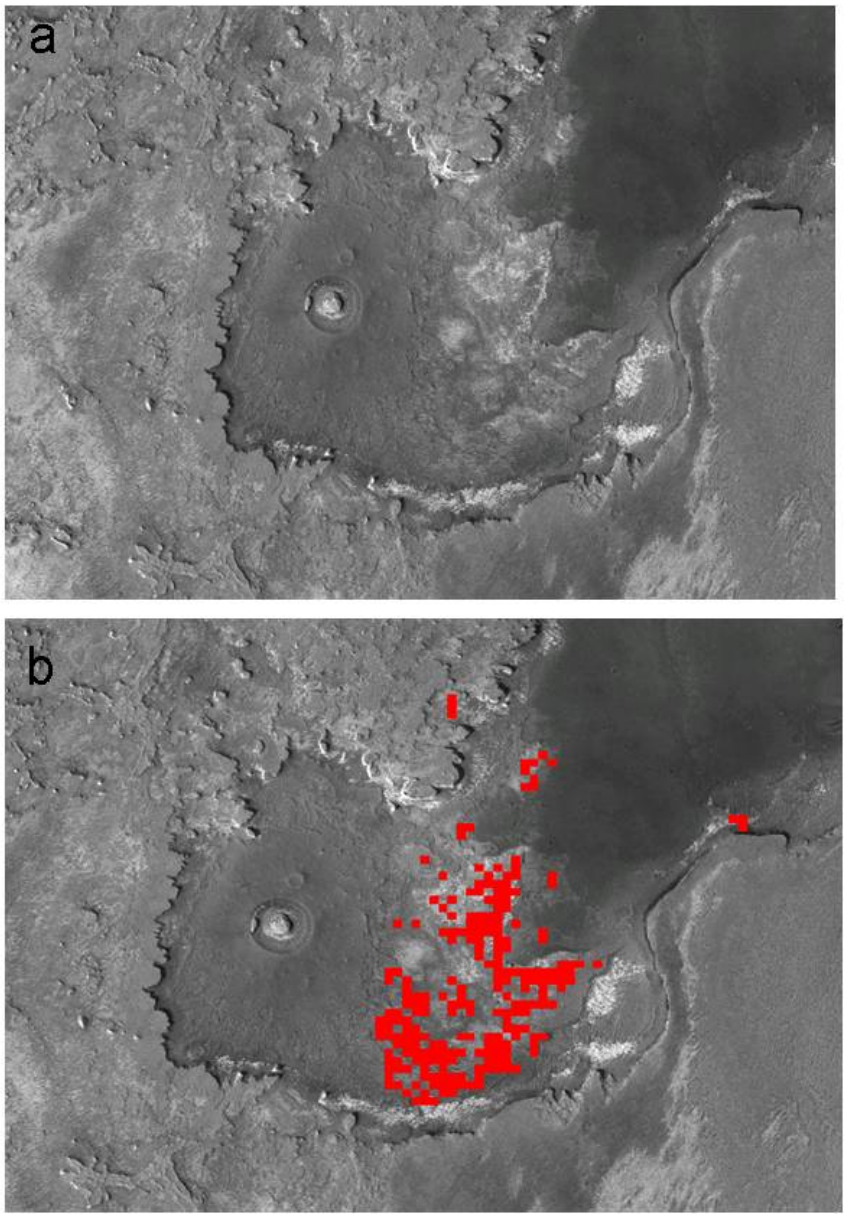

Figure 4.24. a) CTX mosaic, location indicated in Figure 4.17. b) Area shown in part a) with CRISM MSP parameters indicating the presence of hydrated sulfates overlain in red.

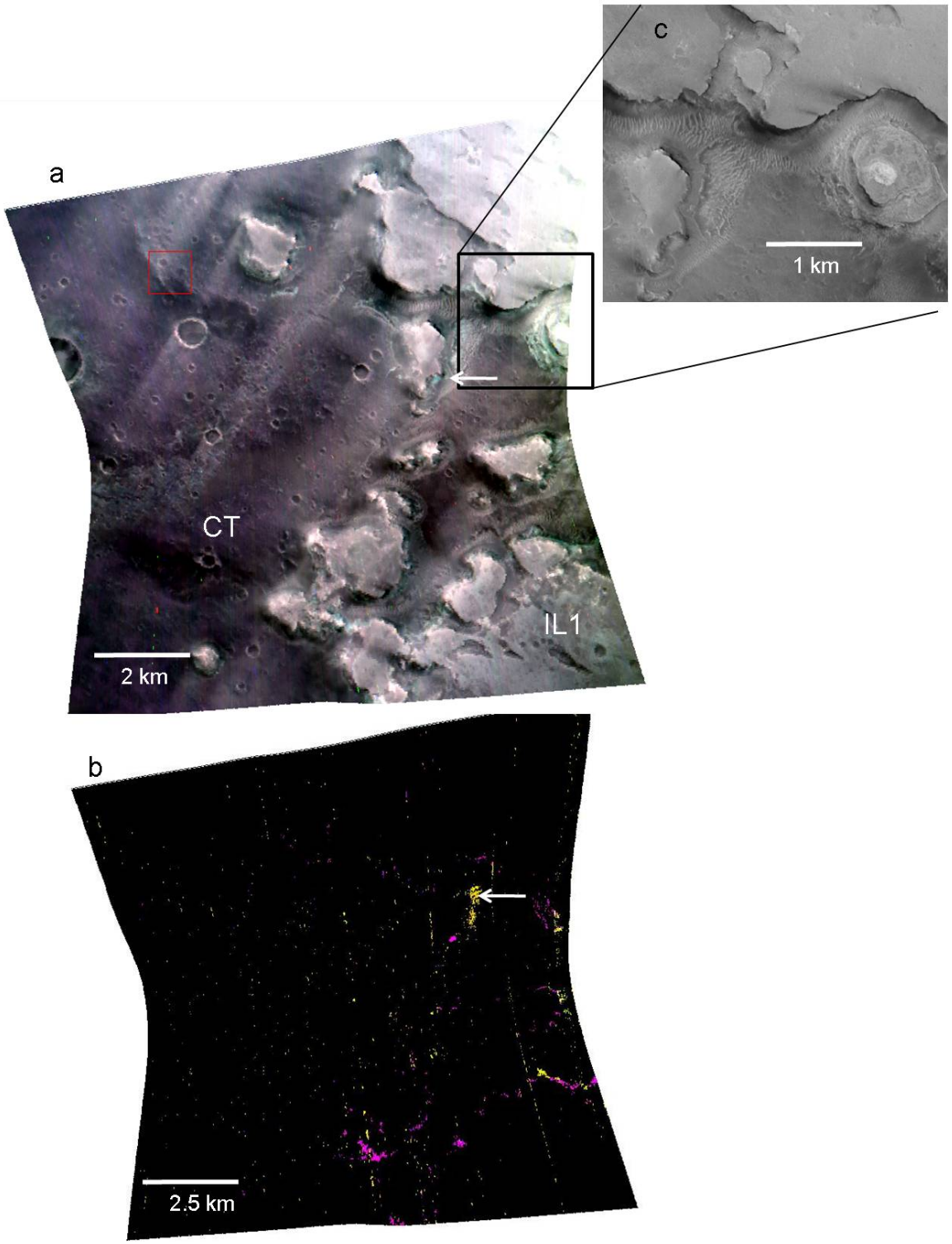
a
c
1 km
CT
IL1
2 km
b
2.5 km

Figure 4.25. a) CRISM image FRT0000893E (footprint Figure 4.4a) false color composite with R = 2.5 μm, G = 1.5 μm, B = 1.1 μm. b) Parameter map of FRT0000893E (R = D2400, G = D2100, B = D1900). Areas that appear magenta exhibit high D1900 plus D2400 parameter values and areas that appear yellow exhibit high D2100 plus D2400 parameters. The materials with hydrated sulfate detections occur in layers exposed at the base of the plateau of $[ET1/LHS/LHS_{cap}]_{mantled}$. The green arrow shows the location of the spectrum shown in Figure 4.26. c) CTX P13_005937_1834_XI_03N359W_071102 showing area indicated in part a).

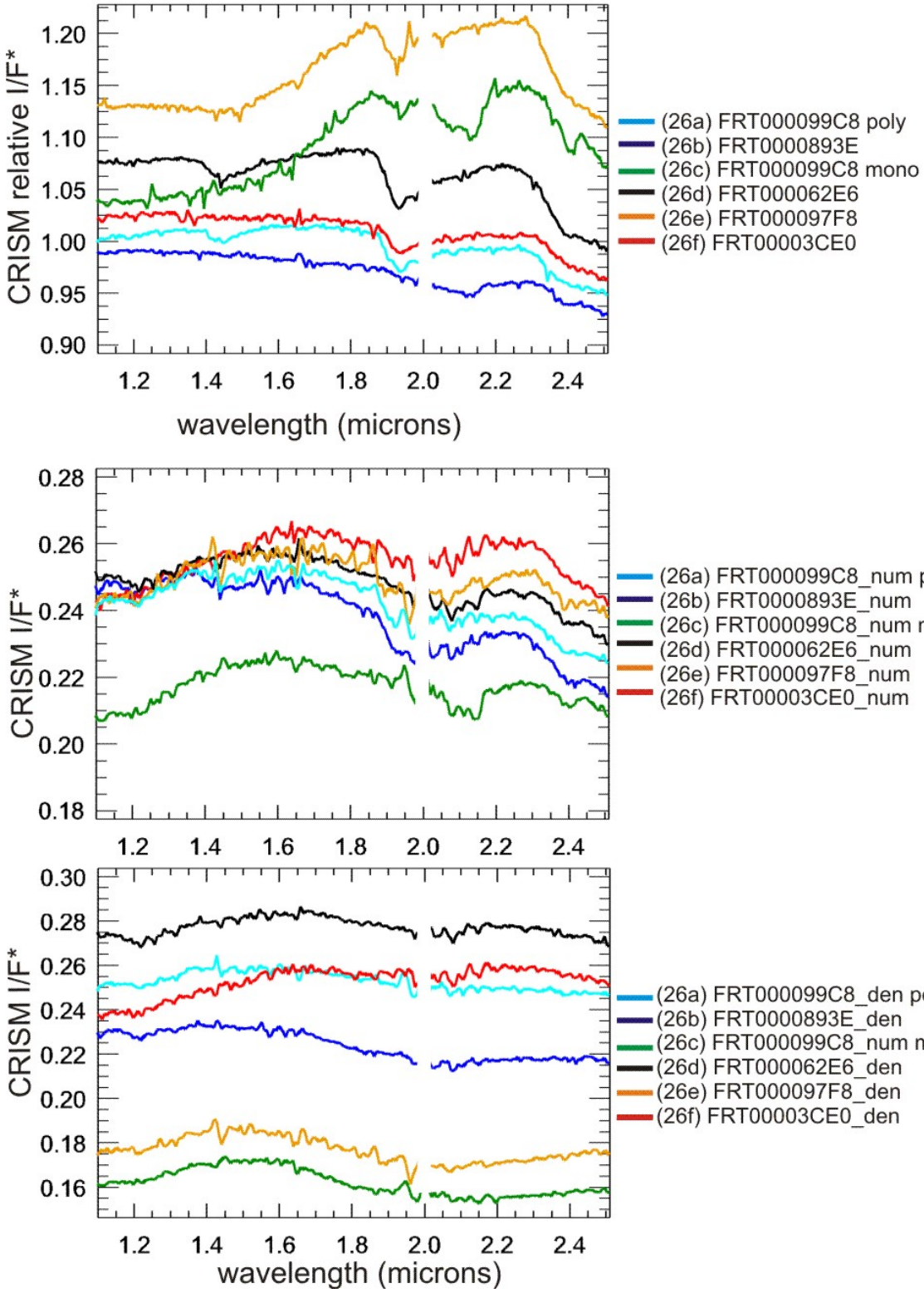
CRISM relative I/F*
1.20
1.15
1.10
1.05
1.00
0.95
0.90
1.2
1.4
1.6
1.8
2.0
2.2
2.4
wavelength (microns)
(26a) FRT000099C8 poly
(26b) FRT0000893E
(26c) FRT000099C8 mono
(26d) FRT000062E6
(26e) FRT000097F8
(26f) FRT00003CE0
CRISM I/F*
0.28
0.26
0.24
0.22
0.20
0.18
(26a) FRT000099C8_num poly
(26b) FRT0000893E_num
(26c) FRT000099C8_num mono
(26d) FRT000062E6_num
(26e) FRT000097F8_num
(26f) FRT00003CE0_num
CRISM I/F*
0.30
0.28
0.26
0.24
0.22
0.20
0.18
0.16
wavelength (microns)
(26a) FRT000099C8_den poly
(26b) FRT0000893E_den
(26c) FRT000099C8_num mono
(26d) FRT000062E6_den
(26e) FRT000097F8_den
(26f) FRT00003CE0_den

Figure 4.26. Upper: CRISM relative reflectance spectra from areas of selected FRTs with hydrated sulfate like spectral signatures. Middle: CRISM I/F* (cos(i) and volcano scan corrected) numerator spectra that were used to generate the ratio spectra shown in the upper plot. Lower: CRISM I/F* (cos(i) and volcano scan corrected) denominator spectra that were used to generate the ratio spectra shown in the upper plot. Each spectrum is an average of 25 spectra.

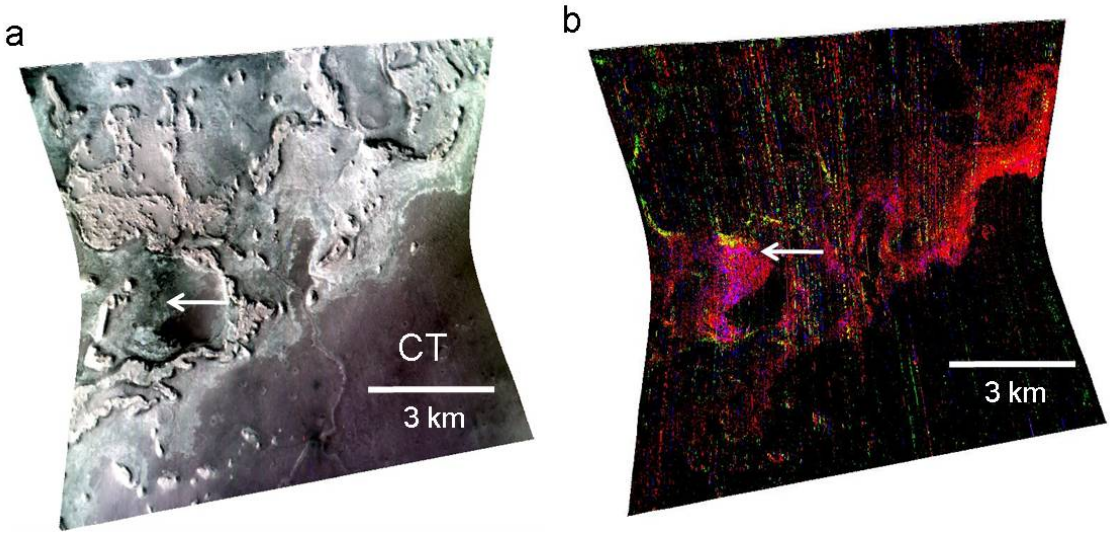

Figure 4.27. a) CRISM image FRT000062E6 (footprint shown in Figure 4.4a) false color composite with R = 2.5 μm, G = 1.5 μm, B = 1.1 μm. b) FRT000062E6 parameter map (R = D2400, G = D2100, and B = D1900). Areas that appear magenta exhibit high D1900 plus D2400 parameter values and areas that appear yellow exhibit high D2100 plus D2400 parameters. The white arrow shows the location of the spectrum in Figure 4.26.

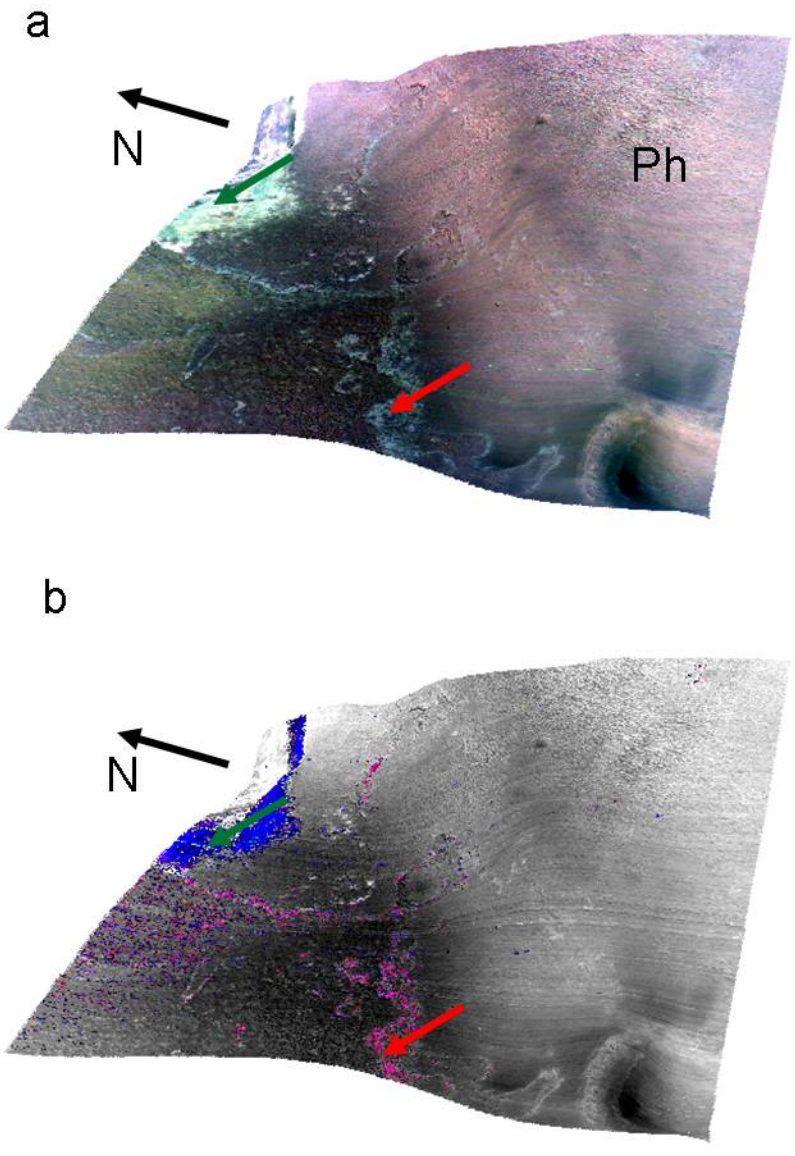
a
N
Ph
b
N

Figure 4.28. a) False color composite of CRISM image FRT00003CE0 (footprint Figure 4.4a) with R=2.5 μm, G=1.5 μm, B=1.1 μm draped on MOLA topography (vertical exaggeration = 10). Ph materials are exposed in the northeastern portion of the image. b) Parameter map color composite of FRT00003CE0 in which R = D2400, G=D2300, and B=D1900 draped on MOLA topography (vertical exaggeration = 10). Areas that appear green have relatively high D2300 values, areas that appear blue have high D1900 parameter values, and areas that appear magenta exhibit high D1900 plus D2400 parameter values. A spectrum extracted from the D2300 material (green arrow) is shown in Figure 4.7 and a spectrum extracted from the D1900 plus D2400 material (red arrow) is shown in Figure 4.26.

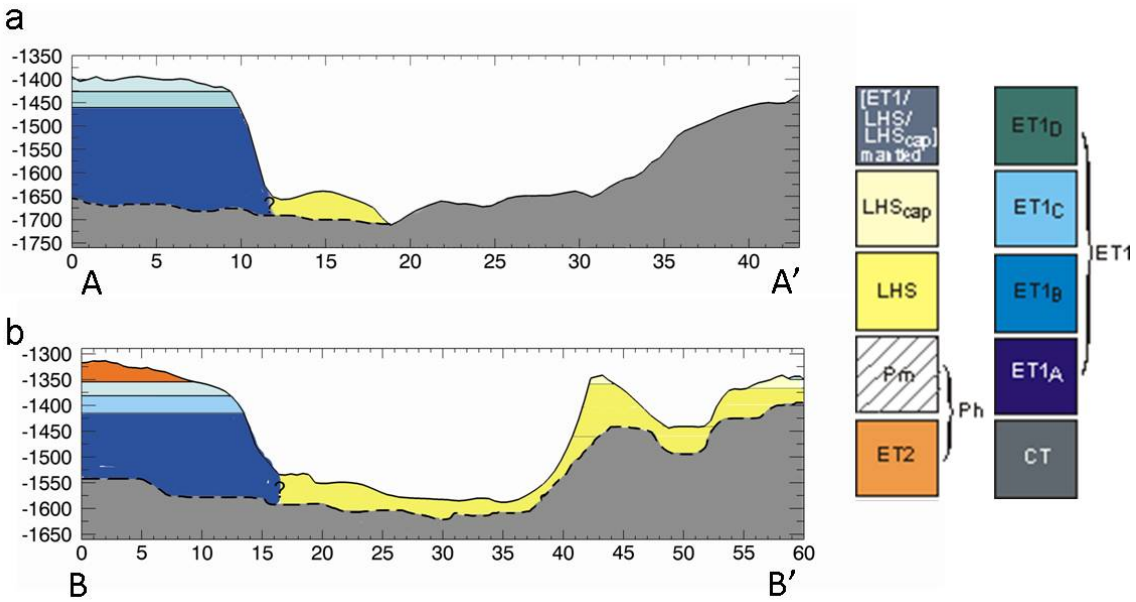

Figure 4.29. Cross sections generated from MOLA topographic profiles along the red lines indicated in Figure 4.17. The units key from Figure 4.4b is shown for reference.

Table 1. Spectral Parameters.

Name	Parameter	Formulation	Threshold	Rationale
BD1900	1.9 μm band depth	1 – (((R1930 + R1985)*0.5)/(a*R1857 + b*R2067))	2%	H_20
BD2100	2.1 μm band depth	1 – (((R2120 + R2140)*0.5)/(a*R1930 + b*R2250))	2%	monohydrated minerals
D2300	2.3 μm drop	1 – ((CR2290 + CR2320 + CR2330)/ (CR2140 + CR2170 + CR2210))	1% CRISM 1.5% OMEGA	Fe-Mg OH vibration
SINDEX	2.4 μm drop	1 – ((CR2390 + CR2430)/(CR2290 + CR2320))	1.5%	hydrated min; particularly sulfates

*CR values are continuum removed and R values are reflectance values at the specified wavelength

REFERENCES

Andrews-Hanna, J. C., M. T. Zuber, and W. B. Banerdt (2009), The Borealis basin and the origin of the Martian dichotomy, *Nature*, 453, 1212-1215 (doi:10.1038/nature07011

Andrews-Hanna, J. C., M. T. Zuber, and R. J. Phillips (2008), Early Mars hydrology: Valley networks and evaporite deposits, *Lunar Planet. Sci.*, *XXXIX*, 1993.

Andrews-Hanna, J. C., R. J. Phillips, and M. T. Zuber (2007), Meridiani Planum and the global hydrology of Mars, *Nature*, *446*, 163-166. doi:10.1038/nature05594.

Arvidson, R. E., F. Poulet, R. V. Morris, J.-P. Bibring, J. F. Bell III, S. W. Squyres, P. R. Christensen, G. Bellucci, B. Gondet, B. L. Ehlmann, W. H. Farrand, R. L. Fergason, J. L. Griffes, J. Grotzinger, E. Guinness, K. E. Herkenhoff, J. R. Johnson, G. Klingelhöfer, Y. Langevin, D. W. Ming, K. Seelos, R. Sullivan, J. Ward, S. M. Wiseman, and M. Wolff (2006), Nature and Origin of the Hematite-Bearing Plains of Terra Meridiani Based on Analysis of Orbital and Mars Exploration Rover Data Sets, *J. Geophys. Res.*, *111*, E12S09, doi:10.1029/2006JE002728.

Arvidson, R. E., F. Poulet, J.-P. Bibring, M.Wolff, A. Gendrin, R. V. Morris, J. J. Freeman, Y. Langevin, N. Mangold, and G. Bellucci (2005), Spectral reflectance and morphologic correlations in eastern Terra Meridiani, Mars, *Science*, 307, 1591– 1594, doi:10.1126/science.1109509.

Arvidson, R. E., F. P. Seelos IV, K. Deal, W. Koeppen, N. Snider, J. Kieniewicz, B. M. Hynek, M. Mellon, and J. Garvin (2003), Mantled and exhumed terrains in Terra Meridiani, Mars, *J. Geophys. Res.*, *108*(E12), 8073, doi:10.1029/2002JE001982.

Bandfield, J. L. (2002), Global mineral distributions on Mars, *J. Geophys. Res.*, *107*(E6), doi:10.1029/2001JE001510.

Bibring, J.-P., A. Soufflot, M. Berthé, Y. Langevin, B. Gondet, P. Drossart, M. Bouyé, M. Combes, P. Puget, A. Semery, G. Bellucci, V. Formisano, V. Moroz, V. Kottsov, G. Bonello, S. Erard, O. Forni, A. Gendrin, N. Manaud, F. Poulet, G. Poulleau, T. Encrenaz, T. Fouchet, R. Melchiori, F. Altieri, N. Ignatiev, D. Titov, L. Zasova, A. Coradini, F. Capacionni, P. Cerroni, S. Fonti, N. Mangold, P. Pinet, B. Schmitt, C. Sotin, E. Hauber, H. Hoffmann, R. Jaumann, U. Keller, R. E. Arvidson, and F. Forget, OMEGA: Observatoire pour la Minéralogie, l'Eau, les Glaces et l'Activite´, in *Mars Express: The Scientific Payload*, edited by A. Wilson, pp. 37-49, Eur. Space Agency Spec. Publ., Noordwijk, The Netherlands, 2004.

Bibring, J.-P., Y. Langevin, J. F. Mustard, F. Poulet, R. E. Arvidson, A. Gendrin, B. Gondet, N. Mangold, P. Pinet, F. Forget, and theOMEGATeam (2006), Global mineralogical and aqueous Mars history derived from OMEGA/Mars Express Data, *Science*, *312*, 400-404. DOI:10.1126/science.1122659.

Bishop, J. L., J. Madejova, P. Komadel, and H. Fröschl (2002), The influence of structural Fe, Al and Mg on the infrared OH bands in spectra of dioctahedral smectites, *Clay MInerals*, *37*, 607-616. DOI: 10.1180/0009855023740063.

Bishop, J. L., and E. Murad (2005), The visible and infrared spectral properties of jarosite and alunite, *American Mineralogist*, *90*, 1100-1107.

Bishop, J., M. Parente, C. Weitz, P. McGuire, E. Noe Dobrea, L. Roach, N. McKeown, N. Rossi, A. Brown, W. Calvin, R., Milliken, S. Murchie, and J. Mustard (2009) Mineralogy of Juventae Chasma: Sulfates in the light-toned Mounds, mafics in the sand, and opal in the plains, *J. Geophys. Res.*, submitted.

Bridges, N.T., Banks, M.E., Beyer, R.A., Chuang, F.C., Dobrea, E.Z.N., Herkenhoff, K.E.,Keszthelyi, L.P., Fishbaugh, K.E., McEwen, A.S., Michaels, T.I., Thomson, B.J., Wray, J.J., Aeolian Bedforms,Yardangs, and Indurated Surfaces in the Tharsis Montes as Seen by the HiRISE Camera: Evidence for Dust Aggregates, Icarus (2009), doi: 10.1016/j.icarus.2009.05.017.

Calvin, W. M., and T. V. V. King (1997), Spectral characteristics of iron-bearing phyllosilicates: Comparison to Orgueil (CI1), Murchison and Murray (CM2), *Meteor. Planet. Sci.*, *32*, 693-701.

Clark, B. C., R. V. Morris, S. M. McLennan, R. Gellert, B. Jolliff, A. H. Knoll, S. W. Squyres, T. W. Lowenstein, D. W. Ming, N. J. Tosca, A. Yen, P. R. Christensen, S. Gorevan, J. Bruckner, W. Calvin, G. Dreibus, W. Farrand, G. Klingelhöfer, H. Waenke, J. Zipfel, J. F. Bell III, J. Grotzinger, H. Y. McSween, and R. Rieder (2005), Chemistry and mineralogy of outcrops at Meridiani Planum, *Earth. Planet. Sci. Lett.*, *240*, 73-94.

Christensen, P. R. (2004), The Thermal Emission Imaging System (THEMIS) for the Mars 2001 Odyssey mission, *Space Sci. Rev.*, *110*, 85-1doi:10.1023/B:SPAC.0000021008.16305.94.

Christensen, P. R., and S. W. Ruff (2004), Formation of the hematite-bearing unit in Meridiani Planum: Evidence for deposition in standing water, *J. Geophys. Res*, *109*, E08003, doi:10.1029/2003JE002233.

Christensen, P. R., R. V. Morris, M. D. Lane, J. L. Bandfield, and M. C. Malin (2001),Global mapping of martian hematite mineral deposits: Remnants of water-driven processes on early Mars, J. Geophys. Res., 106, 23,873–23,886.

Christensen, P. R. (2000), Detection of crystalline hematite mineralization on Mars by the Thermal Emission Spectrometer: Evidence for near-surface water, *J. Geophys. Res*, *105*(E4), 9623-9642.

Christensen, P. (1986), Regional Dust Deposits on Mars: Physical Properties, Age, and History, *J. Geophys. Res*., 91(B3), 3533-3545.

Clark, R. N., G. A. Swayze, R. Wise, K. E. Livo, T. M. Hoefen, R. F. Kokaly, and S. J. Sutley (2007), USGS digital spectral library, *U.S. Geological Survey, Data Series 231*.

Clark, R. N., T. V. V. King, M. Klejwa, and G. A. Swayze (1990), High resolution reflectance spectroscopy of minerals, *J. Geophys. Res*, *95*(B8), 12653-12680.

Cloutis, E. A., F. C. Hawthorne, S. A. Mertzman, K. Krenn, M. A. Craig, D. Marcino, M. Methot, J. Strong, J. F. Mustard, D. L. Blaney, J. F. Bell, III, and F. Vilas (2006), Detection and discrimination of sulfate minerals using reflectance spectroscopy, *Icarus*, *184*, 121-157.

Cooper, C. D., and J. F. Mustard (1999), Effects of very fine particle size on reflectance spectra of smectite and palagonite soil, *Icarus*, *142*, 557-570.

Craddock, R. A., and A. D. Howard (2002), The case for rainfall on a warm, wet early Mars, *J. Geophys. Res*, *107*(E11), 5111, doi:10.1029/2001JE001505, 2002.

CRISM Science Team (2006), Mars Reconnaissance Orbiter CRISM Spectral Library, *NASA Planetary Data System*, MRO-M-CRISM-5-SPECLIB-V1.0.

Crowley, J. K., D. E. Williams, J. M. Hammarstrom, N. Piatak, I.-M. Chou, and J. C. Mars (2003), Spectral reflectance properties (0.4-2.5 μm) of secondary Fe-oxide, Fe-hydroxide, and Fe-sulphate-hydrate minerals associated with sulphide-bearing mine wastes, *Geochemistry: Exploratoin, Environment, Analysis*, *3*, 219-228.

Decarreau, A., S. Petit, F. Martin, F. Farges, P. Vieillart, and Joussein (2008), Hydrothermal synthesis, between 75 and 150°C, of high-charge, ferric nontronites, *Clays Clay Minerals*, 56, 322-337.

Edgett, K. S. (2005), The sedimenatary rocks of Sinus Meridiani: Five key observations from data acquired by the Mars Global Surveyor and Mars Odyssey Orbiters, *Mars*, doi:10.1555/mars.2005.0002.

Edgett, K. S., and M. C. Malin (2002), Martian sedimentary rock stratigraphy: Outcrops and interbedded craters of northwest Sinus Meridiani and southwest Arabia Terra, *Geophys. Res. Lett*., 29, 24, 2179.

Garvin, J. B., J. J. Frawley (1998), Gemmetric properties of Martian impact craters: Preliminary results from the Mars Orbiter Laser Altimeter, *J. Geophys. Res*. 25, 4405-4408.

Gendrin, A., N. Mangold, J.-P. Bibring, Y. Langevin, B. Gondet, F. Poulet, G. Bonello, C. Quantin, J. Mustard, R. E. Arvidson, and S. MeMouelic (2005), Sulfates in Martain layered terrains: The OMEGA/Mars Express view, *Science*, *307*, 1587-1591. doi:10.1126/science.1109087.

Griffes, J. L., R. E. Arvidson, F. Poulet, A. Gendrin (2007), Geologic and spectral mapping of etched terrain deposits in northern Meridiani Planum, *J. Geophys. Res*, 112, E08S09, doi:10.1029/2006JE002811.

Frost, R. L., J. T. Kloprogee, and Z. Ding (2002), Near-infrared spectroscopic study of nontronites and ferruginous smectite, *Geochim. Cosmochim. Acta*, *58*, 1657-1668.

Glotch, T. D., J. L. Bandfield, P. R. Christensen, W. M. Calvin, S. M. McLennan, B. C. Clark, A. D. Rogers, and S. W. Squyres (2006), Mineralogy of the light-toned outcrop at Meridiani Planum as seen by the Miniature Thermal Emission Spectrometer and implications for its formation,, *J. Geophys. Res*, 111, E12S03, doi:10.1029/2005JE002672.

Golden, D. C., D. W. Ming, R. V. Morris, and T. G. Graff (2008), Hydrothermal synthesis of hematite spherules and jarosite: Implications for diagenesis and hematite spherule formation in sulfate outcrops at Meridiani Planum, Mars, *Amer. Mineral.*, *93*, 1201-1214.

Grant, J. A., R. E. Arvidson, L. Crumpler, M. Golombek, B. C. Hahn, A. F. C. Haldemann, R. Li, J. Soderblom, S. W. Squyres, S. P. Wright, and W. A. Watters (2006), Crater gradation in Gusev crater and Meridiani Planum, Mars, *Journal of Geophysical Research*, *111*, doi:10.1029/2005JE002465.

Grotzinger, J. P., R. E. Arvidson, J. F. Bell III, W. M. Calvin, B. C. Clark, D. A. Fike, M. Golombek, R. Greeley, A. Haldermann, K. E. Herkenhoff, B. L. Jolliff, A. H. Knoll, M. Malin, S. M. McLennan, T. Parker, L. A. Soderblom, J. N. Sohl-Dickstein, S. W. Squyres, N. J. Tosca, and W. A. Watters (2005), Stratigraphy and sedimentology of a dry to wet eolian depositional system, Burns formation, Meridiani Planum, Mars, *Earth Planet. Sci. Lett.*, *240*, 11-72.

Hawthorne, F. C., S. V. Krivovichev, and P. C. Burns (2000), The crystal chemistry of sulfate minerals, in *Sulfate Minerals: Crystallography, Geochemistry, and Environmental Significance*, edited by C. N. Alpers, et al., pp. 1-112, Reviews in Mineralogy and Geochemistry, Volume 40, Washington, D.C.

Hynek, B. M., and R. J. Phillips (2008), The stratigraphy of Meridiani Planum, Mars, and implications for the layered deposits' orgin, *EPRSL*, 274.

Hynek, B. M. (2004), Implications for hydrologic processes on Mars from extensive bedrock outcrop throughout Terra Meridiani, *Nature*, 431, 156-159.

Hynek, B. M., R. E. Arvidson, and R. J. PhIL1ips (2002), Geologic setting and origin of Terra Meridiani hematite deposit on Mars, *J. Geophys. Res*, *107*(E10), 5088, doi:10.1029/2002JE001891.

Hynek, B. M., and R. J. Phillips (2001), Evidence for extensive denudation of the Martian highlands, *Geology*, *29*(5), 407-410. doi:10.1130/0091-7613(2001)029.

King, T. V. V., and R. N. Clark (1989), Spectral characteristics of chlorites and Mg-serpentines using high-resolution reflectance spectroscopy, *J. Geophys. Res*, *94*(B10), 13997-14008.

Klingelhöfer, G., R. V. Morris, B. Bernhardt, C. Schröder, D. S. Rodionov, P. A. de Souza, Jr., A. Yen, R. Gellert, E. N. Evlanov, B. Zubkov, J. Foh, U. Bonnes, E. Kankeleit, P. Gütlich, D. W. Ming, F. Renz, T. Wdowiak, S. W. Squyres, and R. E. Arvidson (2004), Jarosite and hematite at Meridiani Planum from Opportunity's Mössbauer Spectrometer, *Science*, *306*, 1740-1745. DOI: 10.1126/science.1104653.

Knauth, L. P., D. M. Burt, K. H. Wohletz (2005), Impact origin of sediments at the Opportunity landing site on Mars, *Nature*, 438, 1123-1128.

Knoll A. H., et al. (2008), Veneers, rinds, and fracture fills: Relatively late alteration of sedimentary rocks at Meridiani Planum, Mars, *J. Geophys. Res*, 113, E06S16, doi:10.1029/2007JE002949.

Lane, M. D., P. R. Christensen, and W. K. Hartmann (2003), Utilization of the THEMIS visible and infrared imaging data for crater population studies of the Meridiani Planum landing site, *Geophys. Res. Lett*., 30(14), 1770, doi:10.1029/2003GL017183.

Malin, M. C., J. F. Bell III, B. A. Cantor, M. A. Caplinger, W. M. Calvin, R. T. Clancy, K. S. Edgett, L. Edwards, R. M. Haberle, B. J. PhIL1ips, S. W. Lee, M. A. Ravine, P. C. Thomas, and M. J. Wolff (2007), Context Camera Investigation on board the Mars Reconnaissance Orbiter, *J. Geophys. Res*, *112*, E05S04, doi:10.1029/2006JE002808.

Malin, M. C. (1992), Mars Observer Camera, *J. Geophys. Res*, *97*, 7699-7718.

Malin, M. C., and K. S. Edgett (2000), Sedimentary rocks of early Mars, *Science* 290, 1927-1937.

Mangold, N., A. Gendrin, B. Gondet, S. LeMouelic, C. Quantin, V. Ansan, J.-P. Bibring, Y.Langevin, P. Masson, and G. Neukum (2008) Spectral and geological study of the sulfate-rich region of West Candor Chasma, Mars, *Icarus*, *194*, 519-543.

McEwen, A. S., E. M. Eliason, J. W. Bergstrom, N. T. Bridges, C. J. Hansen, W. A. Delamere, J. A. Grant, V. C. Gulick, K. E. Herkenhoff, L. Keszthelyi, R. L. Kirk, M. T. Mellon, S. W. Squyres, N. Thomas, and C. M. Weitz (2007), Mars Reconnaissance Orbiter's High Resolution Imaging Science Experiment (HiRISE), *J. Geophys. Res*, *112*, E05S02, doi:10.1029/2005JE002605.

McCollum, T. M. and B. M. Hynek (2005), A volcanic environment for bedrock diagenesis at Meridiani Planum on Mars, *Nature*, 438, 1129-1131.

McGretchin, T. R., M. Settle, and J. W. Head (1973), Radial thickness of variation in impact crater ejecta: Implications for lunar basin deposits, EPSL, 20, 226-236.

McLennan, S. M., J. F. Bell III, W. M. Calvin, P. R. Christensen, B. C. Clark, P. A. de Souza, J. Farmer, W. H. Farrand, D. A. Fike, R. Gellert, A. Ghosh, T. D. Glotch, J. P. Grotzinger, B. Hahn, K. E. Herkenhoff, J. A. Hurowitz, M. C. Malin, H. Y. McSween Jr., J. Pocock, S. W. Ruff, L. A. Soderblom, S. W. Squyres, N. J. Tosca, W. A. Watters, M. B. Wyatt, and A. Yen (2005), Provenance and diagenesis of the evaporite-bearing Burns formation, Meridiani Planum, Mars, *Earth Planet. Sci. Lett.*, *240*, 95-121.

Mellon, M. T., B. M. Jakosky, H. H. Kieffer, and P. R. Christensen, Highresolution thermal inertia mapping from the Mars Global Surveyor Thermal Emission Spectrometer, *Icarus*, 148, 255–437, 2001.

Milliken, R. E., and J. F. Mustard (2005), Quantifying absolute water content of minerals using near-infrared reflectance spectroscopy, *J. Geophys. Res*, *110*, E12001, doi:10.1029/2005JE002534.

Morris, R. V., G. Klingelhöfer, C. Schröder, D. S. Rodionov, A. Yen, D. W. Ming, P. A. de Souza Jr., T. Wdowiak, I. Fleischer, R. Gellert, B. Bernhardt, U. Bonnes, B. A. Cohen, E. N. Evlanov, J. Foh, P. Gütlich, E. Kankeleit, T. McCoy, D. W. Mittlefehldt, F. Renz, M. E. Schmitt, B. Zubkov, S. W. Squyres, and R. E. Arvidson (2006), Mössbauer mineralogy of rock, soil, and dust at Meridiani Planum, Mars: Opportunity's journey across sulfate-rich outcrops, basaltic sand and dust, and hematite lag deposits, *J. Geophys. Res*, *111*, E12S15, doi:10.1029/2006JE002791.

Murchie, S., R. E. Arvidson, P. Bendini, K. Beisser, J.-P. Bibring, J. Bishop, J. Boldt, P. Cavender, T. Choo, R. T. Clancy, E. H. Darlington, D. Des Marais, R. Espiritu, D. Fort, R. Green, E. Guinness, J. Hayes, C. Hash, K. Heffernan, J. Hemmler, G. Heyler, D. Humm, J. Hutchenson, N. Izenberg, R. Lee, J. Lees, D. Lohr, E. Malaret, T. Martin, J. A. McGovern, P. McGuire, R. V. Morris, J. F. Mustard, S. Pelkey, E. Rhodes, M. Robinson, T. Roush, E. Schafer, G. Seagrave, F. P. Seelos, IV, S. Slavney, M. Smith, W.-J. Shyong, K. Stohbehn, H. Taylor, P. Thompson, B. Tossman, M. Wirzburger, and M. Wolff (2007), Compact Reconnaissance Imaging Spectrometer for Mars (CRISM) on Mars Reconnaissance Orbiter (MRO), *J. Geophys. Res*, *112*, E05S03, doi:10.1029/2006JE002682.

Murchie, S. L., L. H. Roach, F. P. Seelos, R. E. Milliken, J. F. Mustard, R. E. Arvidson, S. Wiseman, K. Lichtenberg, J. Andrews-Hanna, J.-. Bibring, P., J. L. Bishop, M. Parente, and R. V. Morris (2009), Compositional Evidence for the Origin of Layered Deposits in Valles Marineris, Mars, *Journal of Geophysical Research*, submitted.

Mustard, J. F., F. Poulet, A. Gendrin, J.-P. Bibring, Y. Langevin, B. Gondet, N. Mangold, G. Bellucci, and F. Altieri (2005), Olivine and pyroxene diversity in the crust of Mars, *Science*, *307*, 1594-1597. doi: 10.1126/science.1109098.

Newsom, H. E., C. A. Barber, T. M. Hare, T. Schelble, V. A. Sutherland, and W. C. Feldman (2003), Paleolakes and impact basins in southern Arabia Terra, including Meridiani Planum: Implications for the formation of hematite deposits on Mars, *J. Geophys. Res*, *108* (E12), 8075, doi:10.1029/2002JE001993.

Neukum, G., R. Jaumann, and H. C.-I. a. E. Team, HRSC: The High Resolution Stereo Camera of Mars Express, in *Mars Express: The Scientific Payload*, edited by A. Wilson, pp. 17-35, Eur. Space Agency Spec. Publ., Noordwijk, The Netherlands, 2004.

Noe Dobrea, E.Z., F. Poulet, and M.C. Malin (2008), Correlations between hematite and sulfates in the chaotic terrain east of Valles Marineris, *Icarus*, *193*, 516-534, doi:10.1016/j.icarus.2007.06.029.

Parente, M. (2008), A new approach to denoisig CRISM images, *LPSC XXXVIII*, #2528.

Pelkey, S. M., J. F. Mustard, S. Murchie, R. T. Clancy, M. Wolff, M. Smith, R. Milliken, J.-P. Bibring, A. Gendrin, F. Poulet, Y. Langevin, and B. Gondet (2007), CRISM multispectral summary products: Parameterizing mineral diversity on Mars from reflectance, *J. Geophys. Res*, *112*, E08S14, doi:10.1029/2006JE002831.

Phillips, R. J., et al., (2001), Ancient geodynamics and global-scale hydrology of Mars, *Science*, 291, 2587– 2591.

Poulet, F., J.-P. Bibring, J. F. Mustard, A. Gendrin, N. Mangold, Y. Langevin, R. E. Arvidson, B. Gondet, and C. Gomez (2005), Phyllosilicates on Mars and implications for early Martian climage change, *Nature*, *438*, 632-627. doi:10.1038/nature04274.

Poulet, F., R. E. Arvidson, C. Gomez, R. V. Morris, J.-P. Bibring, Y. Langevin, B. Gondet, and J. Griffes (2008), Mineralogy of Terra Meridiani and western Arabia Terra from OMEGA/MEx and implications for their formation, *Icarus*, *195*(1), 106-130. 10.1016/j.icarus.2007.11.031.

Presley, M. A. and R. E. Arvidson, Nature and origin of materials exposed in the Oxia Palus-Western Arabia-Sinus Meridiani region, Mars (1988), *Icarus*, 75.

Rieder, R., R. Gellert, R. C. Anderson, J. Brückner, B. C. Clark, G. Dreibus, T. Economou, G. Klingelhöfer, G. W. Lugmair, D. W. Ming, S. W. Squyres, C. d'Uston, H. Wänke, A. Yen, and J. Zipfel (2004), Chemistry of rocks and soils at Meridiani Planum from Alpha Particle X-ray Spectrometer, *Science*, *306*, 1746-1749. doi:10.1126/science.1104358.

Rotto, S., and K. L. Tanaka (1995), Geologic/geomorphic map of the Chryse Planitia region of Mars, U.S. Geol. Surv. Misc. Invest. Map, I-2441

Schultz, P. H., and A. B. Lutz (1988), Polar wandering of Mars, *Icarus*, 73, 91– 141.

Scott, D. H., and K. L. Tanaka (1986), Geologic map of the western equatorial region of Mars, U.S. Geol. Surv. Misc. Invest. Map, I-1802-A, 1986.

Sullivan et al. (2005), Aeolian processes at the Mars Exploration Rover Meridiani Planum landing site, *Nature*, 436, 58-61, doi:10.1038/nature03641

Tanaka, K. L., The stratigraphy of Mars, Proc. Lunar Planet. Sci. Conf., XVIIth, J. Geophys. Res., 91, E139-E158.

Smith, D. E., M. T. Zuber, H. V. Frey, J. B. garvin, J. W. Head, D. O. Muhlemann, G. H. PettenfIL1, R. J. PhIL1ips, S. C. Solomon, H. J. Zwally, W. B. Banerdt, T. C. Duxbury, M. P. Golombek, F. G. Lemoine, G. A. Neumann, D. D. Rowlands, O. Aharonson, P. G. Ford, A. B. Ivanov, C. L. Johnson, P. J. McGovern, J. B. Abshire, R. S. Afzal, and X. Sun (2001), Mars Orbiter Laser Altimeter: Experiment summary after the first year of global mapping of Mars, *J. Geophys. Res*, *106*(E10), 23689-23722.

Stoffregen, R. E., C. N. Alpers, and J. L. Jambor, Alunite-jarosite crystallography, thermodynamics, and geochemistry, in *Sulfate Minerals: Crystallography, Geochemistry, and Environmental Significance, Rev. Mineral. Geochem.*, edited by C.N. Alpers, J.L. Jambor, and D.K. Nordstrom, pp. 453-480, Mineral. Soc. of Am., Washington D.C., 2000.

Squyres, S. W., R. E. Arvidson, E. Baumgartner, J. F. Bell III, P. R. Christensen, S. Gorevan, K. E. Herkenhoff, G. Klingelhofer, M. B. Madsen, R. V. Morris, R. Rieder, and R. Romero (2003), The Athena Mars Rover Science Investigation, *Journal of Geophysical Research*, *108*(E12), doi:10.1029/2003JE002121.

Squyres, S. W., R. E. Arvidson, J. F. Bell III, J. Bruckner, N. A. Cabrol, W. M. Calvin, M. H. Carr, P. R. Christensen, B. C. Clark, L. Crumpler, D. J. Des Marais, C. d'Uston, T. Economou, J. Farmer, W. H. Farrand, W. Folkner, M. Golombek, S. Gorevan, J. A. Grant, R. Greeley, J. Grotzinger, L. Haskin, K. E. Herkenhoff, S. Hviid, J. R. Johnson, G. Klingelhofer, A. H. Knoll, G. Landis, M. Lemmon, R. Li, M. B. Madsen, M. C. Malin, S. M. McLennan, H. Y. McSween, D. W. Ming, J. Moersch, R. V. Morris, T. Parker, J. W. Rice Jr., L. Richter, R. Rieder, M. Sims, M. Smith, P. Smith, L. A. Soderblom, R. Sullivan, H. Wanke, T. Wdowiak, M. Wolff, and A. Yen (2004), The Opportunity Rover's Athena Science Investigation at Meridiani Planum, Mars, *Science*, *306*, 1698-1703.

Stamnes, K., S. Tsay, W. Wiscombe, and K. Jayaweera (1988), Numerically stable algorithm for discrete-ordinate-method radiative transfer in multiple scattering and emitting layered media, *Appl. Opt.*, *27*, 2502-2509.

Stoffregen, R. E., C. N. Alpers, and J. L. Jambor, Alunite-jarosite crystallography, thermodynamics, and geochemistry, in *Sulfate Minerals: Crystallography, Geochemistry, and Environmental Significance, Rev. Mineral. Geochem.*, edited by C.N. Alpers, J.L. Jambor, and D.K. Nordstrom, pp. 453-480, Mineral. Soc. of Am., Washington D.C., 2000.

Swayze, G. A., R. N. Clark, S. J. Sutley, C. A. Gent, B. W. Rockwell, D. L. Blane, J. L. Post, and B. P. Farm, Mineral mapping Mauna Kea and Mauna Loa shield volcanos on Hawaii using AVIRIS data and the USGS Tetracorder spectral identification system: Lessons applicable to the search for relict Martian hydrothermal systems, in *Proceedings of the 11th JPL Airborne Earth Science Workshop*, edited by R.O. Green, pp. 373-387, 2002.

Wolff, M. J., R. T. Clancy, M. D. Smith, CRISM Science Team, and Marci Science Team (2007), Some studies of Martian aerosol properties using MRO/CRISM and MRO/Marci, *Sev. Intl. Conf. Mars*, 3121.

Wiseman, S.M., R. E. Arvidson, R. V. Morris, F. Poulet, S. L. Murchie, F. P. Seelos, J. L. Bishop, J. C. Andrews-Hanna, D. Des Marais, J. L. Griffes (2009a), Retrieval of atmospherically corrected hyperspectral CRISM surface reflectance spectra using DISORT radiative transfer modeling: Comparison to the empirical volcano scan correction method, *J. Geophys. Res*, in prep.

Wiseman S. M., et al. (2008), Phyllosilicate and sulfate-hematite deposits within Miyamoto crater in southern Sinus Meridiani, Mars, *Geophys. Res. Lett*., 35, L19204, doi:10.1029/2008GL035363.

Wiseman, S. M. et al. (2007), Initial analysis of CRISM data over Meridiani Planum. *LPSC XXXVIII*: Abstract #1945.

Wolff, M. J., M. D. Smith, R. T. Clancy, R. E. Arvidson, M. Kahre, F. P. Seelos IV, S. Murchie, H. Savij¨arvi, and the CRISM Science Team (2009), Wavelength Dependence of Dust Aerosol Single Scattering Albedo As Observed by CRISM, *J. Geophys. Res*, submitted.

CHAPTER 5 – SYNTHESIS

In this chapter, a brief synopsis is presented that focuses on of key results from dissertation related research. Analyses utilized recently acquired near infrared spectra from the Mars Reconnaissance Orbiter (MRO) Compact Reconnaissance Imaging Spectrometer for Mars (CRISM) in conjunction with other datasets. Atmospheric correction of data acquired from orbit is necessary for proper interpretation of surface spectral properties in the visible and near infrared. The retrieval of atmospherically corrected surface CRISM Lambert Albedo spectra using Discrete Ordinate Radiative Transfer (DISORT) model results is described by *Wiseman et al*., [2009a]. Both aerosol and gas atmospheric contributions are modeled and removed during Lambert Albedo retrieval. High spectral resolution synthetic I/F spectra are resampled to CRISM spectral sampling and time/temperature dependent wavelength shifts that occur in CRISM data are calculated during the Lambert Albedo retrieval process. DISORT radiative transfer modeling was also used to explore artifacts generated by the commonly used empirical volcano scan correction method, which employs division by a scaled transmission spectrum to correct for gas bands only. It was found that residual gas band artifacts that occur in volcano scan corrected data can mimic the presence of surface features. In the current implementation of the volcano scan correction, a constant exponential scaling factor is used to scale the transmission spectrum. Residual features near gas bands are produced because scaling the entire transmission spectrum by a constant exponential factor is not physically correct.

Distinctive spectral features caused by H_2O and/or OH vibrational modes were used to identify hydrated and/or hydroxylated mineral phases in near infrared spectra.

Analyses of high spatial resolution CRISM images revealed the presence of previously unreported exposures of hydrated sulfate and phyllosilicate-bearing deposits. We preformed mineralogic and stratigraphic mapping in southern and northern Sinus Meridiani using MRO CRISM, MRO Context Imager, MRO High Resolution Imaging Science Experiment, Mars Express (MEX) Observatoire pour la Minéralogie, l'Eau, les Glaces et l'Activité, MEX High Resolution Stereo Camera, Mars Odyssey (ODY) Thermal Emission Imaging System, ODY Mars Orbital Camera, and ODY Mars Orbiter Laser Altimeter data. Fe/Mg phyllosilicate minerals, including Fe/Mg smectites, occur in multiple locations in ancient Noachian terrains [*Wiseman et al*., 2008]. Laterally continuous strata were mapped over 100s of km in extensive indurated sedimentary deposits that unconformably overlie ancient Noachian terrain and predate the formation of the hematite-bearing unit explored by the MER rover Opportunity. Fe/Mg smectites also occur within these older sedimentary deposits. A thick sequence (~150 m thick in some locations) of layered hydrated sulfate deposits that are texturally and spectrally distinct from the sulfate rich sedimentary materials explored by the Opportunity rover were unconformably deposited following the partial erosion of the older sedimentary deposits [*Wiseman et al.,* 2009].

The presence of Fe/Mg smectite-bearing deposits indicates that the low pH conditions experienced by younger hematite-bearing materials are not representative of the aqueous geochemical environment that prevailed during the formation of earlier materials. The deposits in Sinus Meridiani record the transition from an open hydrologic system with near neutral pH conditions to a more arid acid-sulfate dominated ground water system. The detection of phyllosilicate-bearing deposits in association with the

oldest terrains in Sinus Meridiani is consistent with the hypothesis that phyllosilicates formed within the oldest terrains on Mars and that geochemical conditions became inconducive to phyllosilicate formation in later periods [*Bibring et al.,* 2006].

REFERENCES

Bibring, J.-P., et al. (2006), Global mineralogical and aqueous Mars history derived from OMEGA/Mars Express Data, *Science*, *312*, 400-404.

Wiseman S. M., R. E. Arvidson, J. C. Andrews-Hanna, R. N. Clark, N. L. Lanza, D. Des Marais, G. A. Marzo, R. V. Morris, S. L. Murchie, H. E. Newsom, E. Z. Noe Dobrea, A. M. Ollila, F. Poulet, T. L Roush, F. P. Seelos, G. A. Swayze (2008), Phyllosilicate and sulfate-hematite deposits within Miyamoto crater in southern Sinus Meridiani, Mars, Geophys. Res. Lett., 35, L19204, doi:10.1029/2008GL035363.

Wiseman, S.M., R. E. Arvidson, R. V. Morris, F. Poulet, S. L. Murchie, F. P. Seelos, J. L. Bishop, J. C. Andrews-Hanna, D. Des Marais, J. L. Griffes (2009), Spectral and stratigraphic mapping of hydrated sulfate and phyllosilicate-bearing deposits in northern Sinus Meridiani, Mars, *J. Geophys. Res*, in revision.

Wiseman, S.M., R. E. Arvidson, R. V. Morris, F. Poulet, S. L. Murchie, F. P. Seelos, J. L. Bishop, J. C. Andrews-Hanna, D. Des Marais, J. L. Griffes (2009a), Retrieval of atmospherically corrected hyperspectral CRISM surface reflectance spectra using DISORT radiative transfer modeling: Comparison to the empirical volcano scan correction method, *J. Geophys. Res*, in prep.

APPENDIX A – LIST OF CRISM IMAGES UTILIZED IN CHAPTER 4

Image ID	Day of Year	Resolution (m/pixel)
FRT000028C1_07_IF165L_TRR2.IMG	2006_277	20
FRT00003CE0_07_IF165L_TRR2.IMG	2007_008	20
FRT00003E24_07_IF165L_TRR2.IMG	2007_013	20
FRT0000410F_07_IF166L_TRR2.IMG	2007_029	20
FRT00004616_07_IF165L_TRR2.IMG	2007_052	20
FRT00004A01_07_IF165L_TRR2.IMG	2007_068	20
FRT00004FE8_07_IF165L_TRR2.IMG	2007_085	20
FRT000062E6_07_IF165L_TRR2.IMG	2007_162	20
FRT00006541_07_IF165L_TRR2.IMG	2007_173	20
FRT000067EA_07_IF165L_TRR2.IMG	2007_184	20
FRT00006A2A_07_IF165L_TRR2.IMG	2007_195	20
FRT00007C29_07_IF166L_TRR2.IMG	2007_261	20
FRT00007DA9_07_IF165L_TRR2.IMG	2007_267	20
FRT000080C0_07_IF166L_TRR2.IMG	2007_278	20
FRT000083E7_07_IF167L_TRR2.IMG	2007_289	20
FRT00008592_07_IF165L_TRR2.IMG	2007_294	20
FRT0000893E_07_IF165L_TRR2.IMG	2007_306	20
FRT00009217_07_IF165L_TRR2.IMG	2008_001	20
FRT0000942E_07_IF165L_TRR2.IMG	2008_007	20
FRT0000960F_07_IF165L_TRR2.IMG	2008_012	20
FRT000097F8_07_IF165L_TRR2.IMG	2008_018	20
FRT000099C8_07_IF165L_TRR2.IMG	2008_024	20
FRT00009B1C_07_IF165L_TRR2.IMG	2008_029	20
FRT00009C73_07_IF165L_TRR2.IMG	2008_035	20
FRT0000A0AC_07_IF165L_TRR2.IMG	2008_052	20
FRT0000A1F3_07_IF165L_TRR2.IMG	2008_057	20
FRT0000A50D_07_IF165L_TRR2.IMG	2008_068	20
FRT0000AA11_07_IF165L_TRR2.IMG	2008_118	20
FRT0000AB4F_07_IF165L_TRR2.IMG	2008_124	20
FRT0000AC13_07_IF165L_TRR2.IMG	2008_130	20
FRT0000B084_07_IF165L_TRR2.IMG	2008_164	20
FRT0000B203_07_IF165L_TRR2.IMG	2008_169	20
FRT0000B33A_07_IF165L_TRR2.IMG	2008_175	20
FRT0000B710_07_IF165L_TRR2.IMG	2008_191	20
FRT0000B8D7_07_IF165L_TRR2.IMG	2008_196	20
FRT0000BAD3_07_IF165L_TRR2.IMG	2008_203	20
FRT0000BC30_07_IF165L_TRR2.IMG	2008_208	20

FRT0000BEF5_07_IF165L_TRR2.IMG	2008_219	20
FRT0000C52C_07_IF165L_TRR2.IMG	2008_247	20
FRT0000CC22_07_IF165L_TRR2.IMG	2008_275	20
FRT00010099_07_IF165L_TRR2.IMG	2008_357	20
FRT00010107_07_IF165L_TRR2.IMG	2008_358	20
FRT000102AB_07_IF165L_TRR2.IMG	2008_362	20
FRT00010837_07_IF166L_TRR2.IMG	2009_013	20
FRT00010F03_07_IF165L_TRR2.IMG	2009_040	20
FRT0001215B_07_IF165L_TRR2.IMG	2009_107	20
FRT0001252F_07_IF165L_TRR2.IMG	2009_118	20
HRL000068D0_07_IF182L_TRR2.IMG	2007_189	40
HRL0000822E_07_IF182L_TRR2.IMG	2007_283	40
HRL00008C6B_07_IF182L_TRR2.IMG	2007_350	40
HRL00009C41_07_IF182L_TRR2.IMG	2008_034	40
HRL0000CFB0_07_IF182L_TRR2.IMG	2008_291	40
HRS0000513B_07_IF174L_TRR2.IMG	2007_090	40
HRS0000B237_07_IF174L_TRR2.IMG	2008_170	40
HRS0000C10B_07_IF174L_TRR2.IMG	2008_230	40
HRS0000C7B0_07_IF174L_TRR2.IMG	2008_258	40
HRS0000D731_07_IF174L_TRR2.IMG	2008_324	40
MSW00003471_01_IF191L_TRR2.IMG	2006_340	100
MSW00003B72_01_IF193L_TRR2.IMG	2007_002	100
MSW00003FC9_01_IF191L_TRR2.IMG	2007_024	100
MSW000047E2_01_IF191L_TRR2.IMG	2007_058	100
MSW000058CC_01_IF191L_TRR2.IMG	2007_112	100
MSW00005AD3_01_IF193L_TRR2.IMG	2007_134	100
MSW00005E14_01_IF191L_TRR2.IMG	2007_145	100
MSW00007F0B_01_IF191L_TRR2.IMG	2007_272	100
MSW00008E00_01_IF191L_TRR2.IMG	2007_355	100
MSP00002F48_05_IF214L_TRR2.IMG	2006_314	200
MSP00002F48_07_IF214L_TRR2.IMG	2006_314	200
MSP0000301D_07_IF214L_TRR2.IMG	2006_319	200
MSP00003281_05_IF214L_TRR2.IMG	2006_329	200
MSP00003281_07_IF214L_TRR2.IMG	2006_329	200
MSP000037BE_01_IF214L_TRR2.IMG	2006_355	200
MSP00004226_07_IF214L_TRR2.IMG	2007_034	200
MSP00004227_01_IF214L_TRR2.IMG	2007_034	200
MSP00004278_07_IF214L_TRR2.IMG	2007_035	200
MSP00004279_01_IF214L_TRR2.IMG	2007_035	200
MSP00004471_01_IF214L_TRR2.IMG	2007_046	200

MSP000048F0_01_IF214L_TRR2.IMG	2007_063	200
MSP00005189_07_IF214L_TRR2.IMG	2007_091	200
MSP0000518A_01_IF214L_TRR2.IMG	2007_091	200
MSP0000518A_03_IF214L_TRR2.IMG	2007_091	200
MSP0000518A_05_IF214L_TRR2.IMG	2007_091	200
MSP0000518A_07_IF214L_TRR2.IMG	2007_091	200
MSP0000518B_01_IF214L_TRR2.IMG	2007_091	200
MSP0000518B_03_IF214L_TRR2.IMG	2007_091	200
MSP0000518B_05_IF214L_TRR2.IMG	2007_091	200
MSP0000518B_07_IF214L_TRR2.IMG	2007_091	200
MSP0000518C_01_IF214L_TRR2.IMG	2007_091	200
MSP0000518C_03_IF214L_TRR2.IMG	2007_091	200
MSP0000518D_01_IF211L_TRR2.IMG	2007_091	200
MSP0000528E_03_IF214L_TRR2.IMG	2007_095	200
MSP000052E4_05_IF214L_TRR2.IMG	2007_096	200
MSP00005684_01_IF214L_TRR2.IMG	2007_106	200
MSP0000568C_01_IF214L_TRR2.IMG	2007_106	200
MSP00005693_01_IF213L_TRR2.IMG	2007_106	200
MSP000056ED_01_IF213L_TRR2.IMG	2007_107	200
MSP00005787_01_IF214L_TRR2.IMG	2007_109	200
MSP00005789_01_IF214L_TRR2.IMG	2007_109	200
MSP0000578A_01_IF213L_TRR2.IMG	2007_109	200
MSP0000578C_01_IF213L_TRR2.IMG	2007_109	200
MSP0000578F_01_IF214L_TRR2.IMG	2007_109	200
MSP0000578F_03_IF214L_TRR2.IMG	2007_109	200
MSP00005792_01_IF214L_TRR2.IMG	2007_109	200
MSP00005793_01_IF213L_TRR2.IMG	2007_109	200
MSP00005794_01_IF213L_TRR2.IMG	2007_109	200
MSP000057A2_01_IF214L_TRR2.IMG	2007_109	200
MSP000057A3_01_IF214L_TRR2.IMG	2007_109	200
MSP000057A5_01_IF214L_TRR2.IMG	2007_109	200
MSP00005C73_05_IF214L_TRR2.IMG	2007_139	200
MSP00005FC8_07_IF214L_TRR2.IMG	2007_150	200
MSP00006024_05_IF214L_TRR2.IMG	2007_151	200
MSP00006024_07_IF214L_TRR2.IMG	2007_151	200
MSP0000612A_07_IF214L_TRR2.IMG	2007_156	200
MSP00006179_07_IF214L_TRR2.IMG	2007_157	200
MSP00006D9F_05_IF214L_TRR2.IMG	2007_211	200
MSP00006F54_05_IF214L_TRR2.IMG	2007_217	200
MSP00006F54_07_IF214L_TRR2.IMG	2007_217	200

MSP0000727B_01_IF214L_TRR2.IMG	2007_229	200
MSP000073D2_01_IF214L_TRR2.IMG	2007_234	200
MSP000073D2_03_IF214L_TRR2.IMG	2007_234	200
MSP00007589_07_IF214L_TRR2.IMG	2007_240	200
MSP00007889_05_IF214L_TRR2.IMG	2007_250	200
MSP00007889_07_IF214L_TRR2.IMG	2007_250	200
MSP00007A90_01_IF214L_TRR2.IMG	2007_256	200
MSP0000C26A_01_IF211L_TRR2.IMG	2008_235	200
MSP0000C670_01_IF211L_TRR2.IMG	2008_253	200
MSP00010701_01_IF211L_TRR2.IMG	2009_008	200
MSP00010A7B_01_IF214L_TRR2.IMG	2009_024	200
MSP00011192_01_IF214L_TRR2.IMG	2009_046	200
MSP0001134A_01_IF214L_TRR2.IMG	2009_051	200
MSP0001139A_01_IF214L_TRR2.IMG	2009_052	200
MSP00011837_01_IF214L_TRR2.IMG	2009_068	200
MSP00011966_01_IF211L_TRR2.IMG	2009_074	200
MSP00011C5A_01_IF211L_TRR2.IMG	2009_085	200